

공학박사학위논문

광대역 직교모드 변환기 설계

**Design of Wideband Orthomode Transducers**

충북대학교 대학원

전파통신공학과 전파통신공학전공

바양뫑흐 엔흐바야르  
(Bayanmunkh Enkhbayar)

2011년 2월

공  
학  
박  
사  
학  
위  
논  
문

광  
대  
역  
직  
교  
모  
드  
변  
환  
기  
설  
계

B  
A  
Y  
A  
N  
M  
U  
N  
K  
H

2  
0  
1  
1  
년  
2  
월

공학박사학위논문

광대역 직교모드 변환기 설계

**Design of Wideband Orthomode Transducers**

지도교수 안병철

전파통신공학과 전파통신공학전공

바양몽흐 엔흐바야르  
(**Bayanmunkh Enkhbayar**)

이 논문을 공학박사학위논문으로 제출함.

2011년 2월

본 논문을 바양뫑호 앵호바야르의 공학박사학위 논문으로 인정함.

심 사 위 원 장      안재형 ⑩

심 사 부 위 원 장      안병철 ⑩

심 사 위 원              김경석 ⑩

심 사 위 원              방재훈 ⑩

심 사 위 원              안병권 ⑩

충북대학교대학원

2011년 2월

# CONTENTS

<b>요약문</b>	<b>iii</b>
<b>ABSTRACT</b>	<b>v</b>
<b>LIST OF FIGURES</b>	<b>vii</b>
<b>LIST OF TABLES</b>	<b>xii</b>
<b>I Introduction</b>	<b>1</b>
<b>II Design of Wideband Orthomode Transducers</b>	<b>6</b>
2.1 Structure and Specifications of an OMT .....	6
2.2 Dunning OMT .....	10
2.3 Bøifot OMT with Double Ridges .....	29
2.4 Branch-Line OMT .....	52
<b>III Fabrication</b>	<b>69</b>
3.1 Fabrication of the Dunning OMT .....	71
3.2 Fabrication of the Bøifot OMT with Double Ridges .....	73
3.3 Fabrication of the Branch-Line OMT .....	76
<b>IV Measurement</b>	<b>79</b>
4.1 Measurement of the Dunning OMT .....	82
4.2 Measurement of the Bøifot OMT with Double Ridges .....	87
4.3 Measurement of the Branch-Line OMT .....	91
<b>V Conclusions</b>	<b>95</b>

<b>REFERENCES</b>	<b>97</b>
<b>ACKNOWLEDGEMENTS</b>	<b>104</b>

# 광대역 직교모드변환기 설계 \*

바양몽호 앵그바야르

충북대학교 대학원 전자통신공학과

지도교수 안 병 철

## 요 약 문

최근에 넓은 연속 주파수 스펙트럼 특성이 요구되는 밀리미터파 위성 통신 혹은 전자 천문학 분야에서 넓은 대역 특성을 가지는 직교모드변환기에 대한 연구가 활발히 진행되고 있다. 직교모드 변환기는 편파가 서로 수직인 두 개의 전자파가 공용 도파관에 입사될 경우 이를 각각의 출력 도파관으로 분리하는 장치이다. 일반적인 광대역 직교모드 변환기는 원형 혹은 사각 형상의 공용 포트, 편파 분리부, 계단형 혹은 테이퍼 형태의 임피던스 정합 구조와 전력 결합기 등으로 구성된다.

대부분의 광대역 직교모드 변환기는 그 구조가 매우 복잡하므로 직교모드 변환기 설계 시 제작의 용이성을 고려하여야 한다. 실험실 모델 직교모드 변환기는 직교모드변환기 구조에서 대칭인 절반을 별도로 가공하여 결합하는 split-block 기법을 적용하여 제작된다.

---

\* A dissertation for the degree of Doctor in February 2011.

본 논문에서는 광대역 직교모드 변환기의 설계 및 제작에 한해 연구하였다. 문헌상에 제시된 여러 광대역 직교모드 변환기의 구조 중에서 Dunning 형태, Bøifot 접합, 가지선로 직교모드 변환기를 연구하였다. 가공을 보다 용이하게 하고 성능을 더 좋게 하기 위해, 각 직교모드변환기의 기존 구조를 개선하였다. 각 직교모드 변환기 구조의 구체적인 설계 절차를 제시하였다. 본 논문에서 사용한 상용 소프트웨어의 패러미터 변화 기능을 사용하여 각각의 직교모드 변환기를 최적 설계하였다. 설계된 직교모드 변환기를 split-block 기법에 의해 제작한 후 설계 타당성 검증을 위해 그 특성을 측정하였다.

# **Design of Wideband Orthomode Transducers**

**Bayanmunkh Enkhbayar**

*Department of Radio and Communications Engineering*

*Graduate School, Chungbuk National University*

*Cheongju City, South Korea*

*Supervised by Professor Bierng-Chearl Ahn, Ph. D.*

## ABSTRACT

In recent years, there have been active research efforts in wideband orthomode transducers (OMTs) for satellite communication and radio astronomy in millimeter-wave bands, where a large continuous spectrum of frequencies is often of interest. An OMT is a device for separating two orthogonally-polarized waves incident on a common waveguide into their respective output waveguides. High-performance OMTs are usually realized using square and rectangular waveguides. A typical wideband OMT consists of a common waveguide, of either circular or rectangular cross section, a polarization-separating junction, impedance-matching steps or tapers, and a power combiner.

When designing an OMT, one has to consider the ease of fabrication since most of wideband OMTs are structurally very complicated. Laboratory model OMTs are usually fabricated using the split-block technique, where symmetric halves in the OMT structure are separately machined and then joined together.

In this dissertation, the design and fabrication of wideband OMTs are investigated. Among many wideband OMT structures published in the open literature, following types are considered: the Dunning type, the Bøifot junction and the branch-line OMT. The existing structure of each OMT type is improved for easier fabrication and better performance. Detailed design procedures are given for each OMT type. For each OMT type, an optimum design is obtained using the parameter sweep function of the commercial software used in this dissertation. Designed OMTs are fabricated using the split-block technique and measured for design verification.

## LIST OF FIGURE

Fig. 1.1 OMT in an dual-polarized feed.....	1
Fig. 2.1 Strcuture of a generic OMT.....	7
Fig. 2.2 Structure of a Dunning OMT.....	10
Fig. 2.3 Operation of the Dunning OMT with the common port excited with (a) a vertically-polarized wave and (b) a horizontally-polarized wave.....	12
Fig. 2.4 Designation of cross sections of the Dunning OMT.....	14
Fig. 2.5 Internal electric fields of the Dunning OMT at various cross sections.....	18
Fig. 2.6 Dimenstions of the Dunning OMT. (a) 3D view, (b) side view and (c) bottom view.....	21
Fig. 2.7 Performance of the Dunning OMT with initial dimensions. (a) Reflection coefficient, (b) transmission coefficient and (c) isolation and polarization descrimination.....	23
Fig. 2.8 Performance of the designed Dunning OMT. (a) Reflection coefficient, (b) transmission coefficient and (c) polarization descrimination and isolation....	25
Fig. 2.9 Effects of dimensional parameters on the reflection coefficient of the Dunning OMT.....	28
Fig. 2.10 Strcuture of the original Bøifot OMT.....	30
Fig. 2.11 Strcuture of the Bøifot OMT with double ridges. (a) External and (b) internal view of the double-ridge section. ....	32
Fig. 2.12 Magnitude of internal electric fields of the Bøifot OMT with double ridges when the common port is excited with (a) vertically- and (b) horizontally-polarized waves.....	33

Fig. 2.13 Arrow plots of internal electric fields of the Bøifot OMT with double ridges when the common port is excited with (a) vertically and (b) horizontally-polarized waves.....	34
Fig. 2.14 Designation of cross section of the Bøifot OMT with double ridges. ....	35
Fig. 2.15 Internal electric fields of Bøifot OMT with double ridges at various cross sections.....	37
Fig. 2.16 Building blocks and dimensional parameters of the Bøifot OMT with double ridges. (a) Stepped <i>E</i> -plane bend, (b) polarization-separating junction, (c) circular <i>E</i> -plane bend, and (d) <i>Y</i> -junction power combiner. ....	40
Fig. 2.17 Simulated reflection coefficient of the stepped <i>E</i> -plane bend in a rectangular waveguide.....	41
Fig. 2.18 Performance of the polarization-separating junction with initial dimensions of the Bøifot OMT with double ridges. . ....	43
Fig. 2.19 Performance of the optimized polarization-separating junction of the Bøifot OMT with double ridges. (a) Reflection coefficient, (b) transmission coefficient and (c) polarization discrimination and isolation.. ....	44
Fig. 2.20 Performance of the circular <i>E</i> -plane bend.....	45
Fig. 2.21 Performance of the <i>E</i> -plane <i>Y</i> -junction power combiner.....	46
Fig. 2.22 Dimensions of the the Bøifot OMT with double ridges. (a) 3D view, (b) side vies and (c) top view.....	47
Fig. 2.23 Performance of the designed Bøifot OMT with double ridges. (a) Reflection coefficient, (b) isolation and polarization discrimination, and (c) transmission coefficient.....	48
Fig. 2.24 Effect of the double ridges on the impedance matching of the vertically-polarized wave in the Bøifot OMT with double ridges. ....	49

Fig. 2.25 Effects of dimensional parameters on the performance of the Bøifot OMT with double ridges.....	52
Fig. 2.26 Structure of the branch-line OMT .....	53
Fig. 2.27 (a) Structure and (b) schematic representation of a branch-line coupler. ....	54
Fig. 2.28 Schematic of the backward coupling structure with equal RL. ....	55
Fig. 2.29 Magnitude of internal electric fields of the branch-line OMT when the common port is excited with (a) vertically- and (b) horizontally-polarized waves.....	56
Fig. 2.30 Arrow plots of internal electric fields of the branch-line OMT when the common port is excited with (a) vertically and (b) horizontally-polarized waves.....	57
Fig. 2.31 Structure of a 90-degree coupler with five branch lines.....	59
Fig. 2.32 Structure of a branch-line coupler with reactive loads.....	59
Fig. 2.33 Structure of the polarization-separating junction in the branch-line OMT.....	59
Fig. 2.34 Performance of the branch-line coupler with initial dimensions. ....	61
Fig. 2.35 Performance of optimized branch-line coupler.....	63
Fig. 2.36 Performance of the designed coupler with reactive load. ....	63
Fig. 2.37 Performance of the optimized polarization-separating junction. (a) Reflection coefficient, (b) polarization discrimination and isolation, and (c) transmission coefficient. ....	64
Fig. 2.38 Structure and dimensional symbols of the two-step <i>E</i> -plane bend. ....	65
Fig. 2.39 Structure and dimensional symbols of the rounded <i>E</i> -plane bend.....	65
Fig. 2.40 Performance of the rounded <i>E</i> -plane bend.....	66
Fig. 2.41 Structure of the <i>E</i> -plane <i>Y</i> -junction.....	66

Fig. 2.42 Structure of the designed branch-line OMT. ....	67
Fig. 2.43 Performance of the designed branch-line OMT. (a) Reflection coefficient, (b) isolation and polarization discrimination, (c) transmission coefficient ....	68
Fig. 3.1 Hole patterns of the standard flange for WR-12 waveguide .....	70
Fig. 3.2 Photograph of the calibration kits .....	71
Fig. 3.3 Fabrication model of the Dunning OMT. (a) 3D model and (b) inside vies of piece II. ....	72
Fig. 3.4 Photograph of the fabricated Dunning OMT (a) Before assembly and (b) after assembly. ....	73
Fig. 3.5 Mating plane of two split blocks in the fabrication of the Bøifot OMT with double ridges.....	74
Fig. 3.6 Fabrication model for the Bøifot OMT with double ridges. (a) 3D model and (b) inside view of the split block. ....	74
Fig. 3.7 Photograph of the fabricated Bøifot OMT with double ridges. (a) Before assembly and (b) after assembly.....	75
Fig. 3.8 Mating plane of two blocks of the branch-line OMT. ....	76
Fig. 3.9 Fabrication model of the branch-line OMT. (a) 3D model and (b) internal view of a split block.....	77
Fig. 3.10 Photograph of the fabricated branch-line OMT. (a) Before assembly and (b) after assembly. ....	78
Fig. 4.1 Calibrated performance of the network analyzer. (a) Reflection and (b) transmission coefficients. ....	79
Fig. 4.2 (a) Structure and (b) photograph of the absorbing material.....	80
Fig. 4.3 Reflection coefficient of matched loads in (a) cylindrical and (b) square waveguides. ....	81

Fig. 4.4 Network analyzer measurement setup. ....	82
Fig. 4.5 Photograph of the Dunning OMT under test. ....	83
Fig. 4.6 Measured reflection coefficients of the fabricated Dunning OMT. ....	84
Fig. 4.7 Measured isolation and polarization discrimination of the fabricated Dunning OMT. ....	85
Fig. 4.8 Measured transmission coefficients of the fabricated Dunning OMT. ....	86
Fig. 4.9 Measured reflection coefficients of the fabricated Bøifot OMT with double ridges. ....	88
Fig. 4.10 Measured isolation and polarization discrimination of the fabricated Bøifot OMT with double ridges. ....	88
Fig. 4.11 Measured transmission coefficients of the fabricated Bøifot OMT with double ridges. ....	89
Fig. 4.12 Measured reflection coefficients of the fabricated branch-line OMT. ....	91
Fig. 4.13 Measured isolation and polarization discrimination of the fabricated branch- line OMT. ....	92
Fig. 4.14 Measured transmission coefficients of the fabricated branch-line OMT. ....	92

## LIST OF TABLE

Table 2.1	Design goals of the Dunning OMT.....	18
Table 2.2	Formulas for the initial dimensions of the Dunning OMT.....	22
Table 2.3	Initial dimensions of the Dunning OMT in mm.....	22
Table 2.4	Final dimensions of the Dunning OMT in mm. ....	24
Table 2.5	Design goals of the Bøifot OMT with double ridges.....	38
Table 2.6	Formulas for initial dimensions of the polarization-separating junction of the Bøifot OMT with double ridges.....	41
Table 2.7	Initial dimensions of the polarization-separating junction of the Bøifot OMT with double ridges (unit in mm).....	42
Table 2.8	Final dimensions of the designed Bøifot OMT with double ridges in mm. ....	49
Table 2.9	Design goals of the branch-line OMT.....	58
Table 3.1	Dimensions of the standard flange for WR-12 waveguide. ....	70
Table 4.1	Charfacteristic of absorber material. ....	80
Table 4.2	Comparison between design goals and perfromances of the fabricated Dunning OMT. ....	86
Table 4.3	Specified and fabricated dimensions of the Dunning OMT in mm. (a) Width and (b) Depth. ....	86
Table 4.4	Comparison between design goals and perfromances of the fabricated Bøifot OMT.....	89
Table 4.5	Specified and fabricated dimensions of the Bøifot OMT in mm. (a) Width and (b) Depth. ....	90

Table 4.6 Comparison between design goals and performances of the fabricated branch-line OMT. ....	93
Table 4.7 Specified and fabricated dimensions of the branch-line OMT in mm. (a) Width and (b) Depth. ....	93

# Chapter I

## Introduction

The orthomode transducer is one of important components in satellite communication and radio astronomy. These applications often require a dual-polarized operation and wideband operation. Fig. 1.1 shows the location of an OMT in a dual-polarized feed. From the antenna, two orthogonally-polarized waves travel through the OMT which separates two waves into their respective output ports.

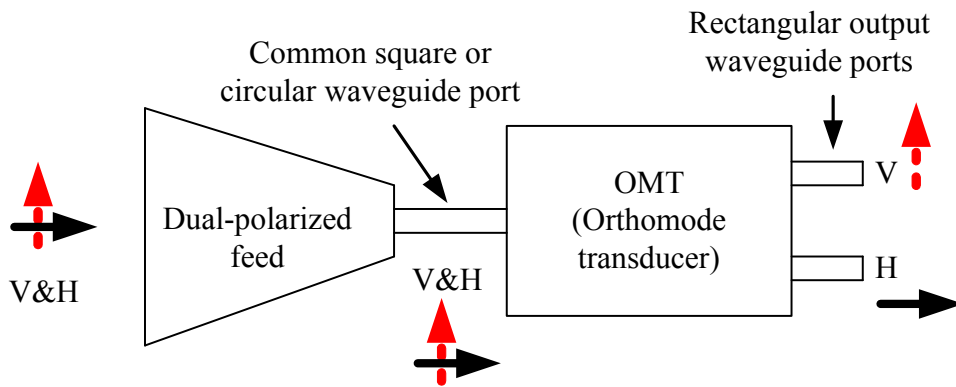


Fig. 1.1 OMT in a dual-polarized feed.

Wideband OMTs can be realized in many different forms, which include Dunning [1], Bøifot [2]-[16], branch-line [17]-[19], turnstile [20]-[31] and fin-line [32]-[34] structures. The Dunning OMT [1] is based on the simple polarization-separating junction of a T-

shaped cross section. Other parts in the Dunning OMT are a 90-degree waveguide bend and stepped waveguide impedance transformers. The practical maximum bandwidth of a Dunning OMT is 1.3:1 (26.1% bandwidth). This type of OMT does not require septa and posts. It is easy to fabricate a Dunning OMT with the split-block technique.

In recent years, the Bøifot OMT has been actively investigated by many researchers [2]-[16]. Their polarization-separating junctions take many different forms such as a septum [2]-[4], a septum and pins [5]-[10], and a ridged waveguide section [11]-[16]. Bøifot first investigated this type of OMT with a linearly-tapered septum and two pins [5]. When designing a Bøifot junction with a septum, the septum shape is very critical for wideband performance. The septum tapering in a Bøifot OMT may take circular [5], stepped [6]-[8], triangle [4]-[5] or exponential [3], [9]-[10] shapes. The bandwidth of the Bøifot OMT is around 40%. Due to a thin septum and pins, it is quite complicated to fabricate the conventional Bøifot OMT.

Some researchers have investigated and developed the Bøifot junction with a ridged waveguide section. The tapering of the ridge can be either in one direction [11], [13]-[16] or in two directions [12]. Dunning first designed and presented this type of OMT with a double-ridged waveguide section and coaxial output ports [11]. Next, Moorey designed this type of OMT with ridges tapered in two directions and with output ports in standard rectangular waveguide [12].

The branch-line OMT is based on the *E*-plane branch-line asymmetric [17] and symmetric backward coupling section [18]-[19] for polarization separation. Other structures in branch-line OMT include reactive loads, *E*-plane bends, stepped impedance

transformers and a *Y*-junction power combiner. A branch-line OMT with a symmetric coupling section is amenable to split-block fabrication. Its bandwidth is largely determined by the performance of *E*-plane branch-line coupler.

The turnstile junction can also be employed in realizing a wideband OMT. The turnstile junction has been investigated by many researchers since 1955 [20]-[21]. In the last decade, this type of OMT has been actively studied by several researchers [22]-[31]. Turnstile junctions are realized either in coaxial cable [22]-[23] or in rectangular waveguide [24]-[31]. The most important part in the design of a turnstile OMT is the tuning stub in the polarization-separating junction whose shapes include a prism [24]-[26], a pyramid [27]-[28] and a stepped cylinder [29]-[31]. The turnstile OMT is suitable for application that requires balanced phases in output ports.

The fin-line OMT is one of useful types of wideband OMT [32]-[34] but its structure is not amenable to split-block fabrication. References [35]-[36] describe another type of a wideband OMT structure consisting of many stepped transitions, a septum and a T-junction.

In this dissertation, wideband orthomode transducers operating at *E*-band (60-90GHz) are designed for use in satellite communication and radio astronomy. Design goals are as follows; easy fabrication, simple structure, bandwidth greater than 20%, reflection coefficient less than -20dB, transmission coefficient greater -0.5dB, polarization discrimination greater than 30dB and port isolation greater than 30dB. The bandwidth is defined as the frequency range over which all of the above performance goals are satisfied.

In order to meet design goal, existing wideband OMT structures are surveyed. Final wideband OMT types of choice are the Dunning structure, the Bøifot junction with double ridges, and the branch-line OMT. Existing structures are improved for easier fabrication and better performance.

In design of the Dunning OMT, stepped impedance transformers in output ports are modified to linearly-tapered ones. A circular-to-square transition is added to the common port. Formulas for calculation of initial dimensions of the Dunning OMT are presented. The whole OMT is optimized using the parameter sweep utility of the Microwave Studio<sup>TM</sup> software by CST, a well-known electromagnetic simulation software. The Microwave Studio<sup>TM</sup> is extensively employed in this dissertation for both analysis and design.

In the case of the Bøifot OMT with double ridges, formulas for the calculation of initial dimensions of the polarization-separating junction are presented. Next the side-arm combiner is designed. Finally, the whole structure is optimized. In the design of the branch-line OMT, an *E*-plane branch-line hybrid coupler is first investigated. For wideband operation, a five-section branch-line coupler is designed. A three-step reactive load is attached to coupled and through ports of the coupler. The symmetric backward coupling section is realized using two *E*-plane branch-line couplers. A circular-to-square waveguide transition is added to the common port. Finally the whole structure is constructed by combining sub-structures designed already.

The designed Dunning OMT has an inner dimension ( $L \times W \times H$ ) of 13.21mm x 3.1mm x 7.69mm and a bandwidth of 25.5%. The designed Bøifot and branch-line OMTs

have inner dimensions of 24.48mm x 14.07mm x 6.98mm and 30.29mm x 18mm x 6.32mm, and bandwidths of 42% and 28.9%, respectively. The designed OMTs are fabricated with the split-block technique. The fabricated OMTs are tested and measured performances are compared with the simulation.

This dissertation consists of five chapters. A brief outline of each chapter is given in the following. Chapter II deals with the design and optimization of a Dunning OMT, a Bøifot OMT with double ridges, and a branch-line OMT. The operating principles and structures of these OMTs are presented. Detailed descriptions of design procedures of each OMT are provided. Chapter III discusses the fabrication of the designed OMTs. In Chapter IV, an analysis of the simulated and measured performances is given. Finally Chapter V provides the discussion and conclusions.

## Chapter II

### Design of Wideband Orthomode Transducers

In this chapter, the design of the wideband orthomode transducer is described. First, specifications and the operating principle of a general OMT are explained. Section 2.2 deals with the design of a wideband Dunning OMT. The structure and theory of operation of the Dunning OMT are presented. The original structure of the Dunning OMT is improved for easier fabrication. Formulas for initial dimensions of the Dunning OMT are presented. Design procedures and results of the optimized design are described. Section 2.3 deals with the Bøifot OMT with double ridges. The design and optimization of this OMT are presented in a manner similar to the case of the Dunning OMT. Section 2.4 deals with the design and optimization of the branch-line OMT.

#### 2.1 Structure and Specifications of an OMT

The structure of a generic OMT is shown in Fig. 2.1. An OMT is a four-port device with three physical waveguide ports. The common waveguide in Fig. 2.1 supports two modes with horizontal and vertical polarizations, which are routed to the straight (port 3) and side (port 2) output waveguides. The common waveguide may also be of circular type. The polarization-separating structure is connected to the common waveguide. In Fig. 2.1, the polarization-separating structure consists of a stepped-waveguide and a slot. The

polarization-separating structure may take many different forms. The common waveguide dimension may be reduced in multiple steps before it is connected to the polarization-separating junction. This is done to prevent the local generation of higher-order modes, which leads to spikes in reflection and transmission performances of the OMT.

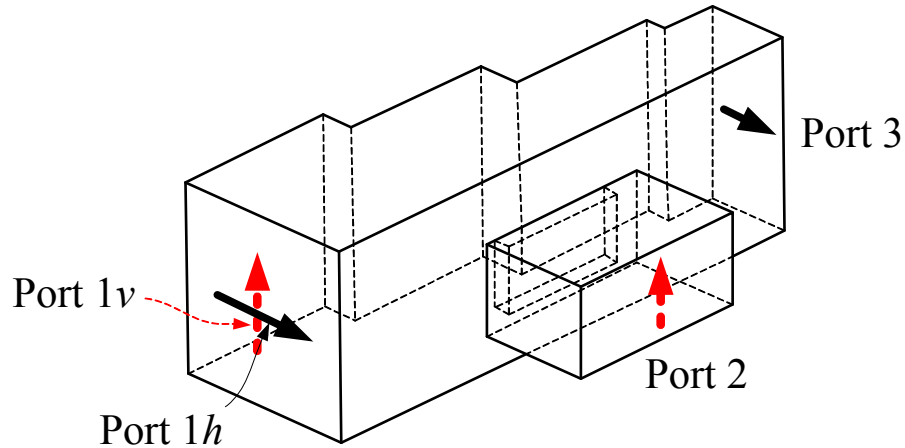


Fig. 2.1 Structure of a generic OMT [37].

In Fig. 2.1, the vertically-polarized wave ( $1v$ ) in the common waveguide is directed to the side port through an aperture on the wall of the square waveguide. The horizontally-polarized wave is prevented from entering the side port by the proper orientation of the slot aperture and the side-port waveguide. The horizontally-polarized wave is transmitted to the straight port. The width of the square waveguide is reduced in multiple steps in such a way that the horizontally-polarized wave ( $1h$ ) is transmitted to the straight port almost without any obstruction, while the vertically-polarized one is blocked by the cut-off dimension of the waveguide with a reduced width. Impedance matching structures

such as stepped or linearly-tapered waveguide sections, irises and posts may be used between the polarization-separating junction and the output waveguide. With a port numbering of Fig. 2.1, the scattering matrix of an ideal OMT is given by

$$[S] = \begin{bmatrix} S_{1v,1v} & S_{1v,1h} & S_{1v,2} & S_{1v,3} \\ S_{1h,1v} & S_{1h,1h} & S_{1h,2} & S_{1h,3} \\ S_{2,1v} & S_{2,1h} & S_{22} & S_{23} \\ S_{3,1v} & S_{3,1h} & S_{32} & S_{33} \end{bmatrix} = \begin{bmatrix} 0 & 0 & 1 & 0 \\ 0 & 0 & 0 & 1 \\ 1 & 0 & 0 & 0 \\ 0 & 1 & 0 & 0 \end{bmatrix} \quad (2.1)$$

Specifications of an OMT consist of the reflection coefficient, transmission coefficient, polarization discrimination, port isolation and passive inter-modulation distortion (PIMD).

*Reflection coefficient:* The amplitude ratio of reflected to incident waves at each port is called the reflection coefficient. In (2.1), they are  $|S_{1v,1v}|$ ,  $|S_{1h,1h}|$ ,  $|S_{22}|$  and  $|S_{33}|$ . Typical specifications call for a reflection coefficient less than -20dB over the operating bandwidth.

*Transmission coefficient:* The amplitude ratio of the wave at the output port to the corresponding vertically or horizontally-polarized incident wave at the common port is called the magnitude of transmission coefficient. In (2.1), they are  $|S_{1v,2}| = |S_{2,1v}|$  and  $|S_{1h,3}| = |S_{3,1h}|$ . Typical specifications call for a magnitude of transmission coefficient greater than -0.5dB.  $\text{Arg}(S_{1v,2}) = \text{Arg}(S_{2,1v})$  and  $\text{Arg}(S_{1h,3}) = \text{Arg}(S_{3,1h})$  are the phases of transmission coefficients. For signals not to be distorted after being transmitted through an OMT, the magnitude of transmission coefficient should be constant over its bandwidth, while the phase should vary linearly with the frequency.

*Port isolation:* The amplitude ratio of the vertically or horizontally-polarized incident wave at the common port to the wave at the output port of the other polarization is called the port isolation. In (2.1), they are  $|S_{23}| = |S_{32}|$ . When an OMT is used in a single-antenna communication device, one of the output ports is connected to the transmitter, while the other to the receiver. In this case one has to increase the isolation as much as possible since the transmitter's sidebands increase the receiver noise. Typical applications require an isolation of 30dB or greater.

*Polarization discrimination:* The degree to which a wave of unwanted polarization is transmitted or received is called the polarization discrimination. In (2.1), they are  $|S_{1h,2}| = |S_{3,h}|$  and  $|S_{1v,3}| = |S_{3,v}|$ . In Fig. 2.1, when a vertically polarized wave, for example, is incident on the common waveguide, most of the wave power will be routed to the side port. But a very small fraction of the power will appear at the straight port where a horizontally-polarized wave incident on the common waveguide is transmitted without loss. In a reverse situation, when the straight port is excited, most of its power will appear at the common port as a horizontally-polarized wave, while a very small vertically-polarized wave will also appear at the common port. Requirements of the polarization discrimination vary depending on particular applications. Typical specifications call for a polarization discrimination of 30dB or better.

*Passive inter-modulation distortion (PIMD):* When an OMT is used as a component in a single-antenna transmitter and receiver application, there will be inter-modulation products generated at the flange contacts and junctions between different metal surfaces. Inter-modulation components that fall within the receiver frequency band is radiated or

routed through the receiver port of an OMT and acts like a noise. PIMD can be suppressed to a sufficiently low level by careful selection of materials and by use of clean, polished and flat mating surfaces.

## 2.2 Dunning OMT

The Dunning OMT is invented by A. Dunning in 2009 [1]. A Dunning OMT consists of an input section, a polarization separating junction and output sections. In the original invention, Dunning used a common waveguide of square shape and stepped impedance transformers for output ports. In this dissertation, a circular-to-square waveguide transition is employed to obtain a circular common port which is suitable for connecting a circular horn for use as a reflector antenna feed. For easier fabrication, linearly-tapered sections are used for output ports instead of stepped impedance transformers in the original Dunning structure.

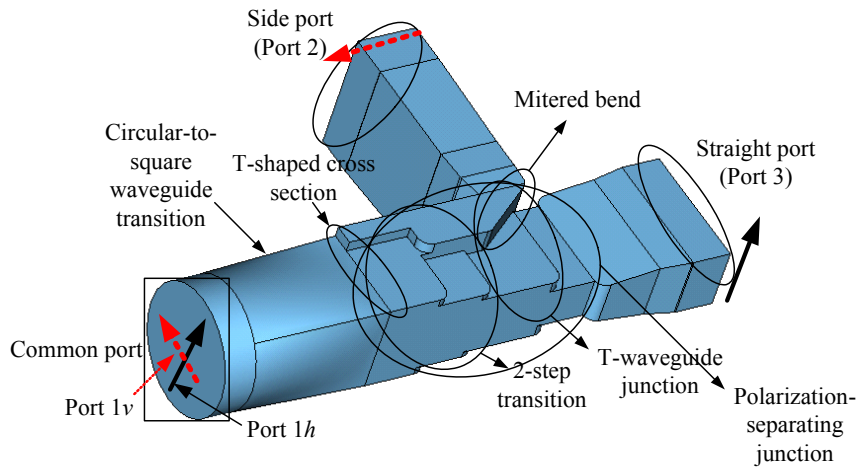
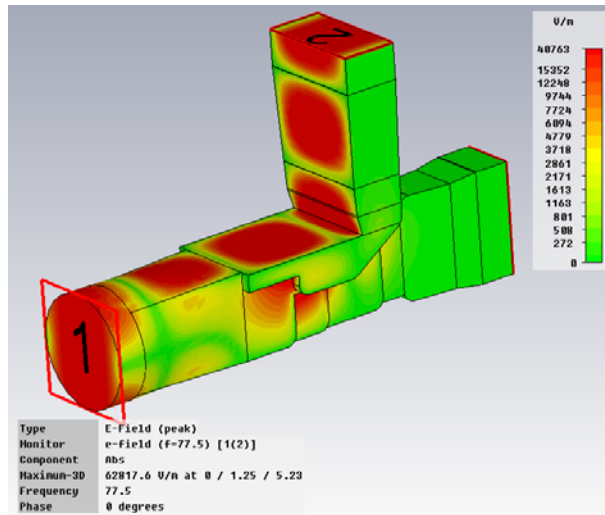


Fig. 2.2 Structure of a Dunning OMT.

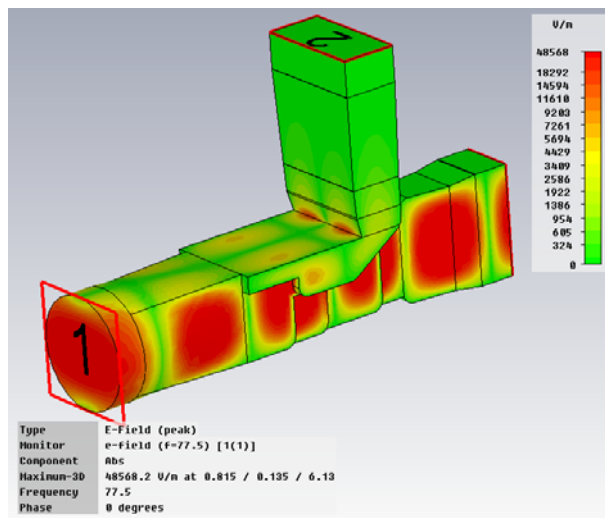
Fig. 2.2 shows an improved Dunning OMT developed in this work. The width of the square waveguide of the common port is reduced to smaller sizes in three steps and at the same time the  $T$ -shaped waveguide is introduced for coupling of the vertically-polarized wave ( $1\nu$  in Fig. 2.2). The width and height of the straight section of the polarization-separating junction are increased into those of the straight port output waveguide using two linearly tapered impedance matching sections.

The height of the upper part in the  $T$ -shaped cross section is increased in one step forming a rectangular waveguide that couples the vertically-polarized wave ( $1\nu$  in Fig. 2.2). A mitered 90-degree bend is used to change the direction of this waveguide forming the side port. The height and width of the waveguide is again increased into those of the side port waveguide using three linearly-tapered impedance matching sections. Waveguides at the side and straight ports are usually of standard type (i.e., WR-series). The bandwidth of the Dunning OMT is largely determined by the performance of the polarization separating junction, in the design of which one has to pay careful attention so that higher-order modes are not excited.

To better understand the operating principles of the Dunning OMT, the Microwave Studio<sup>TM</sup> is used to obtain field distributions inside the OMT. Fig. 2.3(a) is the case of the common port excited with a vertically-polarized wave. Almost all of the common port power is delivered to the side port, while negligible power comes out of the straight port. A similar observation can be made for the case where the common port is excited with a horizontally-polarized wave shown in Fig. 2.3(b).



(a)



(b)

Fig. 2.3 Operation of the Dunning OMT with the common port excited with (a) a vertically-polarized wave and (b) a horizontally-polarized wave.

The core of the Dunning OMT is the polarization separating junction, the understanding of which is sufficient for the understanding of the operating principle of the Dunning OMT. The graphical description of the operation of the polarization separating junction is depicted in Fig. 2.5. In Fig. 2.4, various cross sections are designated with a letter. Two-dimensional arrow plots of the electric field are given on each cross section in Fig. 2.5. The plots are obtained for each polarization at the center frequency using Microwave Studio<sup>TM</sup>. In Fig. 2.5, plots on the left column are electric fields due to a vertically polarized wave ( $1v$  or  $TE_{11,0^\circ}$ ) incident on the common circular waveguide, while those on the right due to a horizontally polarized wave ( $1h$  or  $TE_{11,90^\circ}$ ).

With the common port excited with a vertically-polarized wave, from field distributions on cross sections A to K in Fig. 2.5, one can see that almost all of the vertically-polarized wave power is routed to the side port and that negligible power comes out of the straight port. The maximum electric fields at the side port (the left plot of Fig. 2.5(k)) and straight port (the left plot of Fig. 2.5(j)) are 14,260 V/m and 37.5 V/m respectively when one watt of the vertically-polarized wave is incident on the common port. The polarization discrimination in this case can be calculated as

$$-20\log_{10}|S_{1v,3}| = -10\log_{10}\frac{P_3}{P_{1v}}\frac{P_{1v}}{P_2} = -10\log_{10}\frac{P_3}{P_2} = -20\log_{10}\frac{E_3}{E_2} = -20\log_{10}\frac{37.5}{14260} = 51.6 \text{ dB.}$$

A similar observation can be made in case of the common port excited with a horizontally-polarized wave. The maximum electric fields at the side port (the right plot of Fig. 2.5(k)) and straight port (the right plot of Fig. 2.5(j)) are 37.0 V/m and 14,226 V/m respectively when one watt of the horizontally-polarized wave is incident on the

common port. The polarization discrimination in this case can be calculated as

$$-20\log_{10}|S_{1h,2}| = -10\log_{10}\frac{P_2}{P_{1v}}\frac{P_{1v}}{P_3} = -10\log_{10}\frac{P_2}{P_3} = -20\log_{10}\frac{E_2}{E_3} = -20\log_{10}\frac{37.0}{14226} = 51.7 \text{ dB.}$$

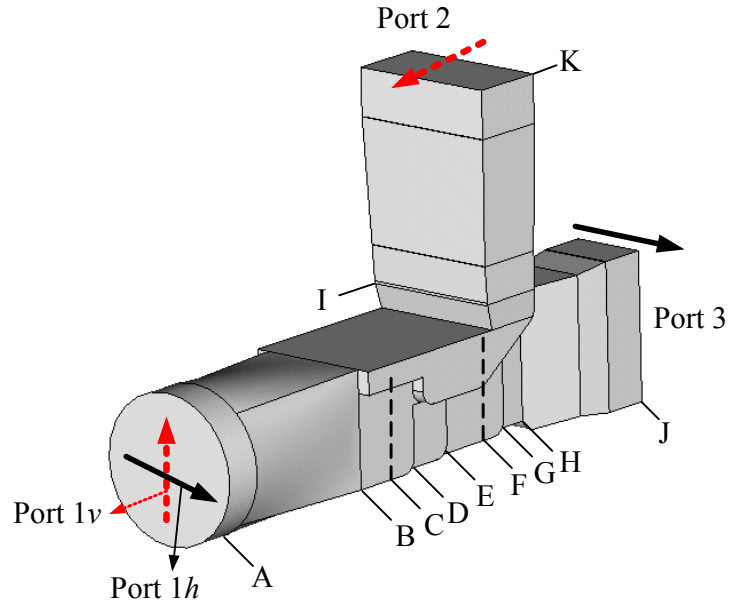
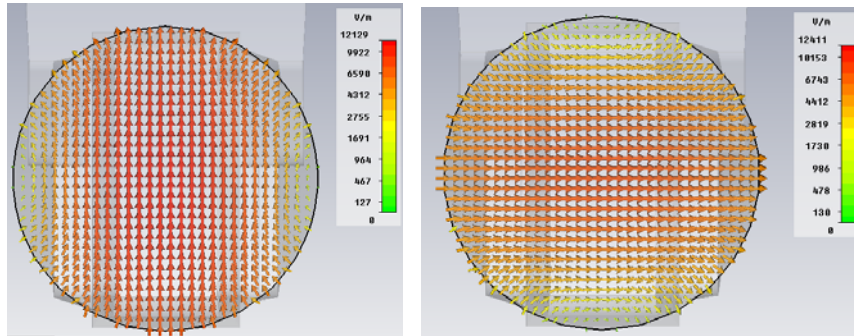
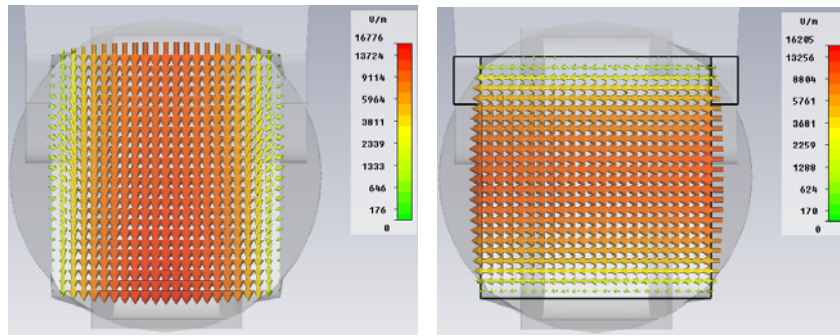


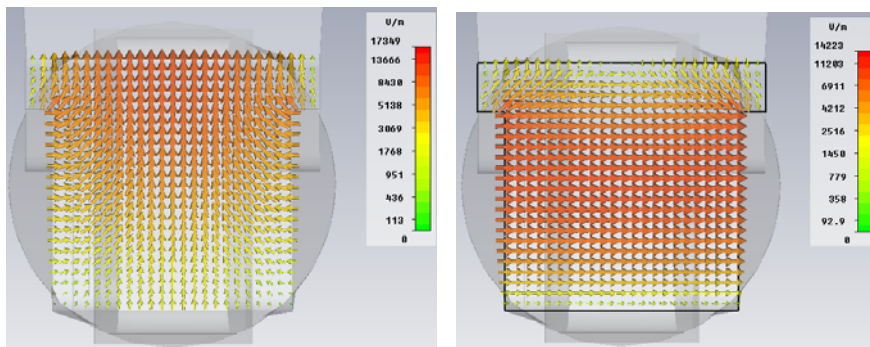
Fig. 2.4 Designation of the cross sections of the Dunning OMT.



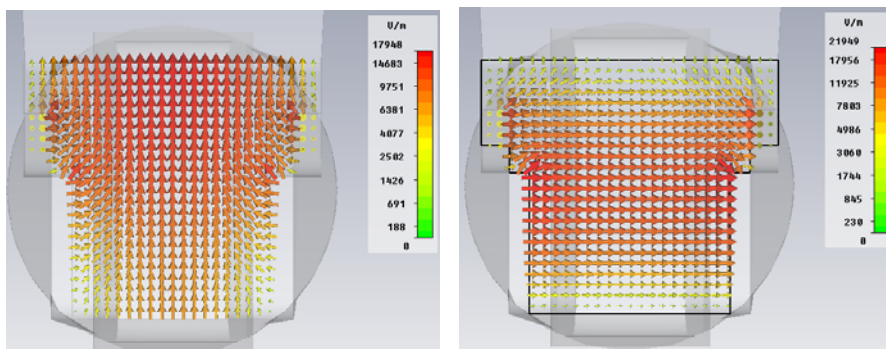
(a) Electric field at cross section A



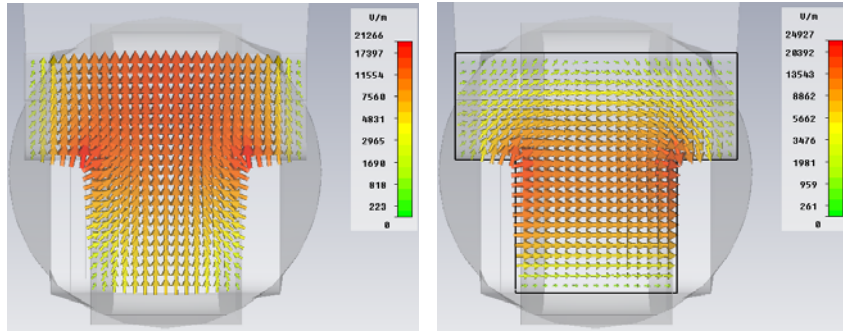
(b) Electric field at cross section B



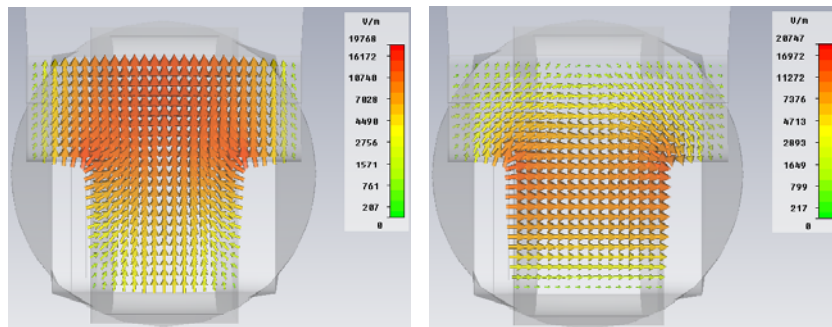
(c) Electric field at cross section C



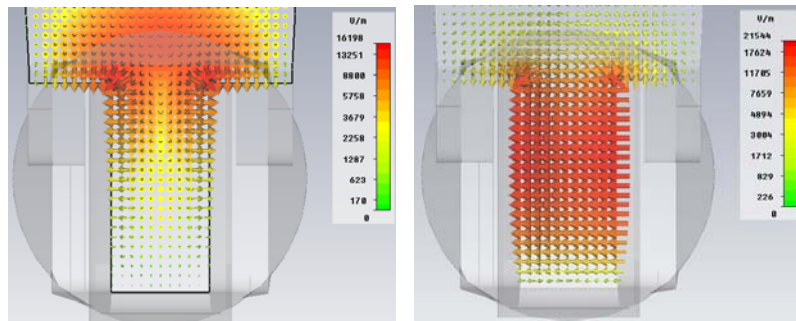
(d) Electric field at cross section D



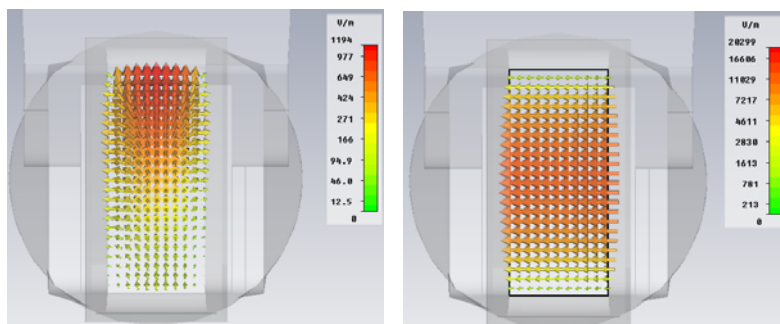
(e) Electric field at cross section E



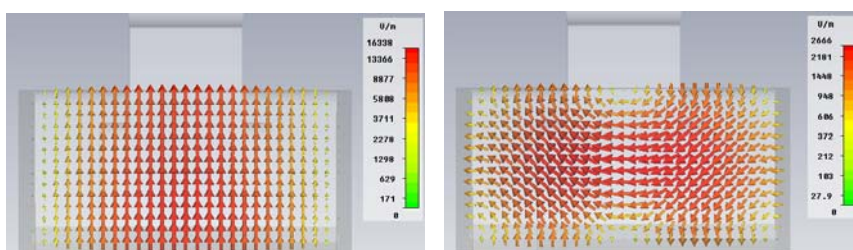
(f) Electric field at cross section F



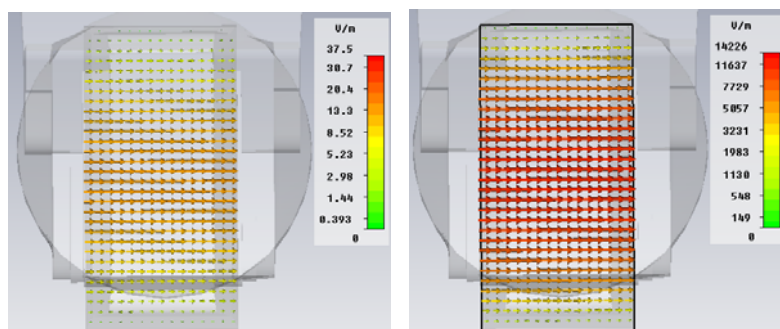
(g) Electric field at cross section G



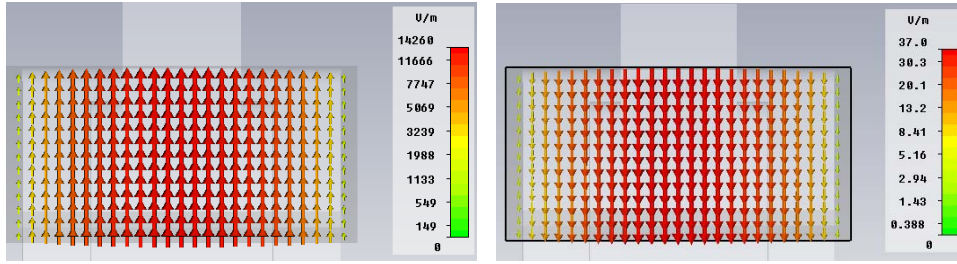
(h) Electric field at cross section H



(i) Electric field at cross section I



(j) Electric field at cross section J



(k) Electric field at cross section K

Fig. 2.5 Internal electric fields of the Dunning OMT at various cross sections.

Table 2.1 shows the design goals of the Dunning OMT which include the reflection coefficient, transmission coefficient, port isolation, polarization discrimination and operating bandwidth.

Table 2.1 Design goals of the Dunning OMT.

Performance	Design goal
Reflection ( $R$ )	$\leq -20\text{dB}$
Transmission ( $T$ )	$\geq -0.5\text{dB}$
Isolation ( $I$ )	$\geq 30\text{dB}$
Discrimination ( $D$ )	$\geq 30\text{dB}$
Bandwidth ( $B$ )	70-87GHz

Fig. 2.6 shows symbols designating dimensions of the Dunning OMT. Initial dimensions are obtained by applying simple waveguide theory. Sizes of the circular and square waveguides are determined so that the cutoff frequency of the dominant mode is lower than the lowest frequency of operation. The operating frequency of the Dunning OMT to be designed is from 70 ( $f_1$ ) to 87( $f_2$ ) GHz. The recommended operating frequency range of a circular waveguide is given by

$$1.15f_{c,TE_{11}} \leq f \leq 0.95f_{c,TE_{21}} = 1.58f_{c,TE_{11}} \quad (2.2)$$

The following equation is used to find  $f_{c,TE_{11}}$ , whose calculated value is 57.5GHz.

$$\frac{1.15f_{c,TE_{11}} + 1.58f_{c,TE_{11}}}{2} = \frac{f_1 + f_2}{2} = 78.5 \text{ GHz} \quad (2.3)$$

The operating frequency range of the circular waveguide is then from 66.13GHz to 90.86GHz which adequately covers the desired frequency band 70-87GHz. Now, the circular waveguide diameter  $d$  can be calculating by following formula [38]

$$f_{c,TE_{11}} = \frac{p'_{11}c}{2\pi d} \quad (2.4)$$

where  $p'_{11} = 1.841$  and  $c$  is the speed of light in vacuum. From (2.4),  $d$  is calculated to be 3.05mm. Instead of this value, a more convenient value of 3.10mm is used, in which case the operating frequency of the circular waveguide is  $65.2\text{GHz} \leq f \leq 89.6\text{GHz}$ .

The dimension of the square waveguide is set to a minimum value so that higher-order modes in the polarization-separating junction are suppressed as much as possible. The lowest operating frequency is set equal to 1.1 times the cutoff frequency, viz.,

$$f_1 = 1.1f_{c,TE_{10}} \quad (2.5)$$

The cutoff frequency of a square waveguide  $f_{c,TE_{10}}$  is calculating by following formula [38]

$$f_{c,TE_{10}} = \frac{c}{\lambda_c} = \frac{c}{2a} \quad (2.6)$$

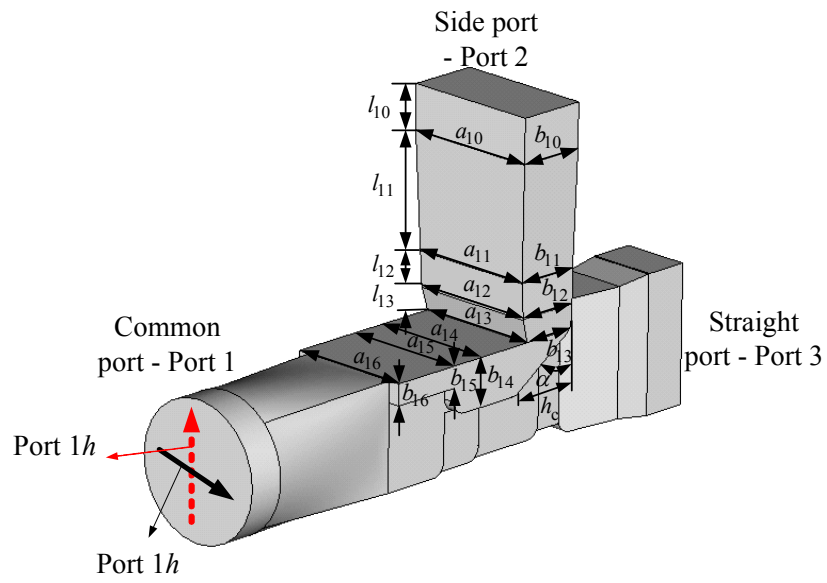
where  $a$  is the width of the waveguide. From (2.6) it is found that  $a = 2.36\text{mm}$ . The output ports are the standard rectangular waveguide WR-12 where  $a_0=a_{10}=3.10\text{mm}$  and  $b_0=b_{10}=1.55\text{mm}$ .

The initial lengths of all waveguide sections in Fig. 2.6 are the one quarter of a guided wavelength ( $\lambda_g/4$ ) at the center frequency (78.5GHz) except  $l_9$ . The guided wavelength of the TE<sub>10</sub> mode of a rectangular waveguide is given by [38]

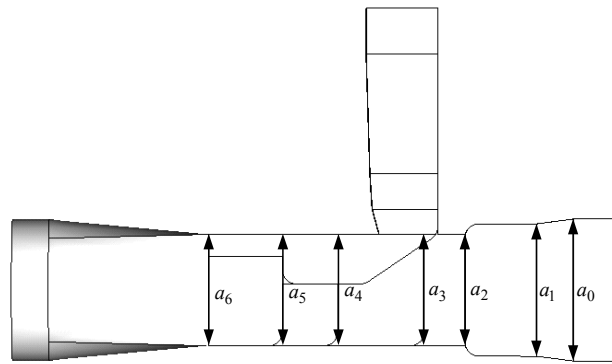
$$\lambda_g = \frac{\lambda_0}{\sqrt{1 - \left(\frac{\lambda_0}{2a}\right)^2}} \quad (2.7)$$

where  $\lambda_0$  is the wavelength in vacuum.

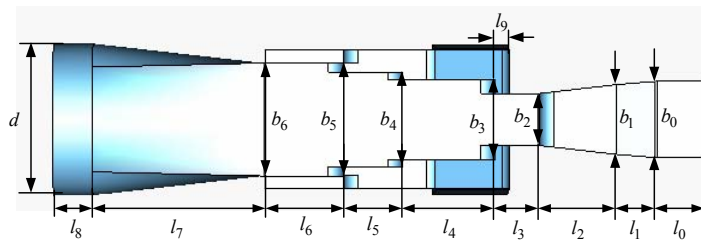
The  $l_9$  is set to be equal to  $\lambda_g/9$ . In Fig. 2.6, it can be seen that values  $a_2$  to  $a_6$  are same, and that  $b_5$  and  $b_6$  are same. Formulas in Table 2.2 are also used in finding initial dimensions. The calculated initial dimensions of the Dunning OMT are shown in Table 2.3. Starting with initial dimensions, the parameter sweep utility in Microwave Studio™ is employed to arrive at the final design.



(a)



(b)



(c)

Fig. 2.6 Dimensions of the Dunning OMT. (a) 3D view, (b) side view and (c) bottom view.

Table 2.2 Formulas for initial dimensions of the Dunning OMT.

Parameter	Formula
$b_2$	$b_5/2$
$b_4$	$b_5-(b_5-b_2)/3$
$b_3$	$b_4-(b_5-b_2)/3$
$b_1$	$(b_2+b_0)/2$
$a_1$	$(a_2+a_0)/2$
$a_{16}$	$b_6+\lambda_g/14$
$a_{11}$	$(a_{10}+a_{13})/2$
$a_{12}$	$(a_{10}+a_{13})/2$
$b_{13}$	$\lambda_g/5$
$b_{11}$	$b_{10}-(b_{10}-b_{13})/3$
$b_{12}$	$b_{11}-(b_{10}-b_{13})/3$
$b_{14}$	$a_6/2.2$
$b_{16}$	$a_6/5$
$\alpha$	$45^\circ$
$h_c$	$b_{14}$

Table 2.3 Initial dimensions of the Dunning OMT in mm.

$a_0$	$a_1$	$a_2$	$a_3$	$a_4$	$a_5$	$a_6$	$a_{10}$	$a_{11}$	$a_{12}$	$a_{13}$	$a_{14}$	$a_{15}$	$a_{16}$	$b_0$
3.1	2.73	2.36	2.36	2.36	2.36	2.36	3.1	2.96	2.96	2.82	2.82	2.82	2.82	1.55
$b_1$	$b_2$	$b_3$	$b_4$	$b_5$	$b_6$	$b_{10}$	$b_{11}$	$b_{12}$	$b_{13}$	$b_{14}$	$b_{15}$	$b_{16}$	$l_0$	$l_1$
1.37	1.18	1.57	1.96	2.36	2.36	1.55	1.46	1.38	1.3	1.07	0.47	0.47	1.62	1.62
$l_2$	$l_3$	$l_4$	$l_5$	$l_6$	$l_7$	$l_8$	$l_9$	$l_{10}$	$l_{11}$	$l_{12}$	$l_{13}$	$d$	$\alpha$	$h_c$
1.62	1.62	1.62	1.62	1.62	1.62	1.62	0.3	1.62	1.62	1.62	1.62	3.1	$45^\circ$	1.07

The performance of the Dunning OMT with initial dimensions of Table 2.3 is shown in Fig. 2.10. The reflection coefficients at the common and output ports are not less than -20dB over 70-87GHz. The reflection coefficients increase sharply at 90.6GHz, which is

close to the cutoff frequency of TE<sub>11</sub> mode of the square waveguide. With  $a = b = 2.36\text{mm}$ , the cutoff frequency of TE<sub>11</sub> mode of a square waveguide is given by

$$f_{c,TE_{11}} = \sqrt{2} \frac{c}{2a} = 89.87\text{GHz} \quad (2.8)$$

Due to high reflection coefficients, co-polarization transmission coefficients are not maximized. Isolation and polarization discrimination performances are good.

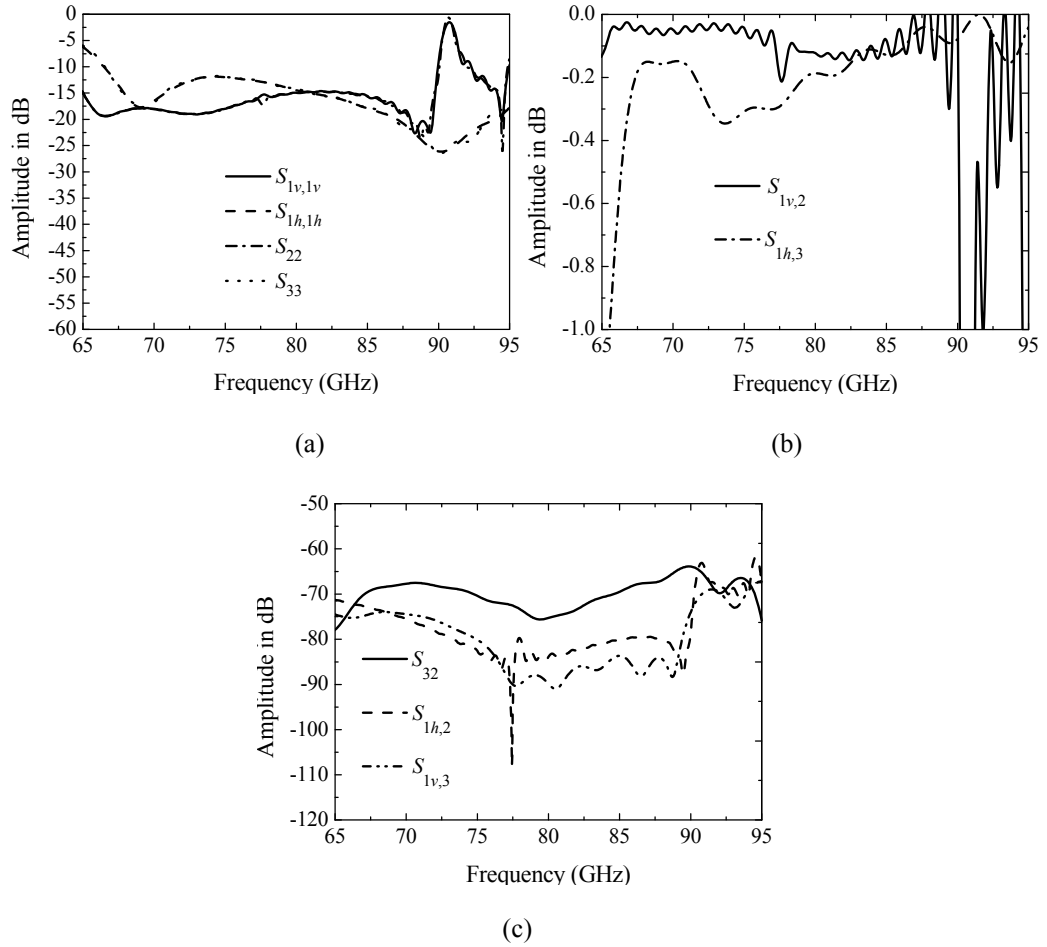


Fig. 2.7 Performance of the Dunning OMT with initial dimensions. (a) Reflection coefficient, (b) transmission coefficient and (c) isolation and polarization discrimination.

Using the parameter sweep function of Microwave Studio<sup>TM</sup>, OMT dimensions are optimized. The performance of the optimized Dunning OMT is shown in Fig. 2.8. Table 2.4 shows final optimized dimensions of the designed OMT. Over 68.5-88.5GHz (25.47% bandwidth), the reflection coefficient is less than -20dB at all ports, the transmission coefficient is greater than -0.5dB, the polarization discrimination and isolation are greater than 40dB. With ports 1<sub>v</sub> (vertically-polarized wave at the common waveguide) or 2 (side port) excited, there is a local resonance at around 90GHz, which is the cutoff frequency of TE<sub>11</sub> mode of the square waveguide.

Table 2.4 Final dimensions of the designed Dunning OMT in mm.

$a_0$	$a_1$	$a_2$	$a_3$	$a_4$	$a_5$	$a_6$	$a_{10}$	$a_{11}$	$a_{12}$	$a_{13}$	$a_{14}$	$a_{15}$	$a_{16}$	$b_0$
3.1	2.89	2.43	2.43	2.43	2.43	2.43	3.1	2.9	2.9	2.84	2.84	2.84	2.84	1.55
$b_1$	$b_2$	$b_3$	$b_4$	$b_5$	$b_6$	$b_{10}$	$b_{11}$	$b_{12}$	$b_{13}$	$b_{14}$	$b_{15}$	$b_{16}$	$l_0$	$l_1$
1.42	1.06	1.63	1.92	2.3	2.3	1.55	1.47	1.42	1.27	1.08	0.48	0.48	1	0.8
$l_2$	$l_3$	$l_4$	$l_5$	$l_6$	$l_7$	$l_8$	$l_9$	$l_{10}$	$l_{11}$	$l_{12}$	$l_{13}$	$d$	$\alpha$	$h_c$
1.55	0.9	1.88	1.2	1.6	3.42	0.8	0.29	1	2.6	0.78	0.55	3.1	45	1.7

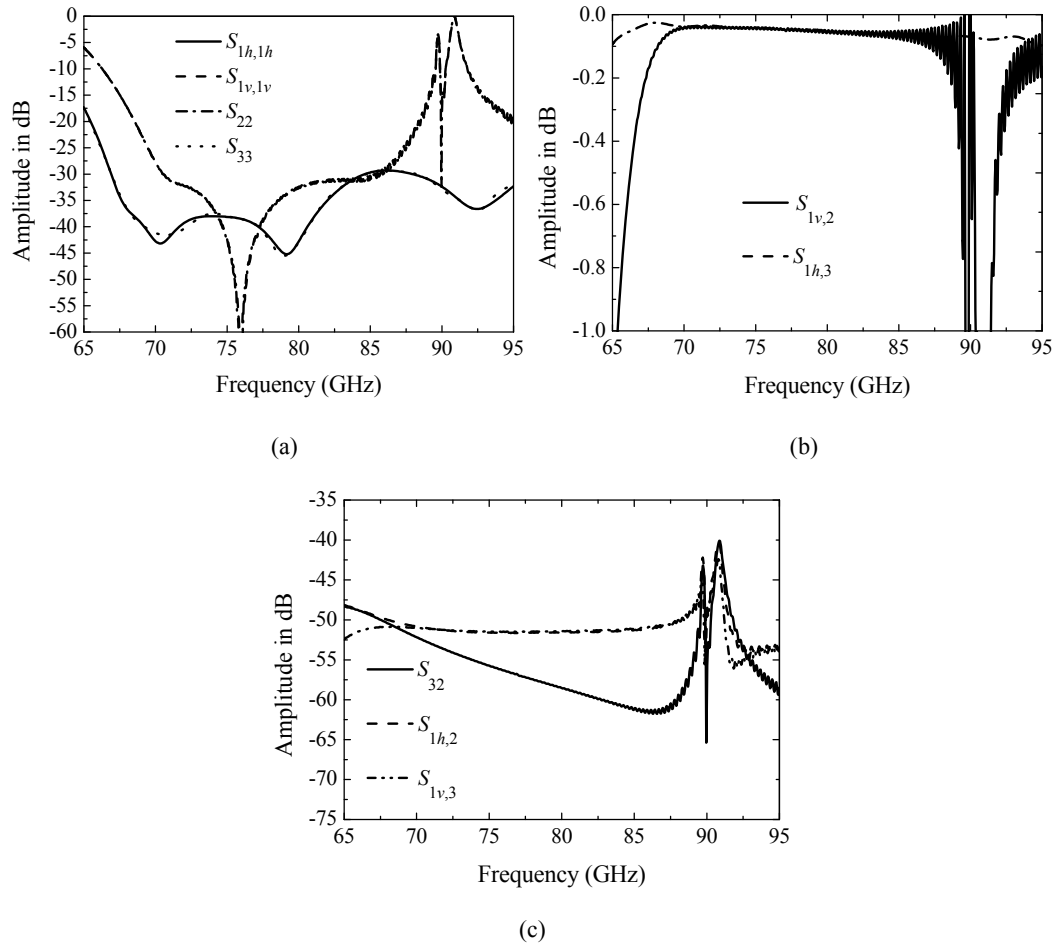


Fig. 2.8 Performance of the designed Dunning OMT. (a) Reflection coefficients, (b) transmission coefficients and (c) polarization discrimination and isolation.

Fig. 2.9 shows reflection coefficients versus important dimensional parameters of the Dunning OMT. In order to reach an optimum design, one initially has to perform parametric studies and find a set of important parameters. Then the parameter sweep is carried only for the set of important parameters.

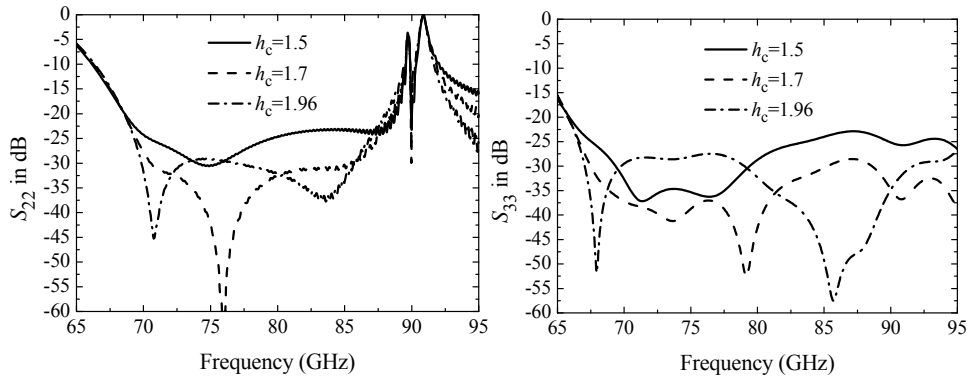
First the effect of the miter's horizontal length  $h_c$  (accordingly the miter angle  $\alpha$  if necessary) is plotted in Fig. 2.9(a). The parameter  $h_c$  has not much effect on the bandwidth. Levels of reflection coefficients are sensitive to the changes in  $h_c$ .

The square waveguide width  $a_6$  (with its height  $b_6$  unchanged) has a significant effect on the level of  $S_{33}$  since it introduces a deviation from the optimized stepped impedance transformer. The parameter  $a_6$  has a minor effect on the level of  $S_{22}$ . When  $a_6$  is increased, the spike in  $S_{22}$  is shifted to a lower frequency due to the lowering of the  $TE_{11}$  mode cutoff frequency.

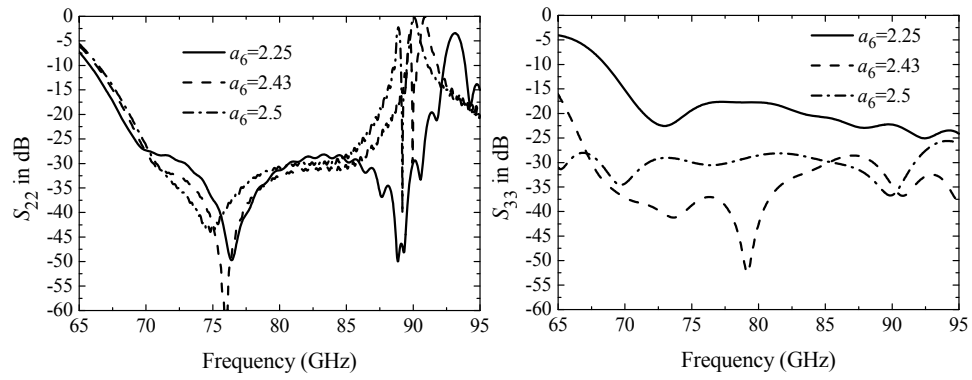
If the square waveguide height  $b_6$  (with its width  $a_6$  unchanged) is increased, the spike in  $S_{22}$  is shifted to a lower frequency and the level of  $S_{22}$  is increased. The parameter  $b_6$  has a minor effect on the level of  $S_{33}$  since it does not perturb the stepped impedance transformer for the straight port.

If the parameter  $a_{16}$  in the T-waveguide section is increased, the level of  $S_{33}$  is changed and the spike in  $S_{22}$  is shifted to a lower frequency. The parameter  $a_{16}$  in combination with the square waveguide width and height determines the cutoff frequency of  $TE_{11}$  mode of the square waveguide guide in the polarization-separating junction.

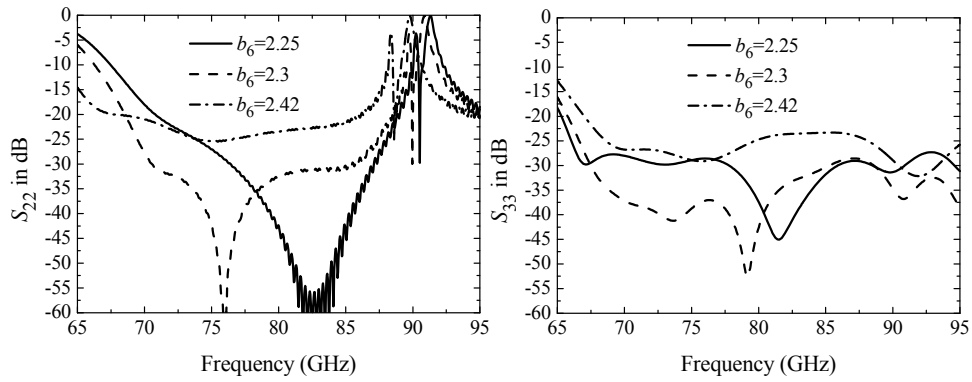
The parameters  $b_{16}$  and  $b_{14}$  have some effects on the level of reflection coefficients. The parameters  $b_2$  and  $b_3$  have a significant effect on the level of  $S_{33}$  but has a minor effect on the level of  $S_{22}$ .



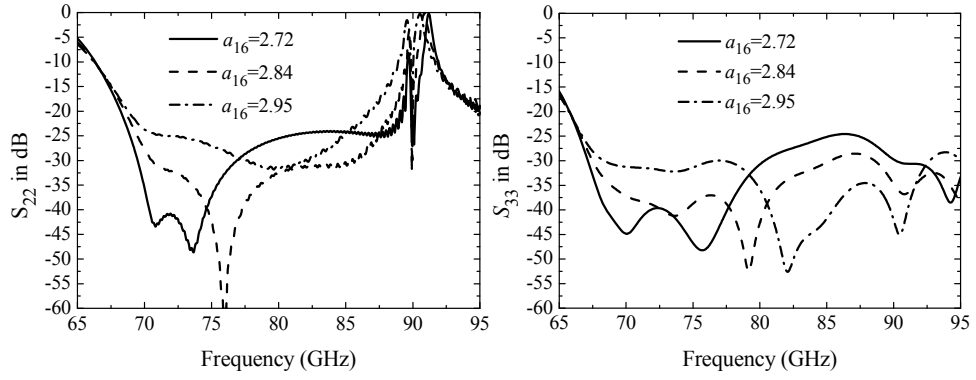
(a) Effect of  $h_c$  on the performance of the Dunning OMT



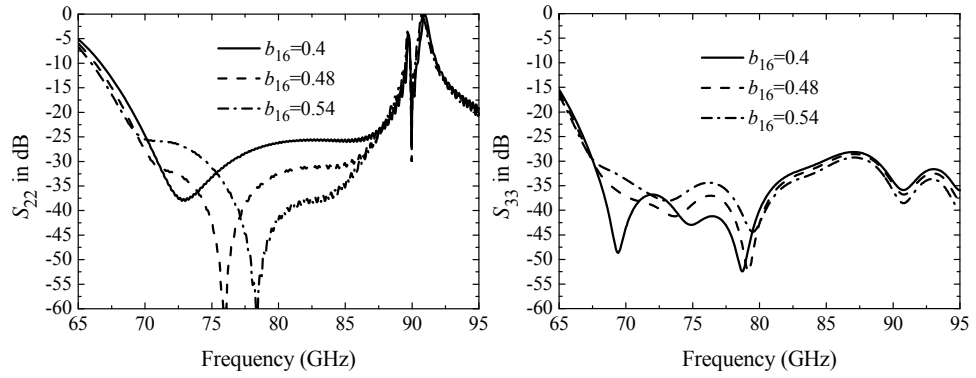
(b) Effect of  $a_6$  on the performance of the Dunning OMT



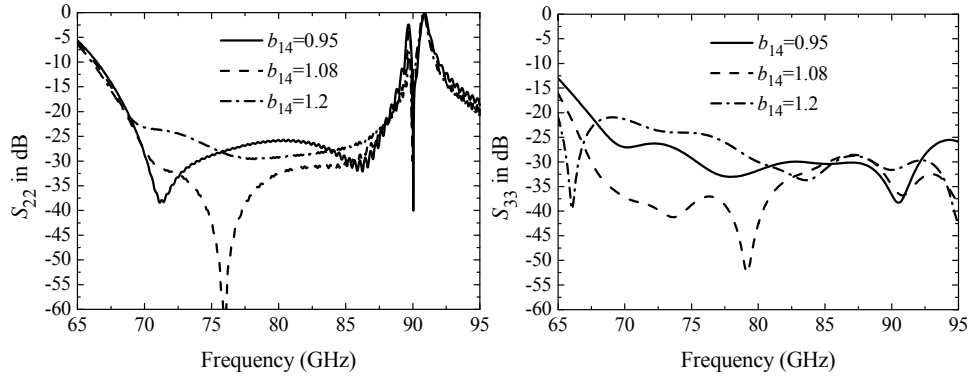
(c) Effect of  $b_6$  on the performance of the Dunning OMT



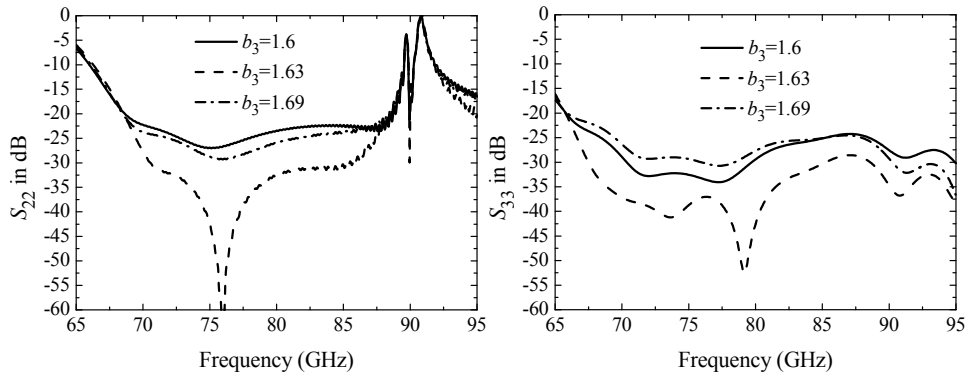
(d) Effect of  $a_{16}$  on the performance of the Dunning OMT



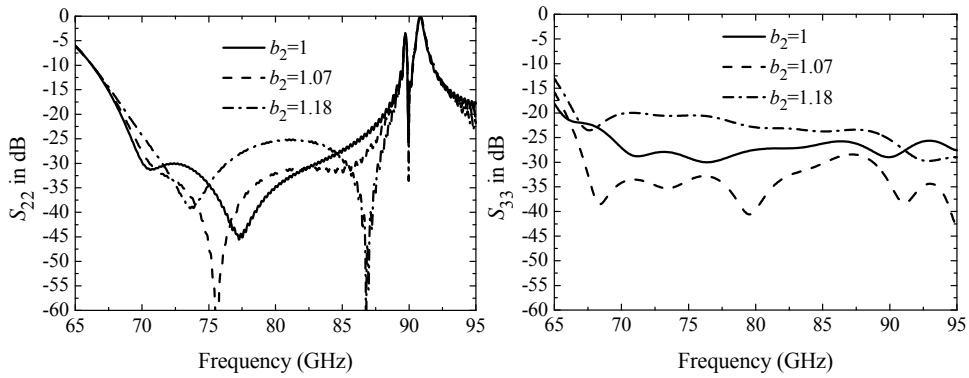
(e) Effect of  $b_{16}$  on the performance of the Dunning OMT.



(f) Effect of  $b_{14}$  on the performance of the Dunning OMT



(g) Effect of  $b_3$  on the performance of the Dunning OMT



(i) Effect of  $b_2$  on the performance of the Dunning OMT

Fig. 2.9 Effects of dimensional parameters on the reflection coefficient of the Dunning OMT.

### 2.3 Bøifot OMT with Double Ridges

The original Bøifot OMT shown in Fig. 2.10 is invented by A. M. Bøifot in 1991 [5]. The Bøifot OMT with a septum and pins has been actively investigated by many researchers [2]-[10]. The common waveguide is of square shape.

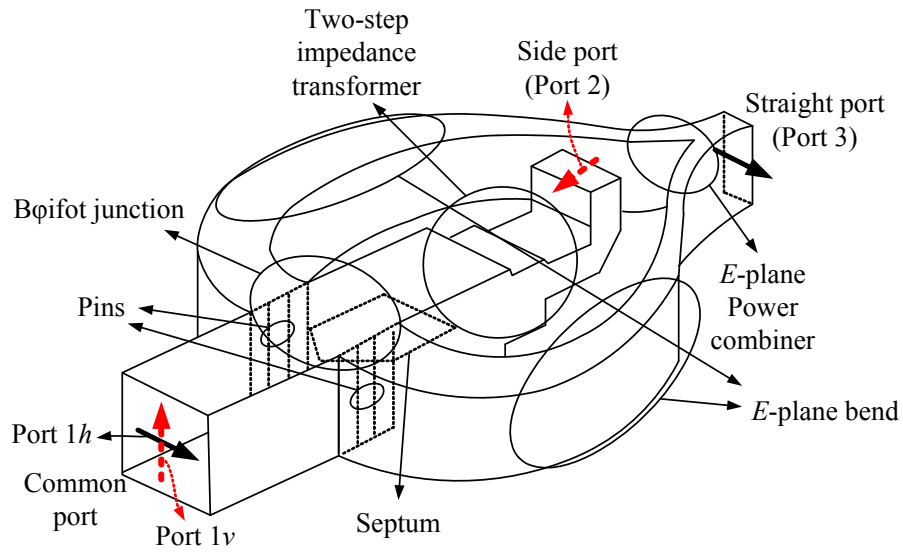


Fig. 2.10 Structure of the original Bøifot OMT [5].

The polarization-separating junction consists of a thin metallic septum and two symmetric side-wall apertures with impedance matching posts. Beyond the septum, the height of the square waveguide is reduced in multiple steps. A mitered  $E$ -plane bend is used to change the direction of the output waveguide for the vertically-polarized wave.

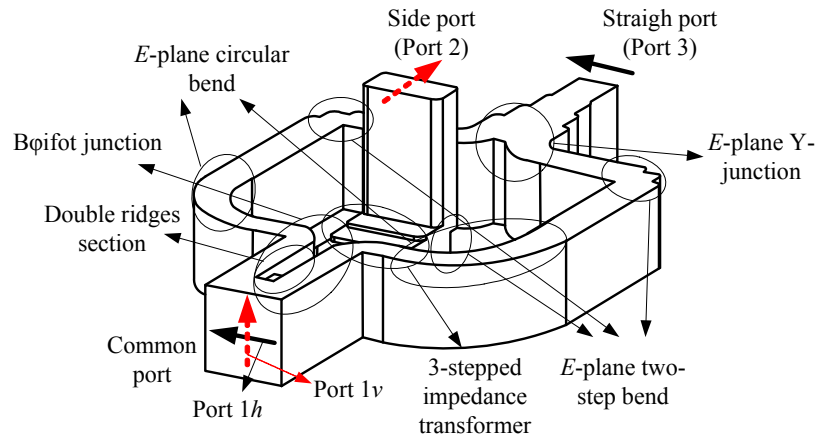
The horizontally-polarized wave is coupled to two symmetric apertures in the side walls of the square waveguide. Multiple thin metallic pins are installed in the aperture to improve the impedance matching. Each side wall slot is connected to a corresponding rectangular waveguide, which is then bent to form a leg of the  $Y$ -junction power combiner. The  $E$ -plane dimension of the waveguide is reduced prior to power combining. A  $Y$ -junction power combiner finally sums up the power in the two side-arm waveguides and outputs it to port 3.

The original Bøifot OMT structure can be modified in many ways, which include the use of double ridges as shown in Fig. 2.11(b) [16]-[19]. The tapering of the ridge can be either in one direction [11], [13]-[16] or in two directions [12]. In conjunction with double ridges, side-wall slots with matching posts may be replaced two symmetric branch waveguides that couple the horizontally-polarized wave as shown in Fig. 2.11(a). For size reduction and performance improvement, the circular bend in the side-arm waveguide can be replaced with an  $E$ -plane circular and two-step bends as shown in Fig. 2.11(a). In this dissertation, a detailed investigation on the design of the double-ridged OMT structure shown in Fig. 2.11 is carried out. Fig. 2.11(b) shows the internal structure of the polarization-separating junction.

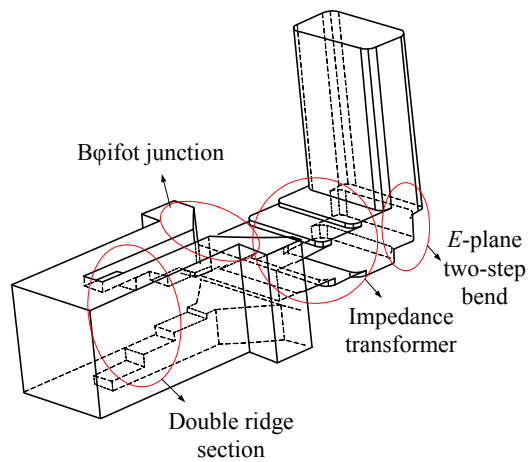
The vertically-polarized wave ( $1v$ ) in the common waveguide is coupled to the port 2 via double ridges, a stepped-impedance transformer and a stepped  $E$ -plane bend. The starting width and height of the ridge is one fourth and one tenth of the square waveguide width. The spacing between double ridges is reduced to two fifths of the square waveguide height in three steps. The width of the last ridge is linearly increased to be same as the width of the waveguide of port 2. The  $E$ -plane height of this waveguide is increased into the output waveguide using a two-step impedance matching section, while the width of this waveguide remains unchanged. The  $E$ -plane two-step bend is used to change the direction of this waveguide forming port 2. The waveguide of port 2 has rounded corners which make split-block fabrication possible.

The horizontally-polarized wave ( $1h$ ) is symmetrically coupled to two side-wall waveguides in the polarization-separating junction. The side-wall waveguide is connected

to the square waveguide via the 45-degree linearly-mitered bend formed by double ridges. In another point of view, double ridges form two symmetric side wall waveguides with a 45-degree linearly-mitered bend.



(a)



(b)

Fig. 2.11 Structure of a Bøifot OMT with double ridges. (a) External and (b) internal views of the polarization-separating junction.

The direction of the side-wall waveguide is changed by 90 degrees with a circular bend, where the  $E$ -plane dimension is also properly increased prior to power combining in the  $Y$  junction. An  $E$ -plane two-step bend is used to change the direction of this waveguide. A  $Y$ -junction power combiner is used in combining two side-wall waveguides into the straight port. A three-step impedance matching section is employed at the  $Y$ -junction for interfacing with the standard rectangular waveguide of the straight port.

To better understand the operating principle of the Bøifot OMT with double ridges, internal electric fields of the OMT are calculated with Microwave Studio<sup>TM</sup>. Fig. 2.12(a) shows the magnitude of the electric field inside the OMT when the common port is excited with a vertically-polarized wave ( $1v$ ). Almost all of the common port power is delivered to the side port, while negligible power comes out of the straight port. Fig. 2.12(b) depicts the operation of the OMT with the common port excited with a horizontally-polarized wave ( $1h$ ). The horizontally-polarized wave is dominantly coupled to the straight port.

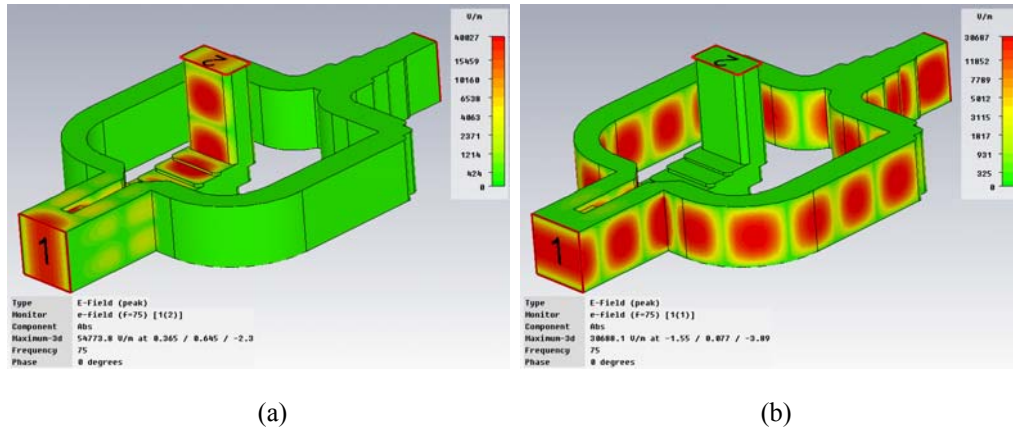


Fig. 2.12 Magnitude of internal electric fields of the Bøifot OMT with double ridges when the common port is excited with (a) vertically- and (b) horizontally-polarized waves.

Fig. 2.13(a) shows the side view of a 2D arrow plot of the internal electric fields when the common port is excited with a vertically-polarized wave ( $1v$ ). Fig. 2.13(b) is the top view when the horizontally-polarized wave ( $1h$ ) is incident on the common port. Fig. 2.15 shows electric fields at various cross sections of the Bøifot OMT with double ridges.

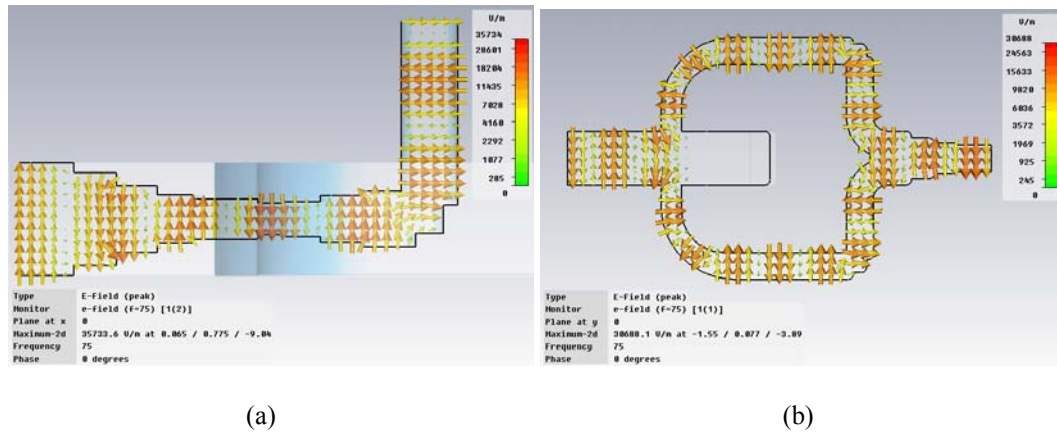


Fig. 2.13 Arrow plots of internal electric fields of the Bøifot OMT with double ridges when the common port is excited with (a) vertically and (b) horizontally-polarized waves.

Fig. 2.14 shows the designation of various cross sections of the OMT. Plots on the left and right columns of Fig. 2.15 correspond to the case when the common port is excited with vertically- and horizontally-polarized waves, respectively.

Looking at left plots of Figs. 2.15(a) to (k), one can easily see than the vertically-polarized wave ( $1v$ ) is transmitted well to the side port (port 2) while it is not transmitted well to the straight port (port 3). The maximum electric fields at the side port (the left plot of Fig. 2.5(h)) and straight port (the left plot of Fig. 2.5(k)) are 14,460 V/m and 1.86 V/m respectively when one watt of the vertically-polarized wave is incident on the common

port. The polarization discrimination in this case can be calculated as

$$-20\log_{10} |S_{1v,3}| = -10\log_{10} \frac{P_3}{P_{1v}} \frac{P_{1v}}{P_2} = -10\log_{10} \frac{P_3}{P_2} = -20\log_{10} \frac{E_3}{E_2} = -20\log_{10} \frac{1.86}{14460} = 77.8\text{dB}.$$

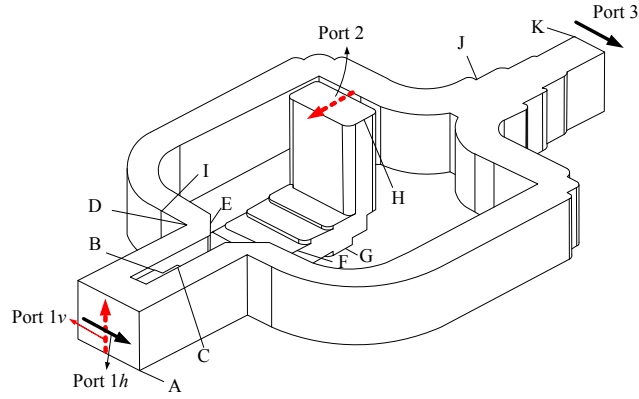
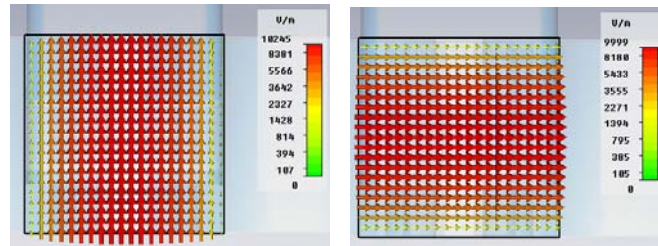
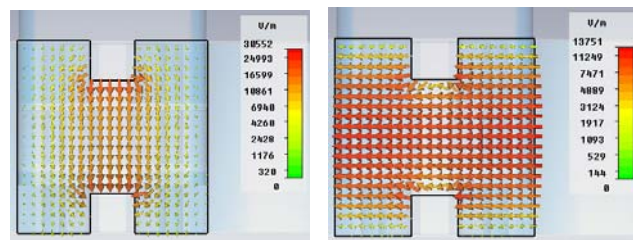


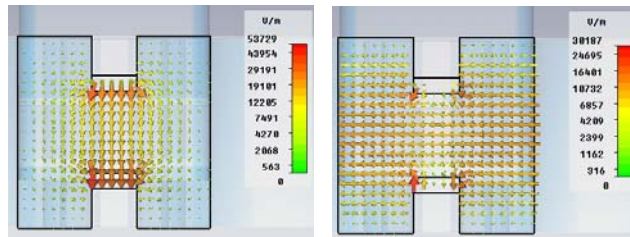
Fig. 2.14 Designation of cross sections of the Bøifot OMT with double ridges.



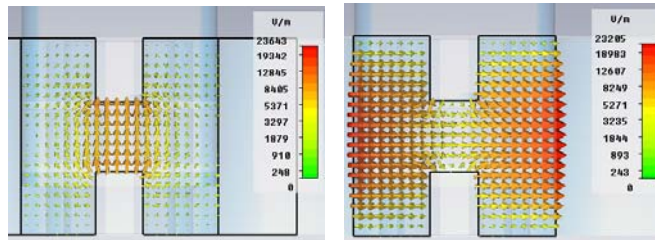
(a) Electric field cross section A



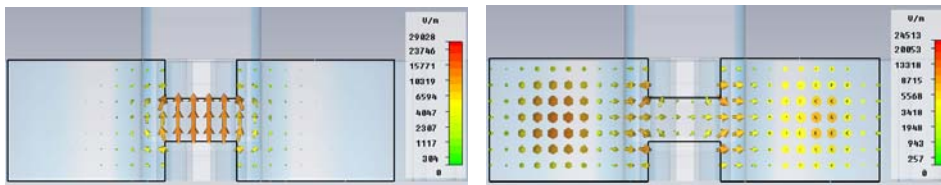
(b) Electric field cross section B



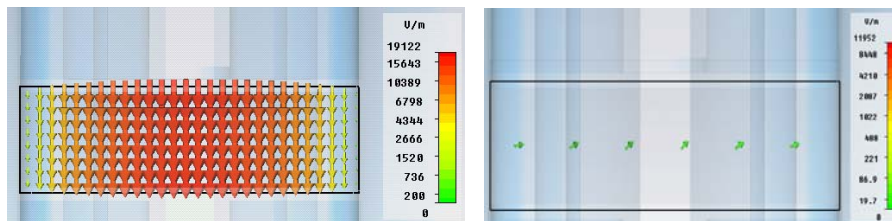
(c) Electric field cross section C



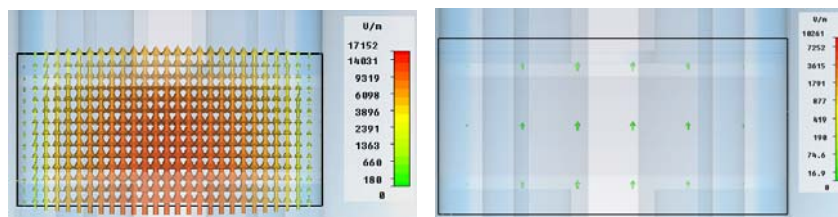
(d) Electric field cross section D



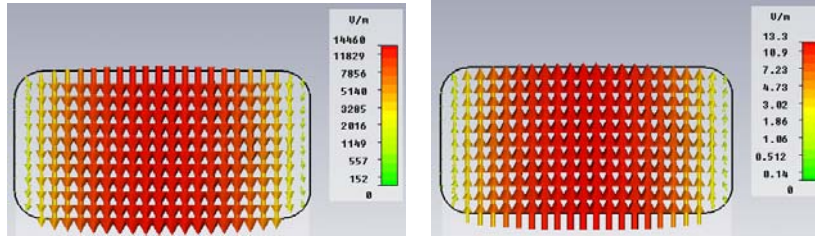
(e) Electric field cross section E



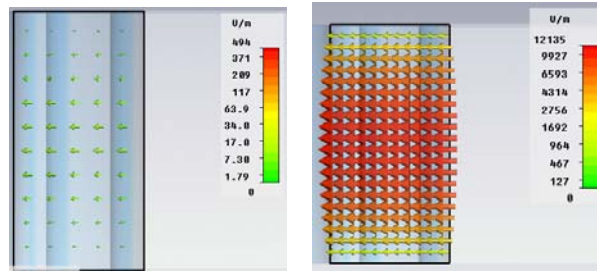
(f) Electric field cross section F



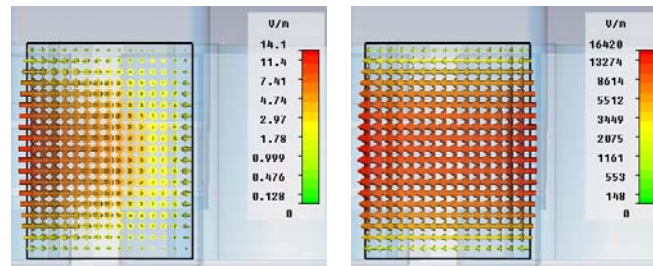
(g) Electric field cross section G



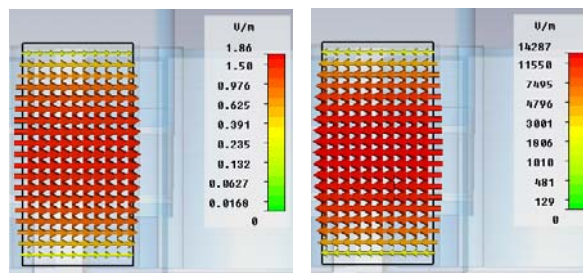
(h) Electric field cross section H



(i) Electric field cross section I



(j) Electric field cross section J



(k) Electric field cross section K

Fig. 2.15 Internal electric fields of Bøfot OMT with double ridges at various cross sections.

A similar observation can be made in case of the common port excited with a horizontally-polarized wave. The maximum electric fields at the side port (the right plot of Fig. 2.5(h)) and straight port (the right plot of Fig. 2.5(k)) are 13.3 V/m and 14,287 V/m respectively when one watt of the horizontally-polarized wave is incident on the common port. The polarization discrimination in this case can be calculated as

$$-20\log_{10} |S_{1h,2}| = -10\log_{10} \frac{P_2}{P_{1v}} \frac{P_{1v}}{P_3} = -10\log_{10} \frac{P_2}{P_3} = -20\log_{10} \frac{E_2}{E_3} = -20\log_{10} \frac{13.3}{14287} = 60.6\text{dB}.$$

Table 2.5 shows the design goals of the Bøifot OMT with double ridges which include the reflection coefficient, transmission coefficient, port isolation, polarization discrimination and operating bandwidth.

Table 2.5 Design goals of the Bøifot OMT with double ridges

Performance	Design goal
Reflection ( $R$ )	$\leq -20\text{dB}$
Transmission ( $T$ )	$\geq -0.5\text{dB}$
Isolation ( $I$ )	$\geq 30\text{dB}$
Discrimination ( $D$ )	$\geq 30\text{dB}$
Bandwidth ( $B$ )	60-90GHz

The design of the Bøifot OMT with double ridges is done in following steps. The desired frequency bend for this OMT is 60-90GHz, which is the full frequency band of WR-12 waveguide.

- 1) Building blocks of the OMT (stepped  $E$ -plane bend, polarization-separating junction, circular  $E$ -plane bend, and  $Y$ -junction power combiner) are designed separately.

- 2) The whole OMT structure is constructed by assembling building blocks that have already been designed.
- 3) The performance of the whole OMT structure is simulated. If the OMT does not meet design goals, the structure is optimized by changing critical parameters.

Building blocks and dimensional parameters of the Bøifot OMT with double ridges are shown in Fig. 2.16.

Many researchers have investigated *E*-plane bends in rectangular waveguide which include chamfer, stepped, rounded, and circular types [37], [40]-[46]. Important aspects in the design of the bend are wide bandwidth and low reflection coefficient. In reference [43] many types of *E*-plane bends are investigated and their performances are compared. Furthermore, an optimum design for each type is presented. Initial dimensions of the stepped *E*-plane bend are obtained by referring to [43]-[44]. Then the optimization utility in Microwave Studio<sup>TM</sup> is employed to arrive at an optimum design:  $a = 2b = 3.05\text{mm}$  (WR-12),  $a_8 = 0.505b = 0.77\text{mm}$ , and  $a_9 = 0.256b = 0.39\text{mm}$ . For compatibility with split-block fabrication, every square corner is modified to a circular corner of 0.30-mm radius.

The simulated reflection coefficient of the designed bend is shown in Fig. 2.17. The bend has a reflection coefficient of less than -45dB and a transmission coefficient of greater than -0.05dB at 60-90GHz.

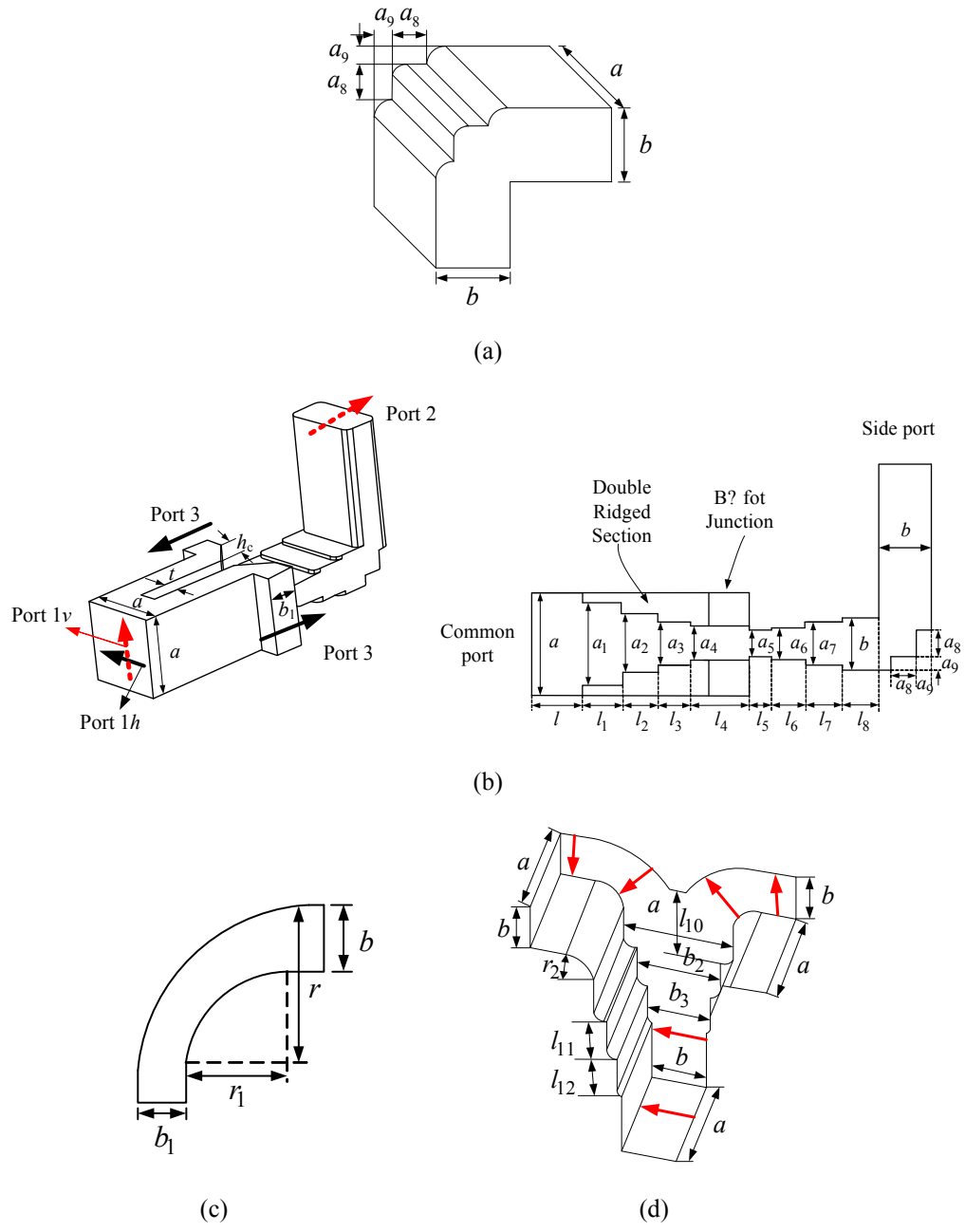


Fig. 2.16 Building blocks and dimensional parameters of the Bøifot OMT with double ridges. (a) Stepped *E*-plane bend, (b) polarization-separating junction, (c) circular *E*-plane bend, and (d) *Y*-junction power combiner.

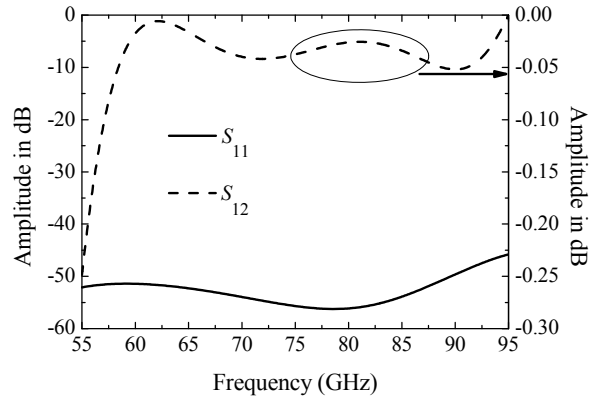


Fig. 2.17 Simulated reflection coefficient of the stepped  $E$ -plane bend in a rectangular waveguide.

Initial dimensions of the polarization-separating junction are determined using simple waveguide theory in a way similar to the case of the Dunning OMT. Initial lengths of all waveguide sections in Fig. 2.16(b) are one quarter of a guided wavelength ( $\lambda_g/4$ ) at 75GHz. The guided wavelength at the center frequency (75GHz) of the  $TE_{10}$  mode in WR-12 waveguide is 5.30mm. The parameter  $a_4$  is set to be equal to  $2a/5$  (1.24mm). Formulas in Table 2.6 are also used in finding initial dimensions.

Table 2.6 Formulas for initial dimensions of the polarization-separating junction of the Bøifot

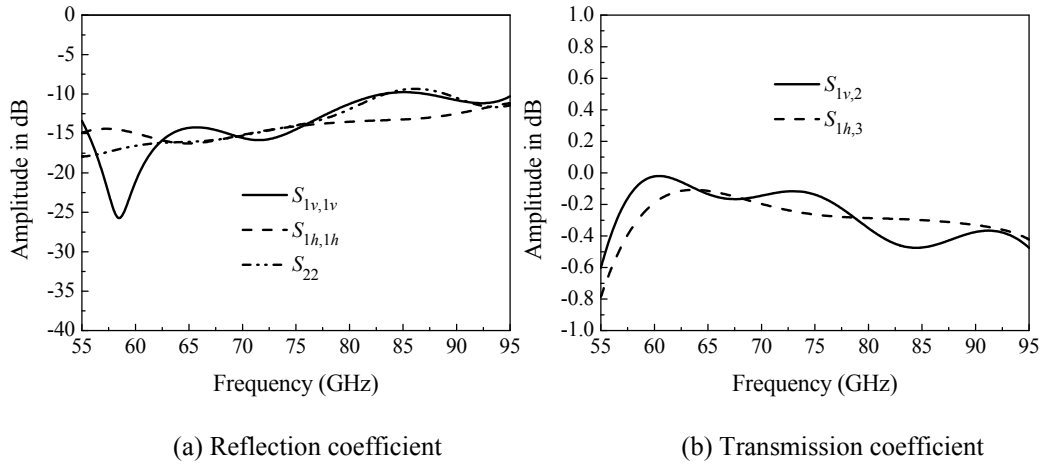
OMT with double ridges.

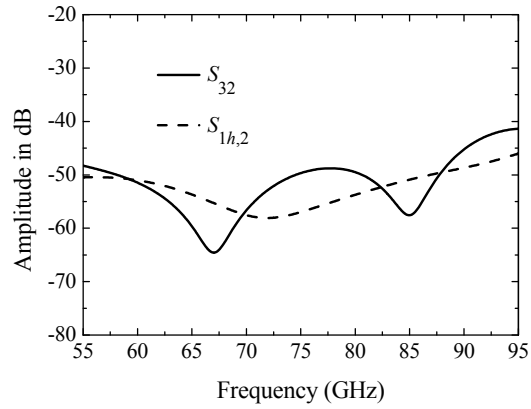
Parameter	Formula
$t$	$a/4$
$a_1$	$a-(a-a_4)/4$
$a_2$	$a_1-(a-a_4)/4$
$a_3$	$a_2-(a-a_4)/4$
$a_5$	$a_4$
$a_6$	$a_5+(b-a_5)/3$
$a_7$	$a_6+(b-a_5)/3$
$b_1$	$b$
$h_c$	$3b_1/4$

Table 2.7 Initial dimensions of the polarization-separating junction of the Bøifot OMT with double ridges (unit in mm).

$a$	$a_1$	$a_2$	$a_3$	$a_4$	$a_5$	$a_6$	$a_7$	$a_8$	$a_9$	$b$	$b_1$	$t$
3.1	2.64	2.17	1.7	1.24	1.24	1.34	1.45	0.77	0.39	1.55	1.55	0.73
$l$	$l_1$	$l_2$	$l_3$	$l_4$	$l_5$	$l_6$	$l_7$	$l_8$	$t$	$h_c$		
1.3	1.3	1.3	1.3	1.3	1.3	1.3	1.3	1.3	0.78	1.16		

Pre-designed two-step impedance transformer and two-step  $E$ -plane bend are added and the whole structure is simulated using Microwave Studio<sup>TM</sup>. The performance of the polarization-separating with initial dimensions is shown in Fig. 2.18. The reflection coefficients at the common and output ports are not less than -20dB at the desired frequency band (60-90GHz).





(c) Polarization discrimination and port isolation

Fig. 2.18 Performance of the polarization-separating junction with initial dimensions of the Bøifot OMT with double ridges.

Using the parameter sweep function of Microwave Studio<sup>TM</sup>, dimensions of the polarization-separating junction are optimized. The performance of the optimized polarization-separating junction is shown in Fig. 2.19. Over 59.46-92.56GHz (43.54% bandwidth), the reflection coefficient is less than -20dB, the port isolation is greater than 80dB and the amplitude balance is within the  $\pm 0.5$ dB. Values of optimum dimensions will be shown in Table 2.8.

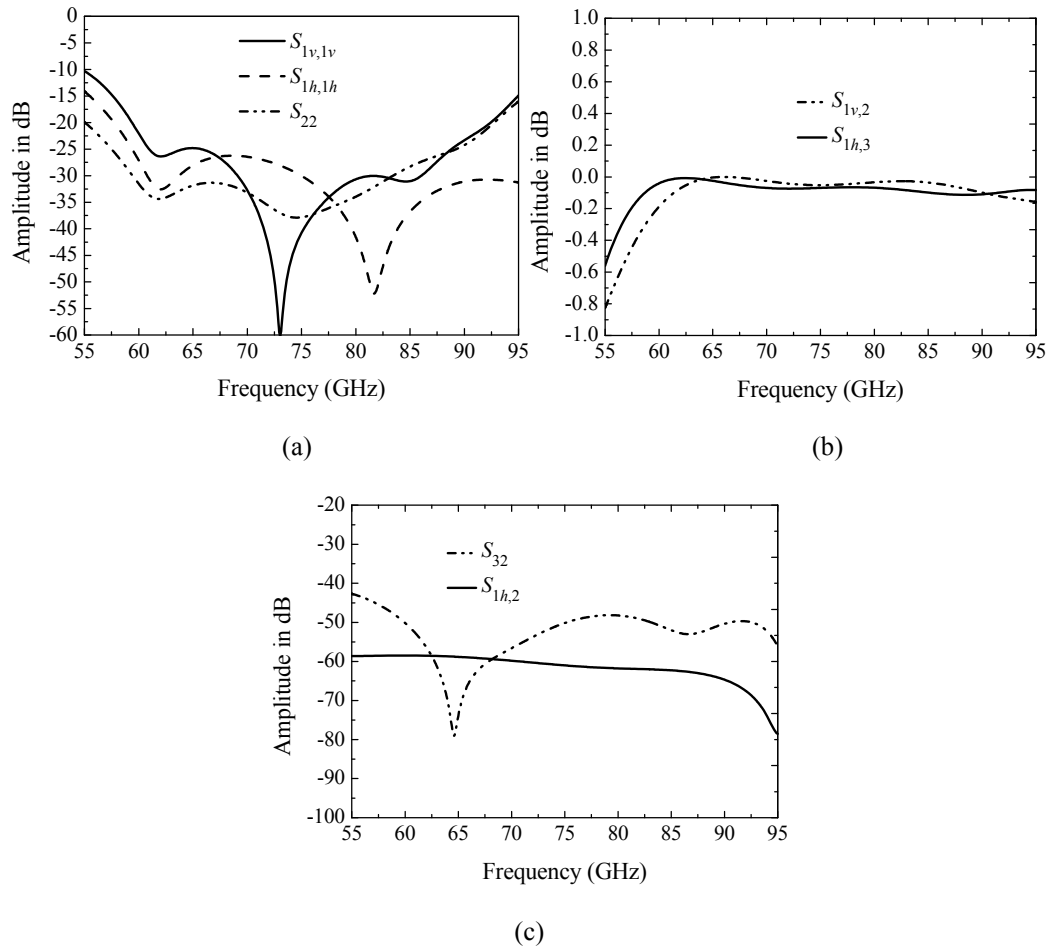


Fig. 2.19 Performance of the optimized polarization-separating junction of the Bøifot OMT with double ridges. (a) Reflection coefficient, (b) transmission coefficient and (c) polarization discrimination and port isolation.

Next, a circular  $E$ -plane bend is designed. The starting  $E$ -plane dimension of the bend matches that of the side-wall waveguide of the polarization-separating junction. The  $E$ -plane dimension is linearly increased in the circular bending region to that of a standard

rectangular waveguide WR-12. Many researchers have investigated this type of bend [47]-[48]. The size of the OMT is significantly reduced by the use of this bend.

Optimized dimensions of the circular bend are  $r=4.25\text{mm}$  and  $r_1=2.46\text{mm}$ . Fig. 2.23 shows the performance of the designed circular  $E$ -plane bend. The bend has a reflection coefficient of less than  $-25\text{dB}$  and transmission coefficient of greater than  $-0.1\text{dB}$  at 60-95GHz.

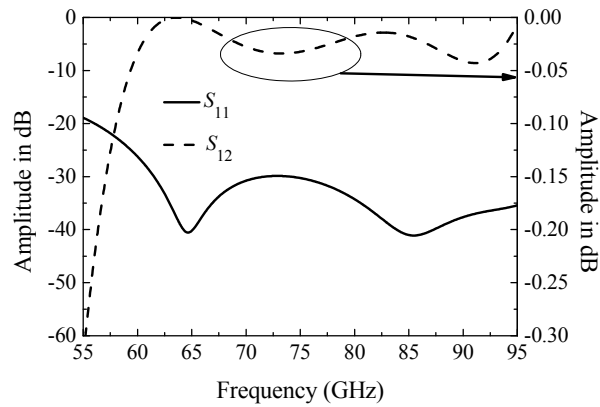


Fig. 2.20 Performance of the circular  $E$ -plane bend.

Next, an  $E$ -plane  $Y$ -junction waveguide power combiner is designed. It has been investigated by many researchers [18]-[19], [39]-[40], [45]-[46]. At the output arm of the combiner, there is a three-step  $E$ -plane impedance transformer for transition from a square waveguide to a standard rectangular waveguide WR-12. At input arms of the combiner, there is a circular bend. It is usually called by “antiphase power combiner or divider”. Output and input ports are in the standard rectangular waveguide WR-12. For initial dimensions, step sizes of the impedance matching section are made same and

lengths of each step section one quarter of a guided wavelength. Starting from initial dimensions, the *Y*-junction combiner is optimized to obtain final dimensions:  $a=3.1\text{mm}$ ,  $b=1.55\text{mm}$ ,  $b_2=2.36\text{mm}$ ,  $b_3=1.78\text{mm}$ ,  $l_{10}=2.38\text{mm}$ ,  $l_{11}=1.32\text{mm}$ ,  $l_{12}=1.31\text{mm}$ ,  $r_2=0.8\text{mm}$ . Fig. 2.21 shows the performance of the designed *Y*-junction power combiner. Over 59.36-92.77GHz (43.92% bandwidth), the reflection coefficient is less than -30dB and amplitude balance is within  $\pm 0.2\text{dB}$ . The phase is exactly balanced because of the symmetric in the structure.

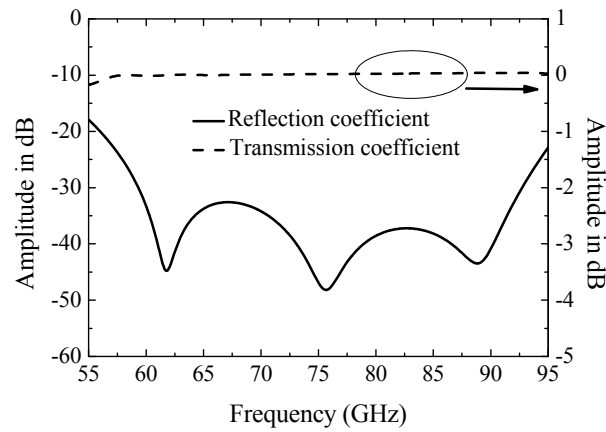


Fig. 2.21 Performance of the designed *E*-plane *Y*-junction combiner.

The Bøifot OMT with double ridges is now realized by assembling all the sub-structures designed in the above. Fig. 2.22 shows dimensional symbols of the OMT. After the assembly, the whole structure is optimized using the parameter sweep function of Microwave Studio<sup>TM</sup>. In the optimization, the main consideration is the dimension of the polarization-separating junction.

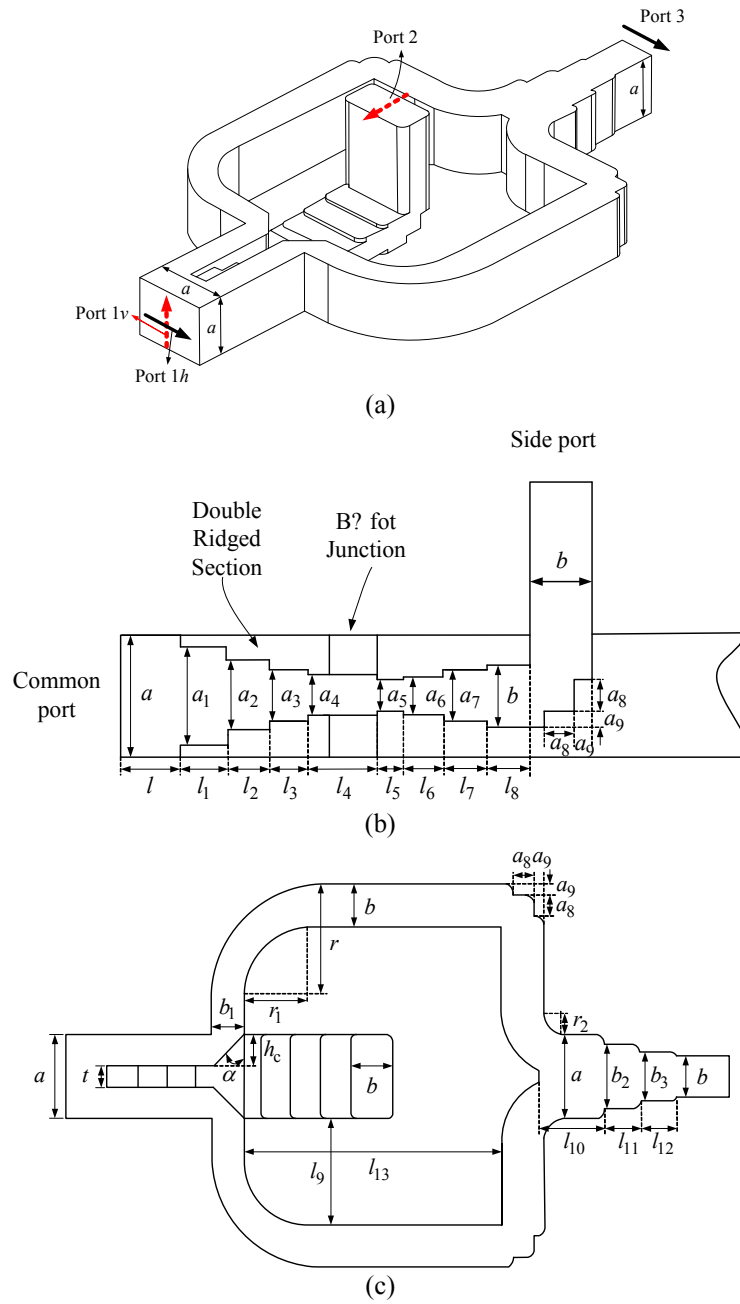


Fig. 2.22 Dimensions of the Bøifot OMT with double ridges. (a) 3D view, (b) side views and (c) top view.

Table 2.8 shows the final dimensions of the designed Bøifot OMT with double ridges. The optimized performance of this OMT is shown in Fig. 2.23. Over 59.67-91.4GHz (42% bandwidth), the reflection coefficient is less than -20dB, the port isolation is greater than 45dB, the polarization discrimination is greater than 55dB and the transmission coefficient is greater than -0.2dB.

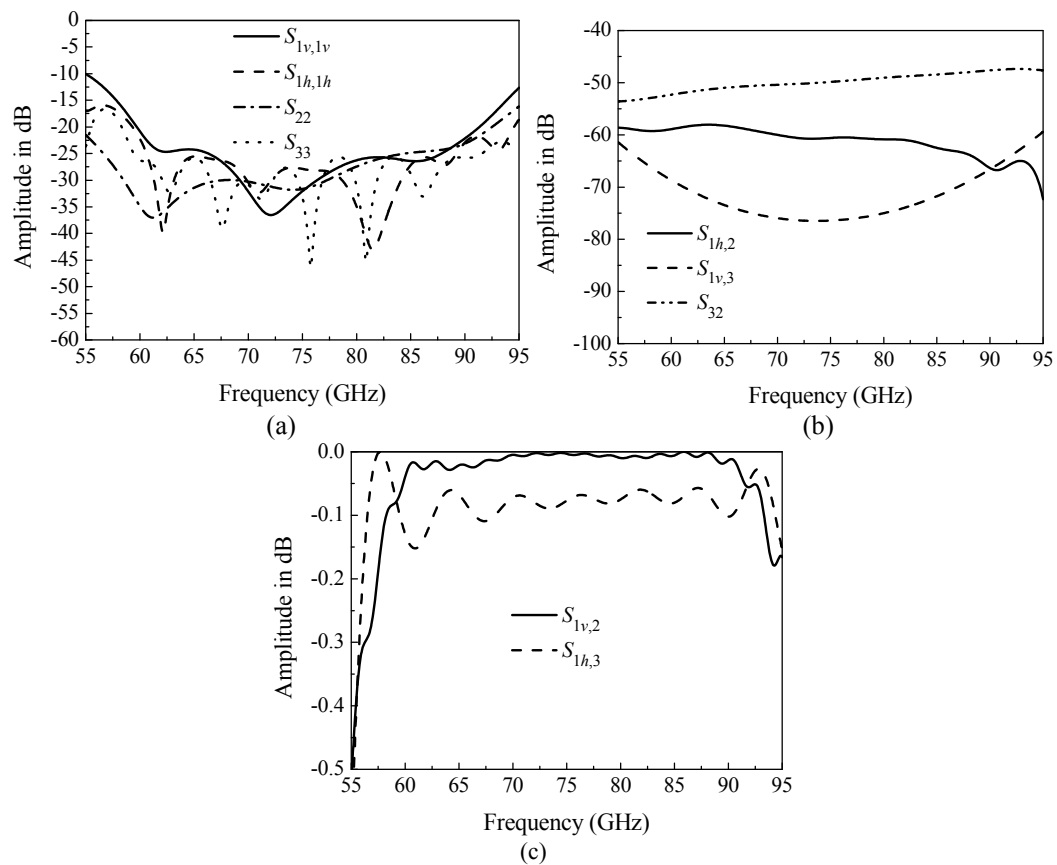


Fig. 2.23 Performance of the designed Bøifot OMT with double ridges.

(a) Reflection coefficient, (b) port isolation and polarization discrimination, and (c) transmission coefficient.

Table 2.8. Final dimensions of the designed Bøifot OMT with double ridges in mm.

$a$	$a_1$	$a_2$	$a_3$	$a_4$	$a_5$	$a_6$	$a_7$	$a_8$	$a_9$	$b$	$b_1$	$b_2$	$b_3$	$t$
3.1	2.55	1.83	1.32	1.1	0.87	0.97	1.29	0.77	0.39	1.55	1.18	2.36	1.8	0.73
$l$	$l_1$	$l_2$	$l_3$	$l_4$	$l_5$	$l_6$	$l_7$	$l_8$	$l_9$	$l_{10}$	$l_{11}$	$l_{12}$	$l_{13}$	$\alpha$
1.5	1.18	1.12	1	1.77	0.65	1.08	1.12	1.12	3.93	2.38	1.32	1.31	9.53	45°
$h_c$	$r$	$r_1$	$r_2$											
1.11	4.25	2.46	0.84											

Fig. 2.24 shows the effect of double ridges on the polarization-separating junction. The impedance of vertical polarization is matched by the double-ridged section of the Bøifot junction. The critical part for the horizontal polarization is a chamfer on the side arms of the Bøifot junction.

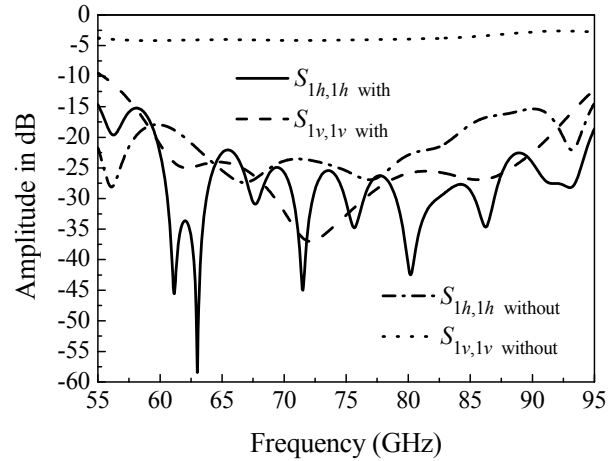
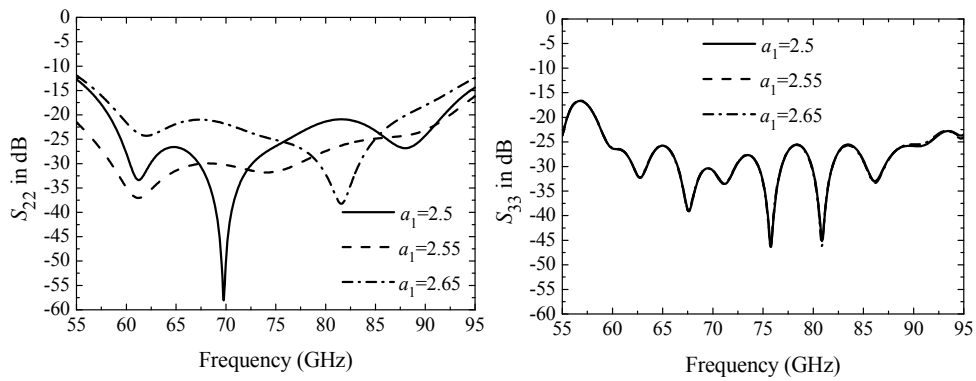


Fig. 2.24 Effect of the double ridges on the impedance matching of the vertically-polarized wave in the Bøifot OMT with double ridges.

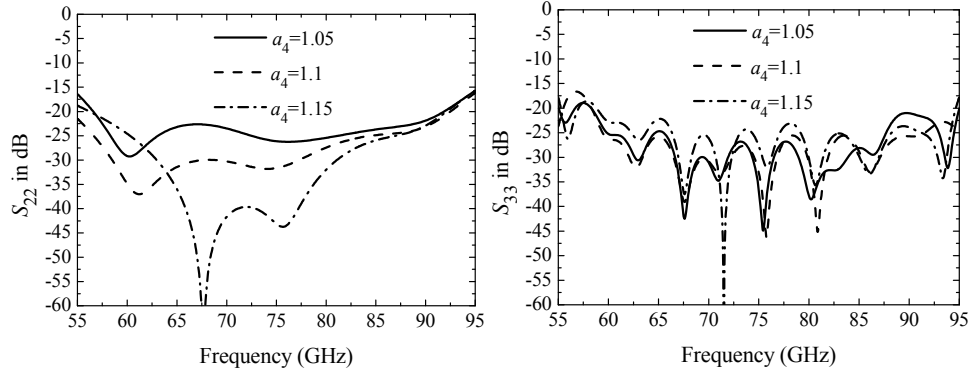
Fig. 2.25 shows reflection coefficients versus dimensional parameters of the Bøifot OMT with double ridges. In order to reach an optimum design, one initially has to

perform parametric studies and find a set of important parameters. Then the parameter sweep is carried only for those important parameters.

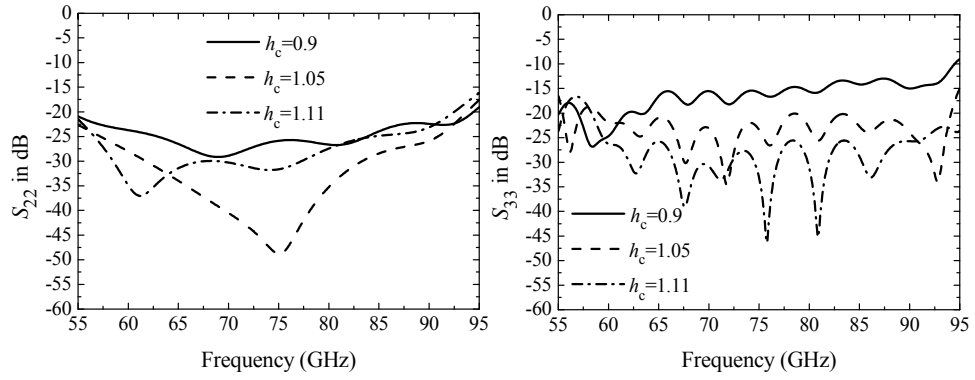
First, the effect of the dimensions  $a_1$  and  $a_4$  of the double-ridged section is plotted in Fig. 2.25(a) and (b). They have a significant effect on the level of the reflection coefficient of port 2 ( $S_{22}$ ), but they have no effect on the reflection coefficient of port 3 ( $S_{33}$ ). The effect of the chamfer's  $h_c$  is plotted in Fig. 2.25(c). It has a significant effect on the level of the reflection coefficients of ports 2 and 3. If the dimension  $a_5$  of the three-step impedance matching section is increased, the level of the reflection coefficient of port ( $S_{22}$ ) is greatly increased as shown in Fig. 2.25(d). The dimension  $b_1$  has little effect on the level of the reflection coefficient of port 3 ( $S_{33}$ ).



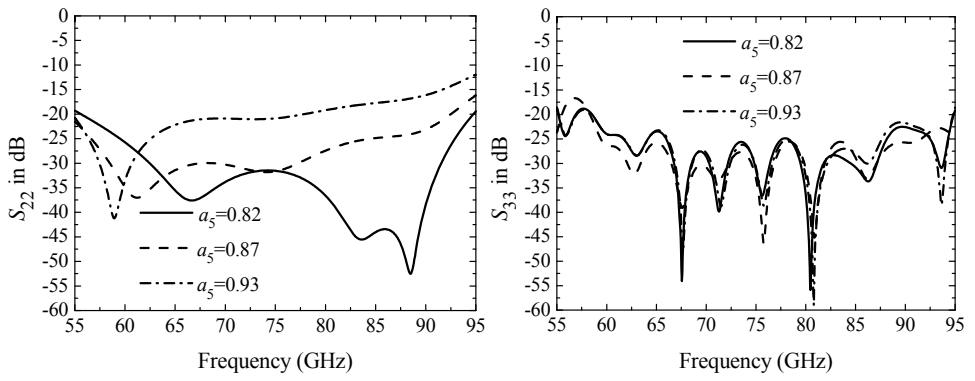
(a) Effect of  $a_1$ .



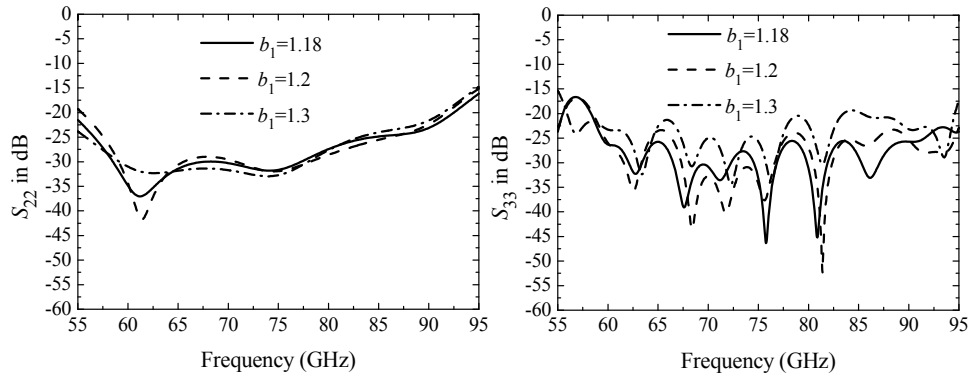
(b) Effect of  $a_4$ .



(c) Effect of  $h_c$ .



(d) Effect of  $a_5$ .



(e) Effect of  $b_1$ .

Fig. 2.25 Effects of dimensional parameters on the performance of the Bøifot OMT with double ridges.

## 2.4 Branch-Line OMT

The branch-line OMT is based on the backward coupling section of either asymmetric [17] or symmetric [18]-[19] type. A branch-line OMT with asymmetric backward coupling sections consists of two  $E$ -plane couplers, stepped  $E$ -plane bends, stepped impedance transformers, a circular-to-square waveguide transition and  $45^\circ$  rectangular waveguide twists with stepped-impedance matching section in output ports. A branch-line OMT with symmetric backward coupling sections consists of symmetric coupling sections, reactive loads,  $E$ -plane bends and an  $E$ -plane  $Y$ -junction power combiner.

Fig. 2.26 shows an OMT with symmetric branch-line backward coupling sections investigated in this dissertation. The backward coupling section plays an important role in the polarization-separating junction. In Fig. 2.26, it efficiently couples the horizontally-polarized wave while negligibly disturbs the propagation of the vertically-polarized wave

in the polarization-separating junction. The backward coupling section consists of four branch lines and a three-step reactive load.

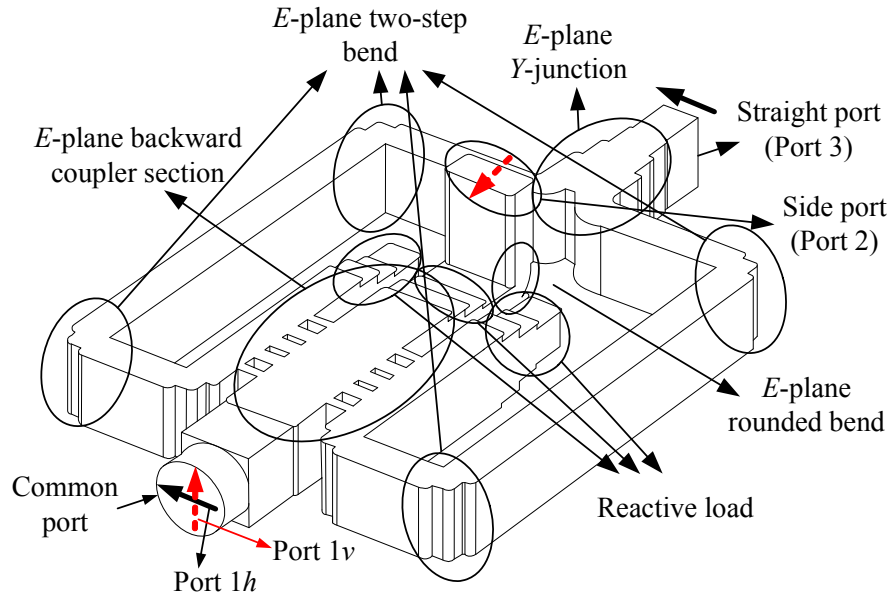


Fig. 2.26 Structure of the branch-line OMT.

In the original branch-line OMT, the common waveguide is of square shape and stepped-impedance transformers are employed for each output port. In this dissertation, a square-to-circular waveguide transition is added to obtain a circular common port. For wide band operation, a coupler with five branch lines is employed. A standard rectangular waveguide is used in polarization-separating junction.

In the common waveguide, a circular-to-square waveguide transition and one-step square waveguide impedance transformer are employed. The horizontally-polarized wave (port  $1h$  in Fig. 2.26) is divided into two waves of equal amplitude and anti-phase by two

symmetric backward couplers. The reactive load is used to terminate the unused port of the coupler. A two-step *E*-plane bend is used to change the direction of two output waveguides of couplers, which are then combined in an *E*-plane *Y*-junction. The *Y*-junction power combiner is of the same type as in the Boifot OMT with double ridges.

For the vertically-polarized wave (port 1<sub>v</sub> in Fig. 2.26), the height of the square waveguide in the polarization-separating junction is reduced three steps so that the horizontally-polarized wave is cut off and the vertically-polarized one is transmitted to port 2, where a rounded *E*-plane bend is used to change the direction of the waveguide.

The operating principles of the branch-line coupler are crucial to the understanding of the branch-line OMT. Fig. 2.27 shows the structure and schematic of a branch-line coupler.

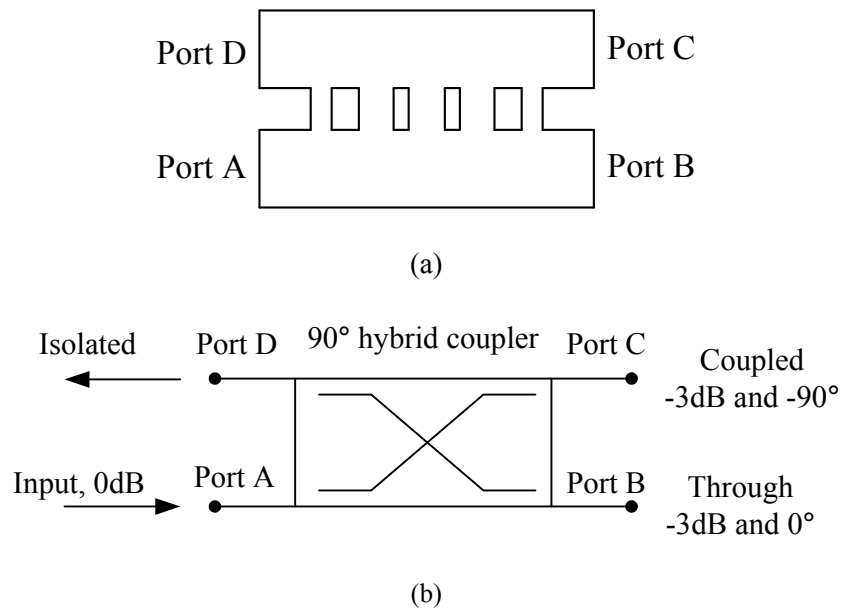


Fig. 2.27 (a) Structure and (b) schematic representation of a branch-line coupler.

The input signal at port A is equally divided into ports B and C (-3 dB transmission) with  $90^\circ$  phase difference. The port D is isolated from port A. The branch-line coupler consists of three or more branch lines where the distance between branch lines is around one quarter of a guided wavelength. When a hybrid coupler consists of two branch lines, the distance between branch lines is around  $3\lambda_g/4$  because the width of the branch line is greater than one quarter of a guided wavelength. If the number of branch lines is increased, the bandwidth is increase [49]-[56]. References [55]-[56] investigated and derived the formula for dimensions of a branch-line coupler with arbitrary number of branch lines.

When a reactive load (RL) terminates ports B and C, signals are totally reflected from the reactive load and sent backward and recombined in phase at port D and out of phase (with  $180^\circ$  phase difference) at port A as shown in Fig. 2.28. So, the signal of port A is transmitted to port D without loss. It is important that reactive loads terminating ports B and C have the same reactance.

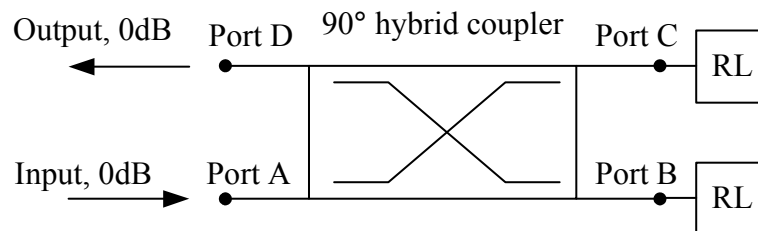
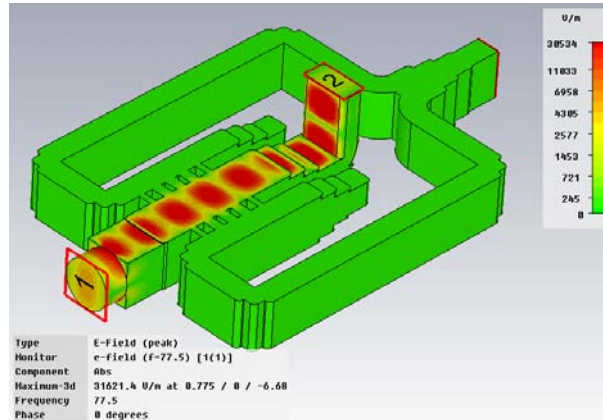


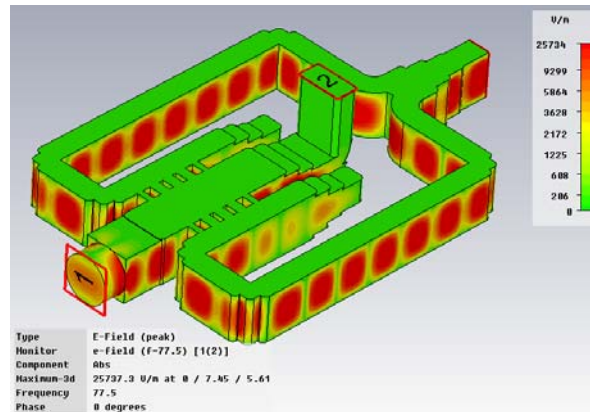
Fig. 2.28 Schematic representation of a backward coupling structure with reactive loads.

To better understand the operating principles of the branch-line OMT, the Microwave Studio<sup>TM</sup> is used to obtain field distributions inside this OMT. Fig. 2.29(a) is the case of

the common port excited with a vertically-polarized wave. Almost all of the common port power is delivered to the side port, while negligible power comes out of the straight port. A similar observation can be made for the case where the common port is excited with a horizontally-polarized wave shown in Fig. 2.29(b).



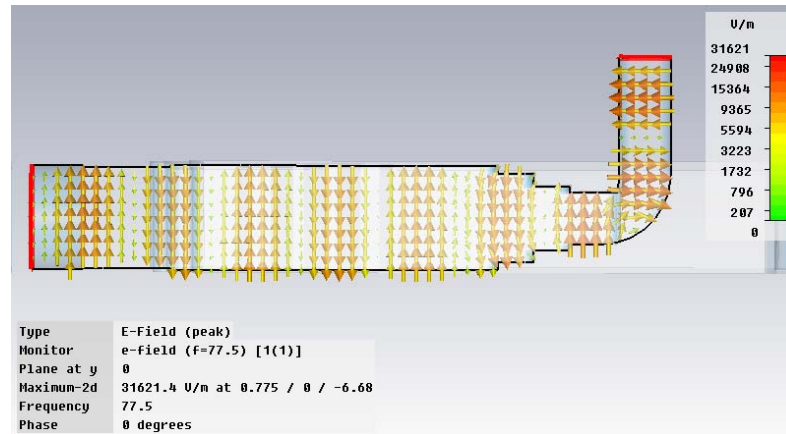
(a)



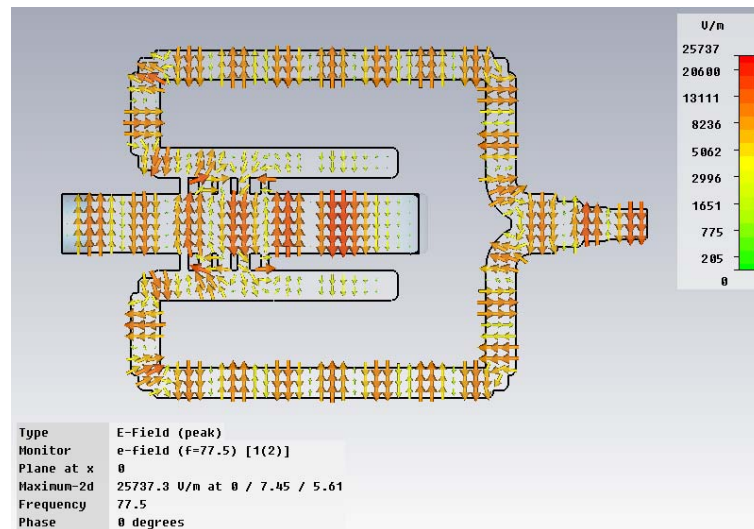
(b)

Fig. 2.29 Magnitude of internal electric fields of the branch-line OMT when the common port is excited with (a) vertically- and (b) horizontally-polarized waves.

Fig. 2.30(a) shows the side view of a 2D arrow plot of the internal electric field when the common port is excited with a vertically-polarized wave (port 1v). Fig. 2.30(b) is the top view when the horizontally-polarized wave (port 1h) is incident on the common port.



(a)



(b)

Fig. 2.30 Arrow plots of internal electric fields of the branch-line OMT when the common port is excited with (a) vertically and (b) horizontally-polarized waves.

Table 2.9 shows the design goals of the branch-line OMT which include the reflection coefficient, transmission coefficient, port isolation, polarization discrimination and operating bandwidth.

Table 2.9 Design goals of the branch-line OMT

Performance	Design goal
Reflection ( $R$ )	$\leq -20\text{dB}$
Transmission ( $T$ )	$\geq -0.5\text{dB}$
Isolation ( $I$ )	$\geq 30\text{dB}$
Discrimination ( $D$ )	$\geq 30\text{dB}$
Bandwidth ( $B$ )	70-87GHz

The design of the branch-line OMT is done in following steps. The desired frequency band for this OMT is 70-87GHz. First, the 90-degree hybrid coupler with five branch lines is designed. Its structure is shown in Fig. 2.31. Next, three-step reactive loads are applied to the designed hybrid coupler as shown in Fig. 2.32. Then, the symmetric backward coupling section is realized as shown in Fig. 2.33. Next,  $E$ -plane bends, and an  $E$ -plane  $Y$ -junction power combiner are designed. In the final step, the whole structure of the branch-line OMT is realized by assembling sub-structures that are already designed.

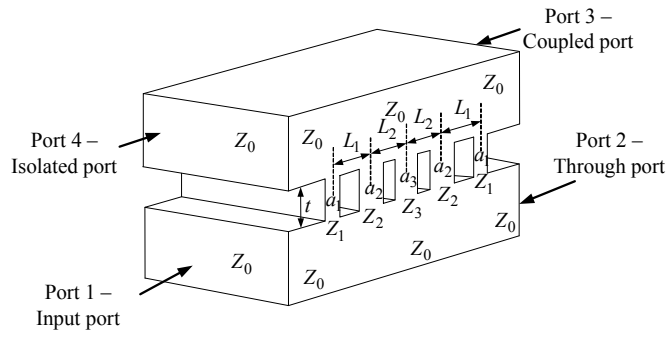


Fig. 2.31 Structure of a 90-degree coupler with five branch lines.

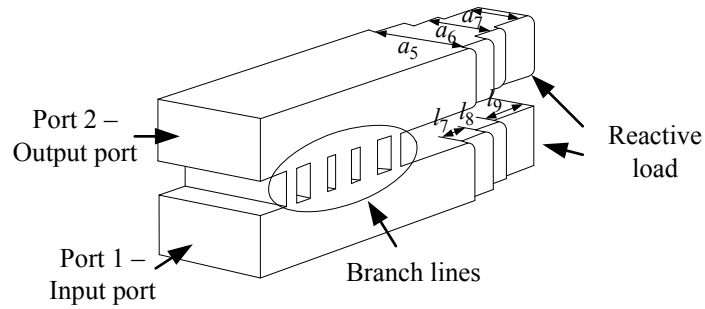


Fig. 2.32 Structure of a branch-line coupler with reactive loads.

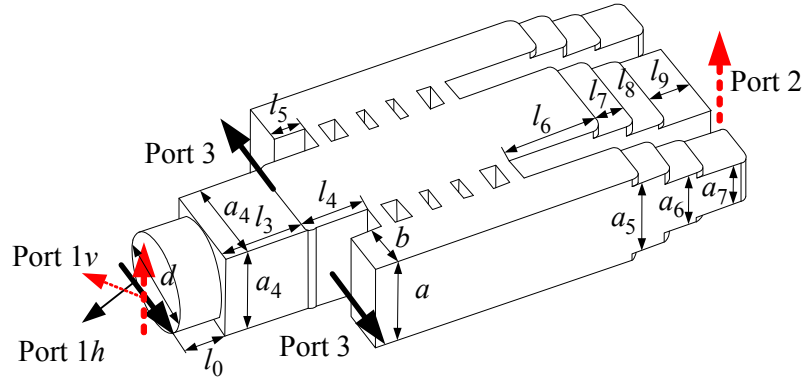


Fig. 2.33 Structure of the polarization-separating junction in the branch-line OMT.

The initial dimensions of the  $E$ -plane coupler with five branch lines are calculated by formulas in the literature [55]-[56]. Normalized characteristic impedances of branch lines are given by  $Z_0=1$ ,  $Z_1=0.222$ ,  $Z_2=0.326$  and  $Z_3=0.358$ . The power-voltage definition of the characteristic impedance of the equivalent transmission line representing a rectangular waveguide is given by

$$Z_c = \frac{2b}{a} \frac{\eta}{\sqrt{1 - (\lambda_0/\lambda_c)^2}} \quad (2.9)$$

where  $\lambda_c$  cutoff wavelength,  $\eta$  is intrinsic impedance,  $a$  and  $b$  are the waveguide width and height, respectively.

At 75GHz, the guided wavelength of WR-12 waveguide is 4.69mm and the quarter-wavelength is 1.17mm. The calculated impedance of WR-12 is  $Z_c = Z_0 = 490.7\Omega$ , so that is  $Z_1=108.93\Omega$ ,  $Z_2=159.96\Omega$  and  $Z_3=175.67\Omega$ . Next, the  $E$ -plane height of each branch line section is calculated using (2.9):  $a_1=0.34\text{mm}$ ,  $a_2=0.50\text{mm}$  and  $a_3=0.55\text{mm}$ .  $L_1$  and  $L_2$  are around one quarter of a guided wavelength ( $L_1 = L_2 = 1.17\text{mm}$ ) and  $t$  takes an arbitrarily small value ( $t = 0.89\text{mm}$ ).

Fig. 2.34 shows the performance of coupler with five branch lines with initial dimensions. The reflection coefficient, isolation and phase balance are very good but the amplitude balance is greater than 2dB at center frequency. The dimensions of the branch-line coupler are optimized using Microwave Studio<sup>TM</sup>. The  $E$ -plane height of the branch line determines the level of coupling. The distance between adjacent branch lines determines the center frequency. The bandwidth is largely determined by the number of

branch lines. The dimension  $t$  has little effect on the center frequency and on the amplitude balance.

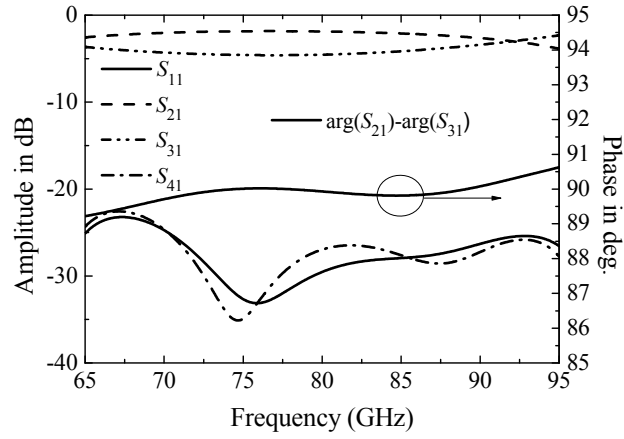


Fig. 2.34 Performance of the branch-line coupler with initial dimensions.

The optimized dimensions of the branch-line coupler are  $a_1 = 0.41\text{mm}$ ,  $a_2 = 0.68\text{mm}$ ,  $a_3 = 0.71\text{mm}$ ,  $t = 0.89\text{mm}$ ,  $L_1 = 1.09\text{mm}$  and  $L_2 = 0.99\text{mm}$ . The  $E$ -plane height of the branch line is slightly increased from the initial value and the distance between adjacent branch lines is slightly decreased for the initial one-quarter of a guided wavelength. Fig. 2.35 shows the performance of the optimized coupler. Over 68-90GHz (27.85%), reflection coefficient and isolation are less than -20dB, amplitude balance is within  $\pm 0.5\text{dB}$  and phase balance within  $+0.03^\circ/-0.3^\circ$ .

Next, a reactive load is connected to the optimized branch-line coupler. In the initial reactive load, step heights are constant and lengths of stepped waveguide sections are around one quarter of a guided wavelength. Initial dimensions of the reactive load are optimized by parameter sweeping with Microwave Studio<sup>TM</sup> to arrive at better

performance. The optimum values are  $a_5 = 2.64\text{mm}$ ,  $a_6 = 1.89\text{mm}$ ,  $a_7 = 1.55\text{mm}$ ,  $l_7 = 1.07\text{mm}$ ,  $l_8 = 1.06\text{mm}$ , and  $l_9 = 1.45\text{mm}$ . Fig. 2.36 shows the performance of the optimized coupler with reactive loads. Over 67.57-93.11GHz (31.78% bandwidth), the reflection coefficient is less than -20dB and transmission coefficient is greater than -0.1dB. When the reactive load is connected to the coupler, the reflection coefficient is decreased.

A polarization-separating junction is realized using the designed branch-line coupler and a circular-to-square waveguide transition. Only the dimensions of the additional parts such as a circular-to-square transition are optimized. The optimum dimensions are  $a = 3.1\text{mm}$ ,  $b = 1.55\text{mm}$ ,  $a_4 = 3\text{mm}$ ,  $a_5 = 2.64\text{mm}$ ,  $a_6 = 1.89\text{mm}$ ,  $a_7 = 1.55\text{mm}$ ,  $d = 3.1\text{mm}$ ,  $l_0 = 1.5\text{mm}$ ,  $l_3 = 2.6\text{mm}$ ,  $l_4 = 2.02\text{mm}$ ,  $l_5 = 1.02\text{mm}$ ,  $l_6 = 3.1\text{mm}$ ,  $l_7 = 1.07\text{mm}$ ,  $l_8 = 1.06\text{mm}$ , and  $l_9 = 1.45\text{mm}$ . Fig. 2.37 shows the performance of the polarization-separating junction. Over 68.25-92GHz (29.64% bandwidth), the reflection coefficient is less than -20dB, the port isolation and polarization discrimination are greater than 160dB and the amplitude balance is within the  $\pm 0.5\text{dB}$ .

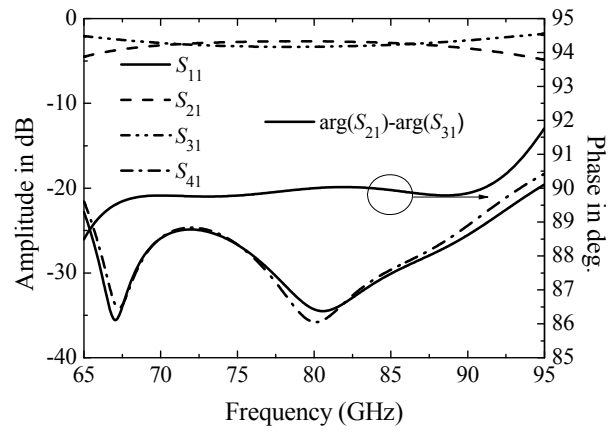


Fig. 2.35 Performance of the optimized branch-line coupler.

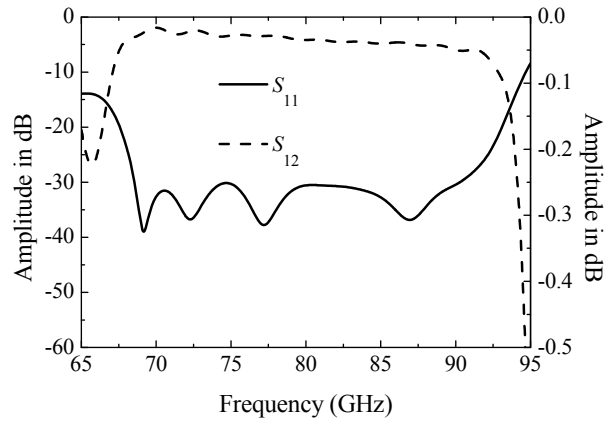


Fig. 2.36 Performance of the designed coupler with reactive loads.

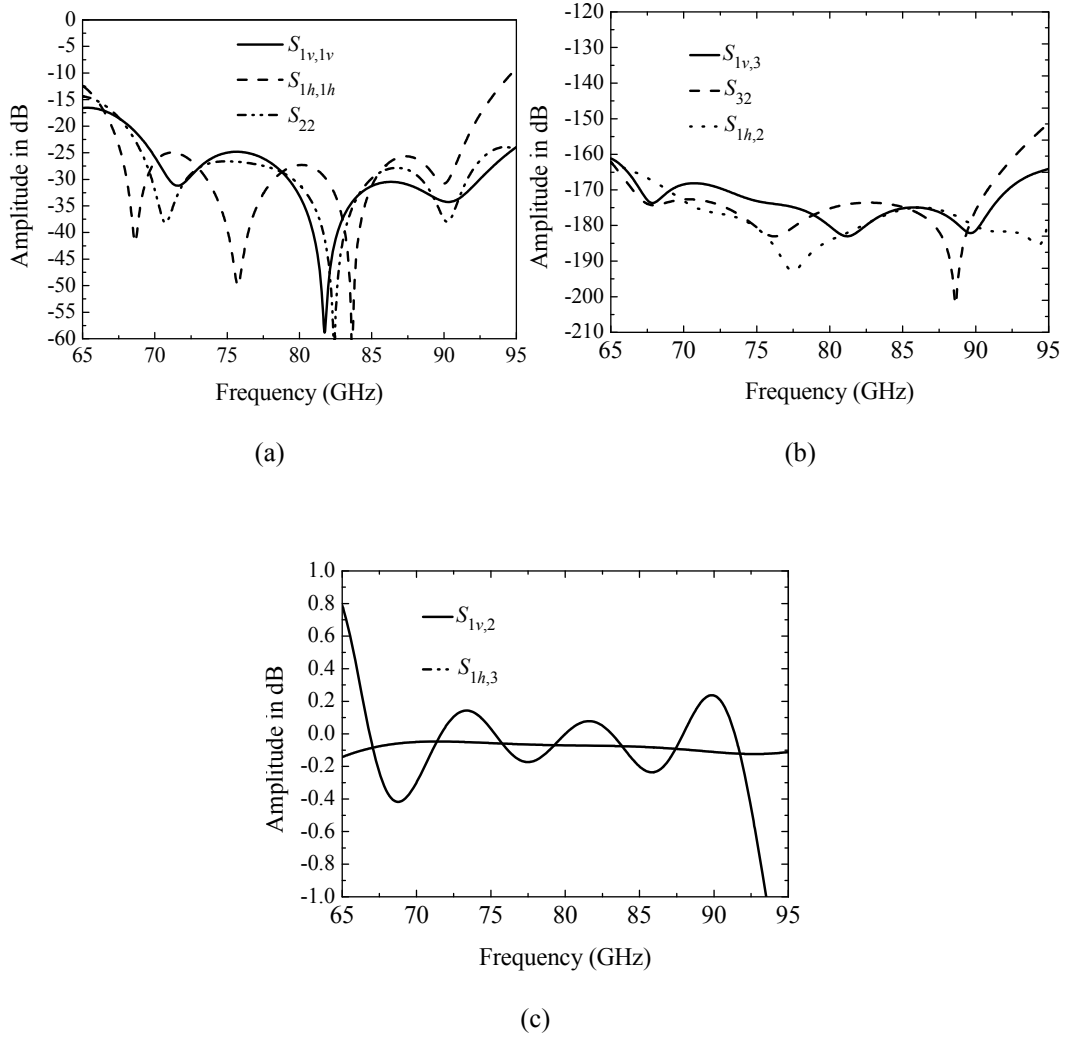


Fig. 2.37 Performance of the optimized polarization-separating junction. (a) Reflection coefficient, (b) polarization discrimination and isolation, and (c) transmission coefficient.

Next, stepped and rounded  $E$ -plane bends are designed. The size of the orthomode transducer is significantly reduced by these types of right-angle bends. The structure and dimensional symbols of the stepped  $E$ -plane bend are shown in Fig. 2.38. The design of

the two-step  $E$ -plane bend is described in Section 2.3. Its performance is shown in Fig. 2.17.

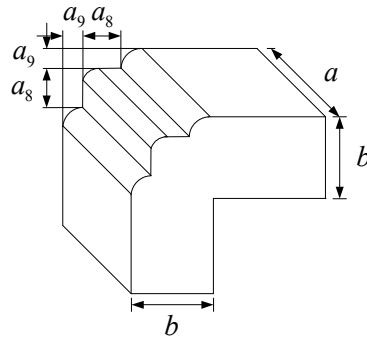


Fig. 2.38 Structure and dimensional symbols of the two-step  $E$ -plane bend.

Fig. 2.39 shows the structure and dimensional symbols of the rounded  $E$ -plane bend used for changing the direction of the waveguide that couples the vertically-polarized wave. In this type of bend, due to one optimization parameter, performance is limited. Optimum value of rounded radius  $r_1$  is 2.08mm, so that  $r_1/b$  is 1.34.

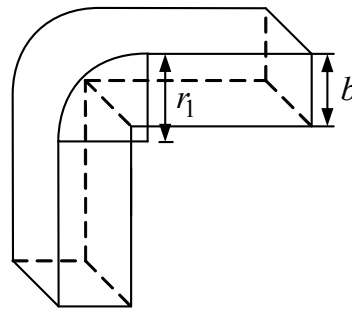


Fig. 2.39 Structure and dimensional symbols of the rounded  $E$ -plane bend.

The performance of the designed rounded  $E$ -plane bend is shown in Fig. 2.40. Over 57.97-95GHz, the reflection coefficient is less than -30dB and transmission coefficient is greater than -0.05dB.

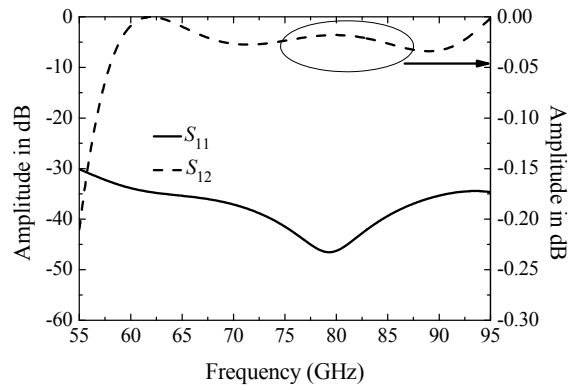


Fig. 2.40 Performance of the designed rounded  $E$ -plane bend.

Fig. 2.41 shows the structure of the  $E$ -plane  $Y$ -junction power combiner consisting of two circular  $E$ -plane bends and a three-step impedance transformer. The design of the  $Y$ -junction power combiner is described before in conjunction with the design of the Bøifot OMT with double ridges. The simulated performance is shown in Fig. 2.21.

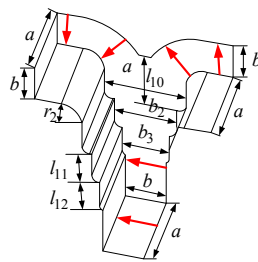


Fig. 2.41 Structure of the  $E$ -plane  $Y$ -junction.

The branch-line OMT is realized by assembling sub-structures that are designed in the above as shown Fig. 2.42. After the assembly, the OMT structure is not optimized further since the OMT's performance satisfies the design goals. If one wants to improve the performance of this OMT, one needs to improve the performance of symmetric backward coupling section only.

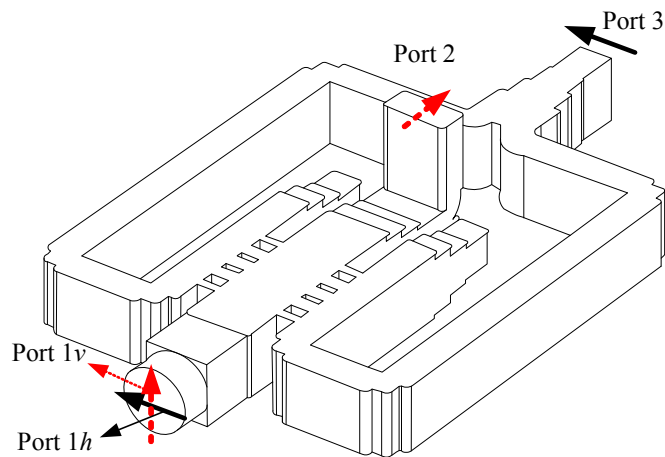
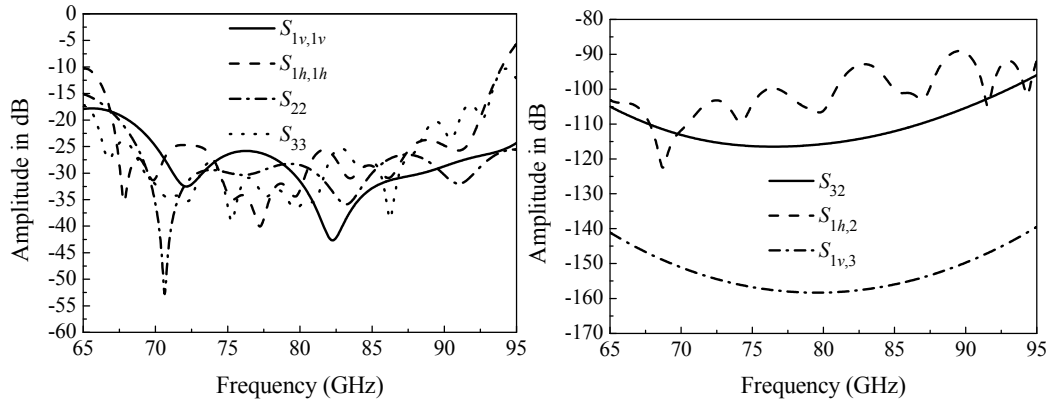


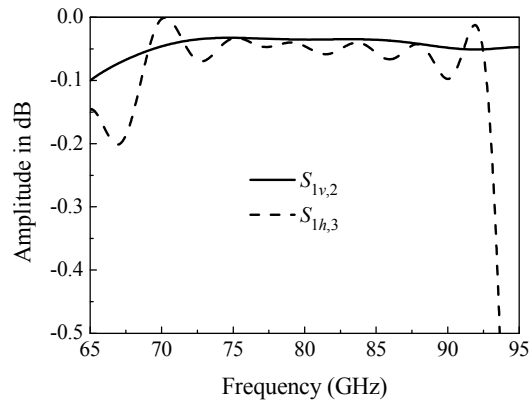
Fig. 2.42 Structure of the designed branch-line OMT.

Fig. 2.43 shows the performance of the designed branch-line OMT. Over 68.05-91.08GHz (28.94% bandwidth), the reflection coefficient is less than -20dB, the polarization discrimination is greater than 85B, the isolation is greater than 90dB and the transmission coefficient is greater than -0.5dB.



(a)

(b)



(c)

Fig. 2.43 Performance of the designed branch-line OMT. (a) Reflection coefficient, (b) isolation and polarization discrimination, (c) transmission coefficient.

## **Chapter III**

### **Fabrication**

Two fabrication techniques have been utilized to produce the designed OMTs. One is the split-block technique. The other is wire-cutting technique. The split-block technique has been investigated and developed by some researchers for high precision, excellent surface quality and low cost [57]-[58]. The structure is separated into two or more pieces at the surface of symmetry. Each piece is machined separately and assembled together.

Aluminum is the choice of material for designed OMTs since it is easy to machine and cheap. Aluminum blocks are machined into complicated OMT sub-blocks using conventional milling operations where the numerical controlled stage generated from a combination of the Autocad™ drawing, commercial CAD/CAM software and Microwave Studio™ electromagnetic simulation software. Working specifications of milling drills are 1) straightforward direction and 2) corner for bends, steps and discontinuity.

The wire cutting technique is used when deep circular or rectangular holes (pipes) are required. This method is efficient because it does not require connection or assembly of parts. This method is used for fabrication of circular-to-rectangular transitions, circular-to-square waveguide transitions, and waveguides for match loads.

A designed OMT is fabricated in three steps. First, its 3D fabrication model is drawn and exported with the filename extension SAT in Microwave Studio™. Then the model is

sent to a machine shop specializing in precision metal machining jobs. Finally, fabricated blocks are assembled using M2 bolts and guide pins.

Grooves are used in the mating surface of split blocks to increase the pressure of the mating faces. The hole patterns of the standard flange for WR-12 waveguide is shown in Fig. 3.1. Table 3.1 shows the dimensions of the flange.

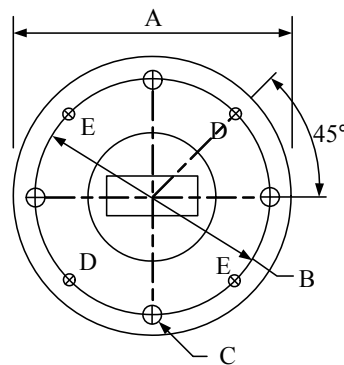


Fig. 3.1 Hole patterns of the standard flange for WR-12 waveguide.

Table 3.1 Dimensions of the standard flange for WR-12 waveguide.

Parameter	mm	Parameter	mm
A	19.05	D Holes	1.613
B	14.29	E Holes	1.555
C Holes	4-40 UNC-2B	All Holes	14.29

Before measuring the performance of a fabricated OMT, a waveguide calibration kit is employed to move measurement planes to the flange surface and to calibrate out reflections and non-ideal transmissions in the measurement system that employs a network analyzer operating at *E*-band (60-90 GHz).

The photograph of the waveguide calibration kit used in this dissertation is shown in Fig. 3.2.

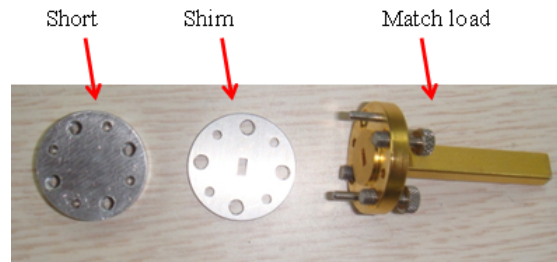
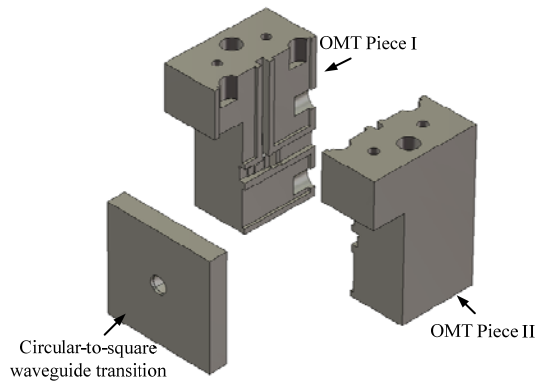


Fig. 3.2 Photograph of the waveguide calibration kit.

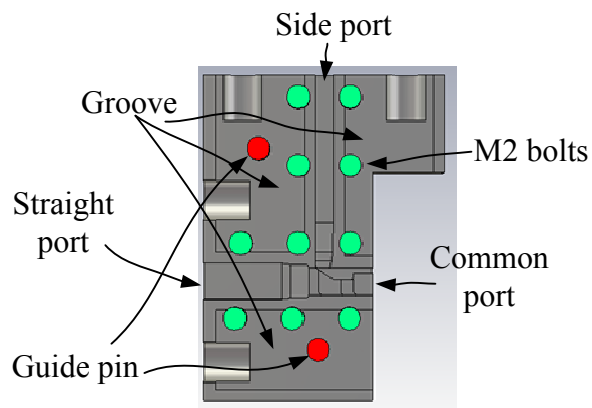
### 3.1 Fabrication of the Dunning OMT

The designed Dunning OMT is fabricated in three sub-blocks as shown in Fig. 3.3. The first block is a circular-to-square waveguide transition. It is fabricated by wire-cutting technique. The second and third ones are one halves of the split-block assembly.

Fig. 3.4 shows the photograph of the fabricated Dunning OMT. Also, the additional components for the Dunning OMT are fabricated by the wire-cutting technique. They are a circular-to-rectangular waveguide transition and a waveguide for the match load absorber for measuring the port isolation.

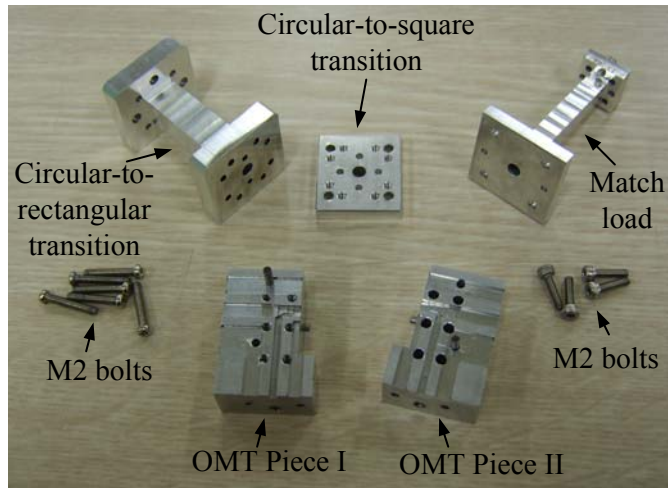


(a)

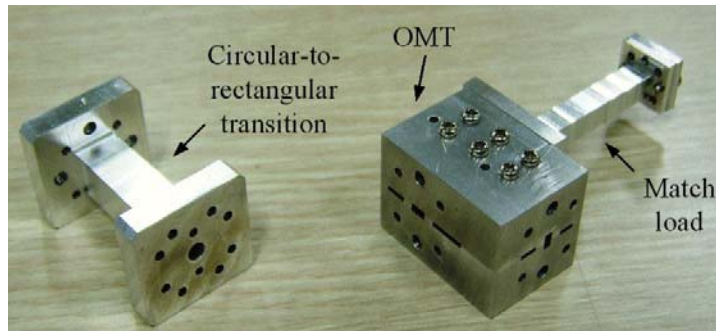


(b)

Fig. 3.3 Fabrication model of the Dunning OMT. (a) 3D model and (b) inside vies of piece II.



(a)



(b)

Fig. 3.4 Photograph of the fabricated Dunning OMT. a) Before assembly and b) after assembly.

### 3.2 Fabricaion of the Bøifot OMT with Double Ridges

The Bøifot OMT is fabricated by split-block technique in two pieces. Fig. 3.5 shows the mating plane of two split blocks. Fig. 3.6 shows the 3D model for the fabrication of this OMT.

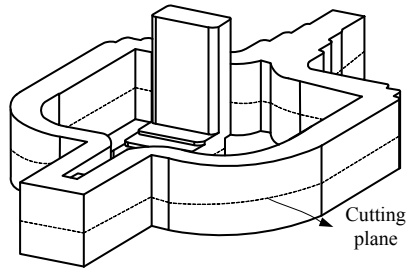
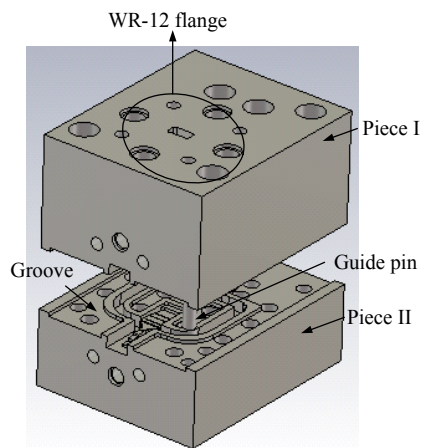
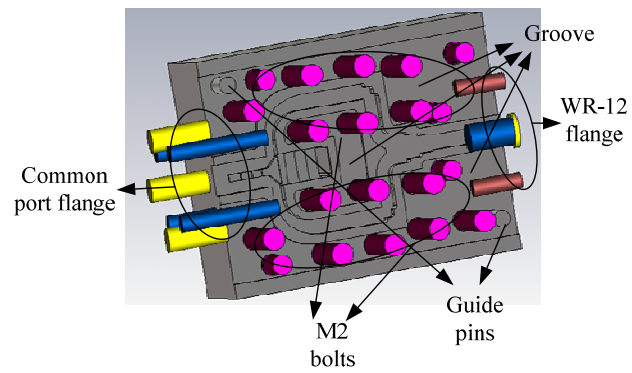


Fig. 3.5 Mating plane of two split blocks in the fabrication of the Bøifot OMT with double ridges.



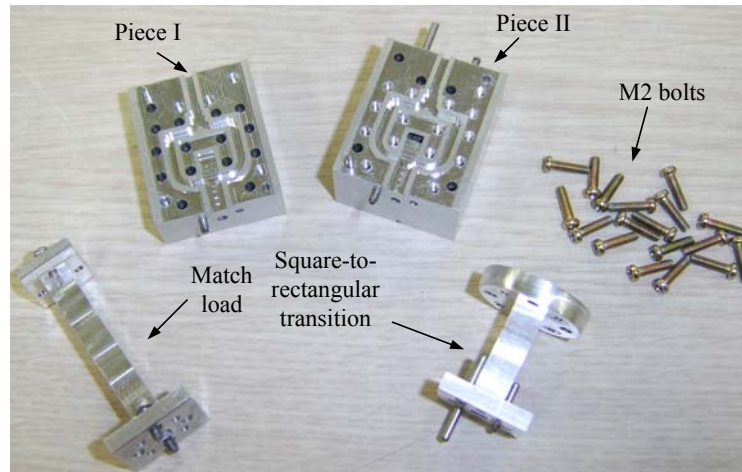
(a)



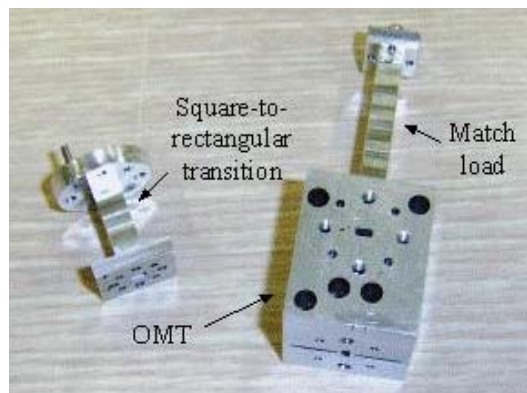
(b)

Fig. 3.6 Fabrication model for the Bøifot OMT with double ridges. (a) 3D model and (b) inside view of the split block.

Fig. 3.7 shows the photograph of the fabricated Bøifot OMT with double ridges. The square-to-rectangular transition and waveguide for matched load are fabricated by wire-cutting technique. A square-to-rectangular transition of linearly taper is employed.



(a)



(b)

Fig. 3.7 Photograph of the fabricated Bøifot OMT with double ridges. (a) Before assembly and (b) after assembly.

### 3.3 Fabrication of the Branch-Line OMT

The fabrication method of the designed branch-line OMT is same as that for the Bøifot OMT with double ridges. Fig. 3.8 shows the mating plane of two split blocks. Fig. 3.9 shows the fabrication model for the branch-line OMT. Fig. 3.10 shows the photograph of the fabricated branch-line OMT and additional components used in the measurement

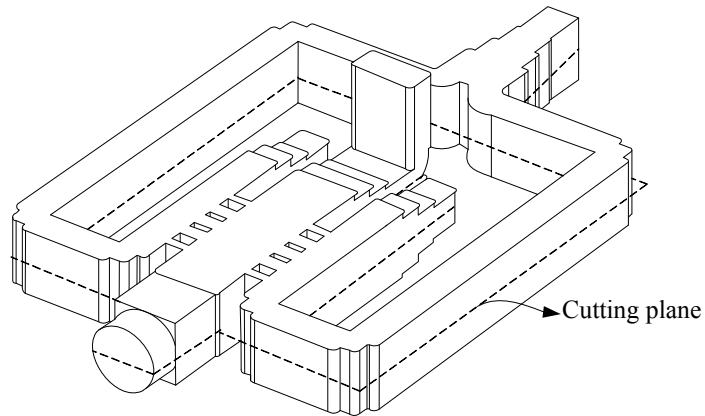
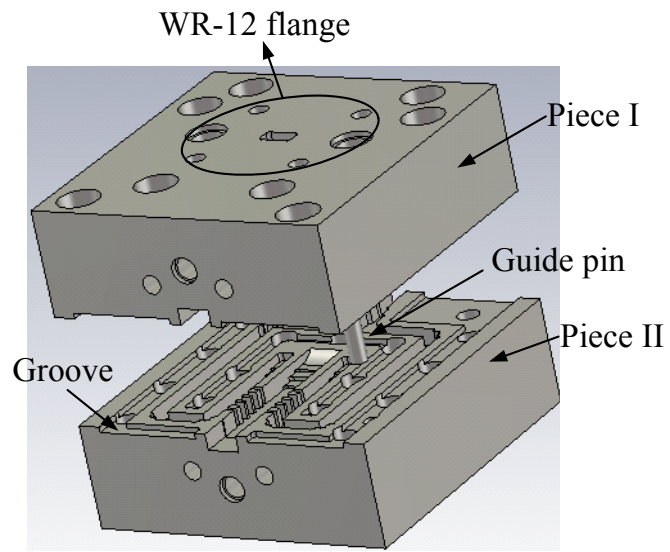
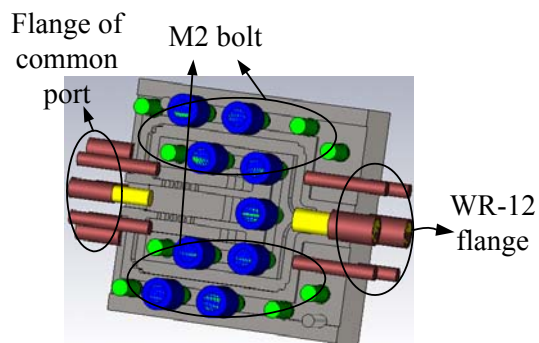


Fig. 3.8 Mating plane of two blocks of the branch-line OMT.

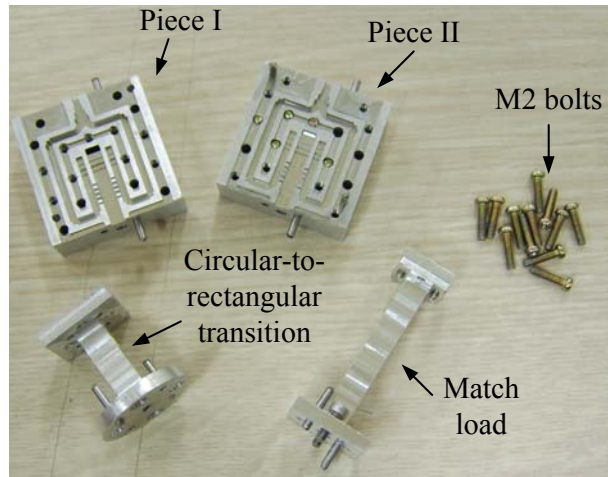


(a)

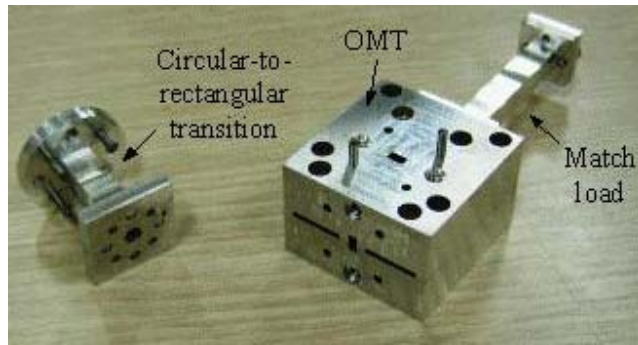


(b)

Fig. 3.9 Fabrication model of the branch-line OMT. (a) 3D model and (b) internal view of a split block.



(a)



(b)

Fig. 3.10 Photograph of the fabricated branch-line OMT. (a) Before assembly and (b) after assembly.

## Chapter IV

### Measurement

Before measuring the fabricated OMTs, the full two-port calibration is required in a vector network analyzer. Fig 4.1 shows reflection and transmission coefficients of at the planes of ports 2 and 3 while ports 2 and 3 of the network analyzer are connected to each other. Over 60-95GHz, the reflection coefficient is less than -35dB and accuracy of the transmission coefficient is within +0.08/-0.05dB.

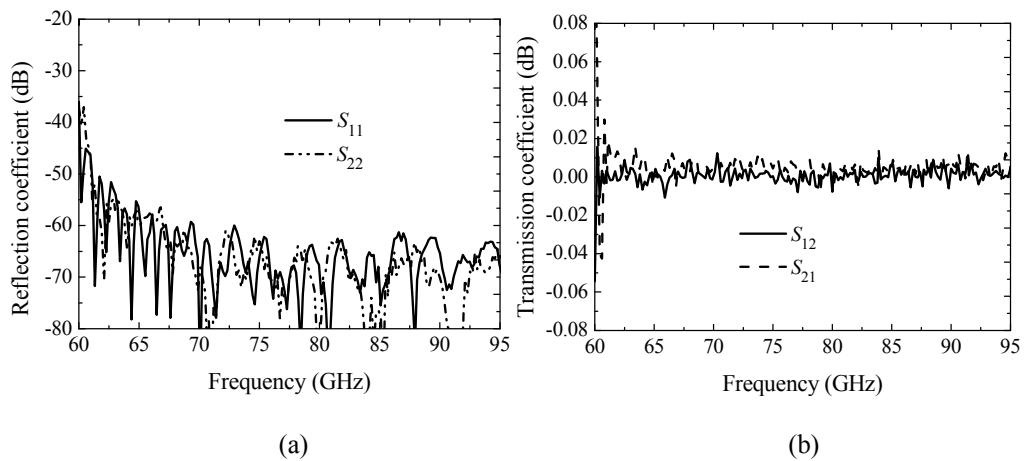


Fig. 4.1 Calibrated performance of the network analyzer. (a) Reflection and (b) transmission coefficients.

When measuring the fabricated OMT, a matched load is required in the common port. The CTL-0880 type of microwave absorber by Microwave Device Laboratories is

employed to construct a matched load for the common port. The structure and photograph of the fabricated matched load are shown in Fig. 4.2, while its dimensions are shown in Table 4.1.

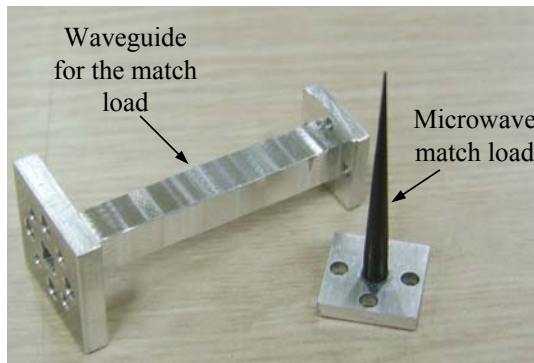
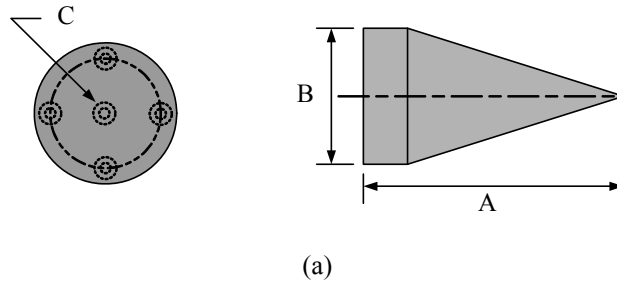
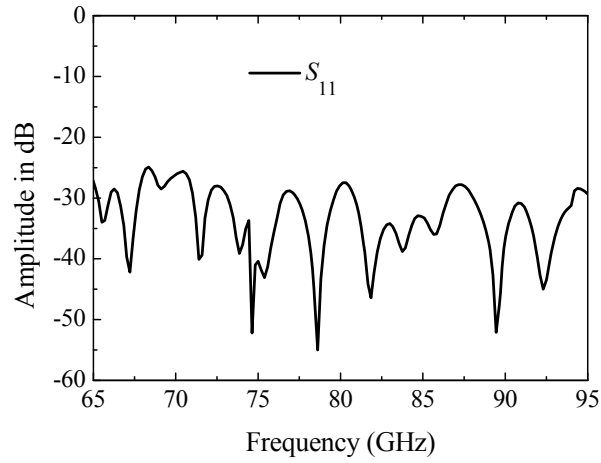


Fig. 4.2 (a) Structure and (b) photograph of the absorbing material.

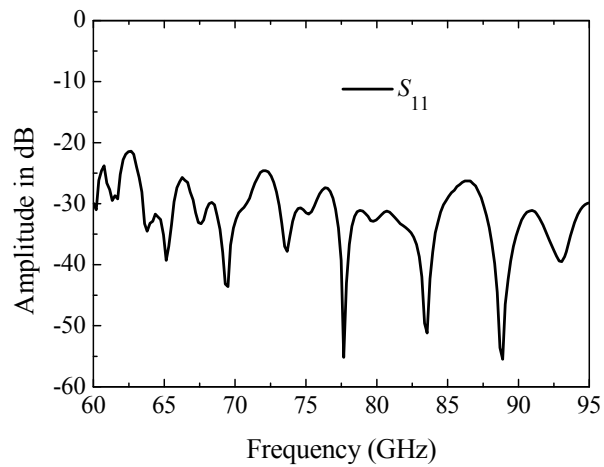
Table 4.1 Characteristic of the absorber material

Catalog Number	WR-No	Frequency range	Max VSWR	A in mm	B in mm	C hole
CTL-0880	22	33-50GHz	1.01	29.97	2.79	1/64"X.10"

Fig. 4.3 shows the measured reflection coefficient of the matched load. The fabricated matched load has a reflection coefficient of less than -25dB over 60-95GHz, which is too large for the reflection coefficient of a matched load. Ideally it should be less than -50dB over the measurement frequency.



(a)



(b)

Fig. 4.3 Reflection coefficient of matched loads in (a) cylindrical and (b) square waveguides.

## 4.1 Measurement of the Dunning OMT

After calibration, the fabricated Dunning OMT is measured. Figs. 4.4 and 4.5 shows the measurement setup.

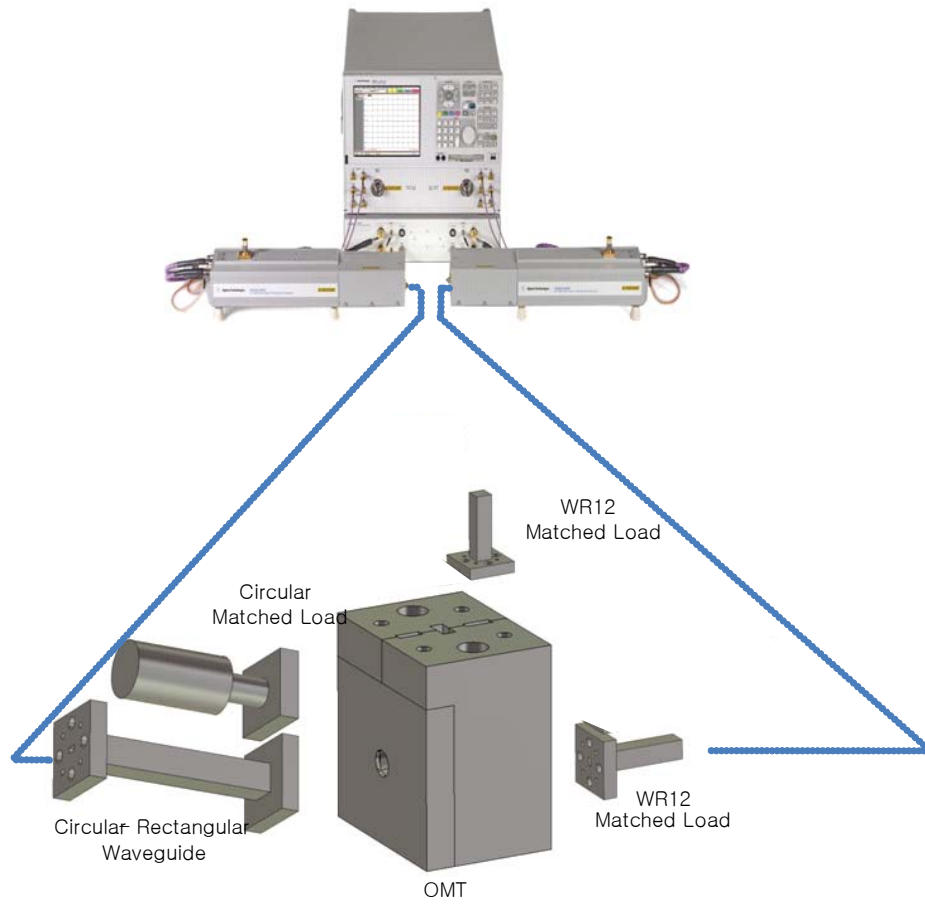


Fig. 4.4 Network analyzer measurement setup.

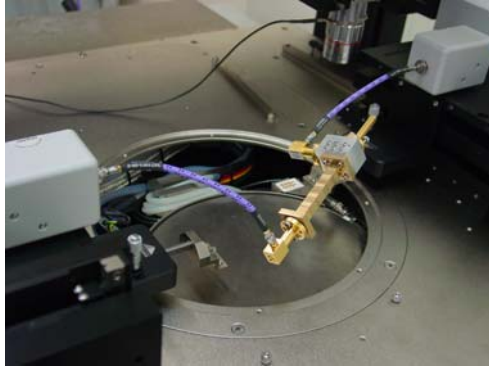


Fig. 4.5 Photograph of the Dunning OMT under test.

Figs. 4.6 to 4.8 show the measured performance of the fabricated Dunning OMT. The agreement between the measurement and the simulation is not good. Table 4.2 shows the comparison between design goals and performances of the fabricated Dunning OMT. The simulated performance of the designed Dunning OMT satisfies design goals. The measured reflection coefficient and measured polarization discrimination of the fabricated Dunning OMT do not satisfy design goals but measured reflection coefficients are very close to design goals. The measured polarization discrimination is far from design goals. Table 4.3 shows the comparison between specified and fabricated dimensions.

The big difference between simulated and fabricated dimensions is the depth in split blocks with a maximum error of 12.3%. In Fig 2.9, this parameter ( $b_3$ ) has a significant effect on the level of the reflection coefficient. It may be a main reason for the difference between simulated and measured performances. Measured dimensions of the fabricated OMT are only approximately values. Also, there are other errors such as flange misalignment and misaligned split blocks. Dunning describes the effect of misalignment

on isolation and polarization discrimination, which are very sensitive to a small amount of misalignment of waveguide flange and split blocks [1].

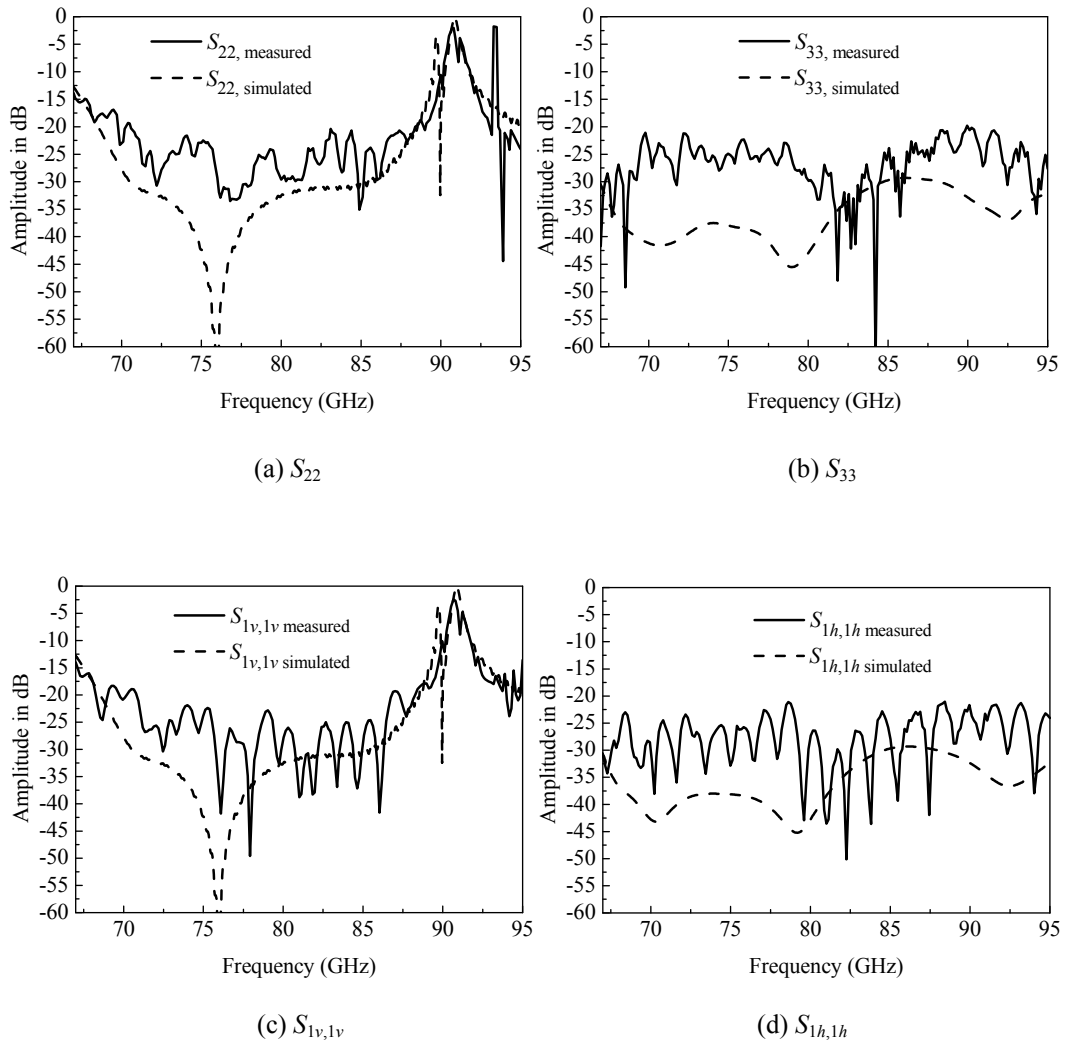
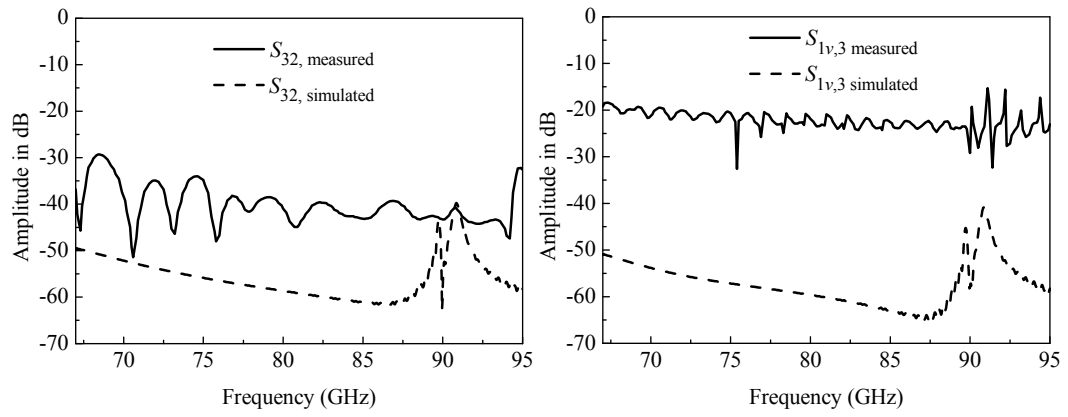
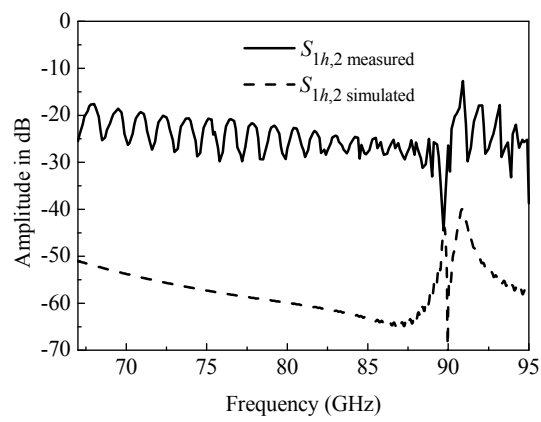


Fig. 4.6 Measured reflection coefficients of the fabricated Dunning OMT.



(a)  $S_{32}$

(b)  $S_{1v,3}$



(c)  $S_{1h,2}$

Fig. 4.7 Measured isolation and polarization discrimination of the fabricated Dunning OMT.

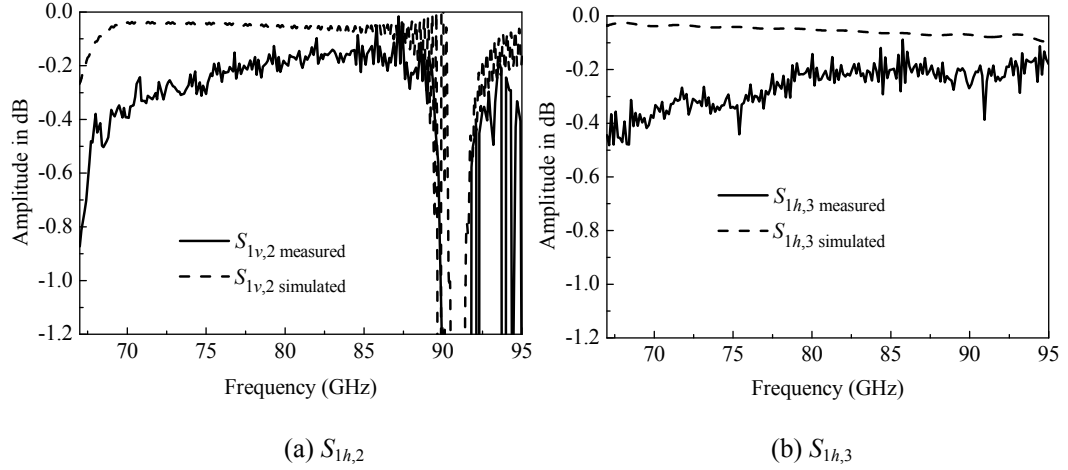


Fig. 4.8 Measured transmission coefficients of the fabricated Dunning OMT.

Table 4.2 Comparison between design goals and performances of the fabricated Dunning OMT.

Performance	Design goal	Simulated performance	Fabricated performance	Remarks
Reflection ( $R$ )	$\leq -20\text{dB}$	$\leq -25\text{dB}$	$\leq -18.5\text{dB}$	Not satisfied
Transmission ( $T$ )	$\geq -0.5\text{dB}$	$\geq -0.16\text{dB}$	$\geq -0.42\text{dB}$	Satisfied
Isolation ( $I$ )	$\geq 30\text{dB}$	$\geq 50\text{dB}$	$\geq 33\text{dB}$	Satisfied
Discrimination ( $D$ )	$\geq 30\text{dB}$	$\geq 50\text{dB}$	$\geq 19\text{dB}$	Not satisfied
Bandwidth ( $B$ )	70-87GHz	70-87GHz	70-88.5GHz	

Table 4.3 Specified and fabricated dimensions of the Dunning OMT in mm.

(a) Width

	$a_0$	$a_1$	$a_4$	$b_{10}$	$b_{11}$	$b_{12}$	$b_{13}$	$b_{14}$
Specified	3.1	2.89	2.43	1.55	1.47	1.42	1.27	1.08
Fabricated piece I	3.08 (-0.02)	2.88 (-0.01)	2.41 (-0.02)	1.54 (-0.01)	1.45 (-0.02)	1.42 (0)	1.26 (-0.01)	1.07 (-0.01)
Fabricated piece II	3.12 (+0.02)	2.84 (-0.05)	2.41 (-0.02)	1.55 (0)	1.47 (0)	1.42 (0)	1.27 (0)	1.07 (-0.01)

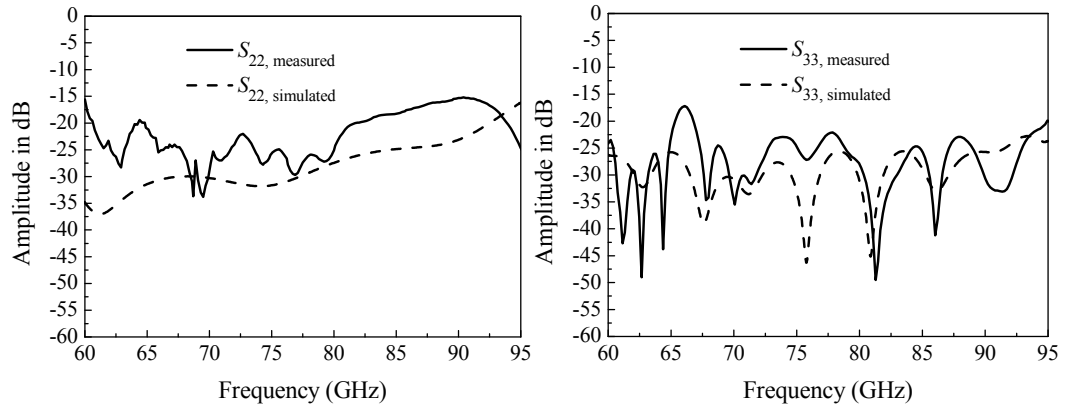
	$b_{15}$	$l_1$	$l_2$	$l_3$	$l_4$	$l_5$	$l_6$
Specified	0.48	0.8	1.55	0.9	1.88	1.2	1.6
Fabricated piece I	0.49 (+0.01)	0.79 (+0.01)	1.54 (-0.01)	0.9 (0)	1.89 (+0.01)	1.21 (+0.01)	1.58 (-0.02)
Fabricated piece II	0.49 (+0.01)	0.79 (+0.01)	1.55 (0)	0.92 (+0.02)	1.85 (-0.03)	1.22 (+0.02)	1.58 (-0.02)

(b) Depth

	$a_{10}$	$b_0$	$b_3$	$b_4$	$b_5$	$b_6$
Specified	3.1	1.55	<b>1.06</b>	1.92	2.3	2.3
Fabricated	3.07 (-0.03)	1.62 (+0.07)	<b>0.93</b> <b>(-0.13)</b>	1.68 (+0.05)	1.93 (+0.01)	2.28 (-0.02)

## 4.2 Measurement of the Bøifot OMT with Double Ridges

Next, the fabricated Bøifot OMT with double ridges is measured. The comparison between the measured and simulated performances is shown in Figs. 4.9 to 4.10. Also, there are differences between simulated and measured performances.

(a)  $S_{22}$ (b)  $S_{33}$

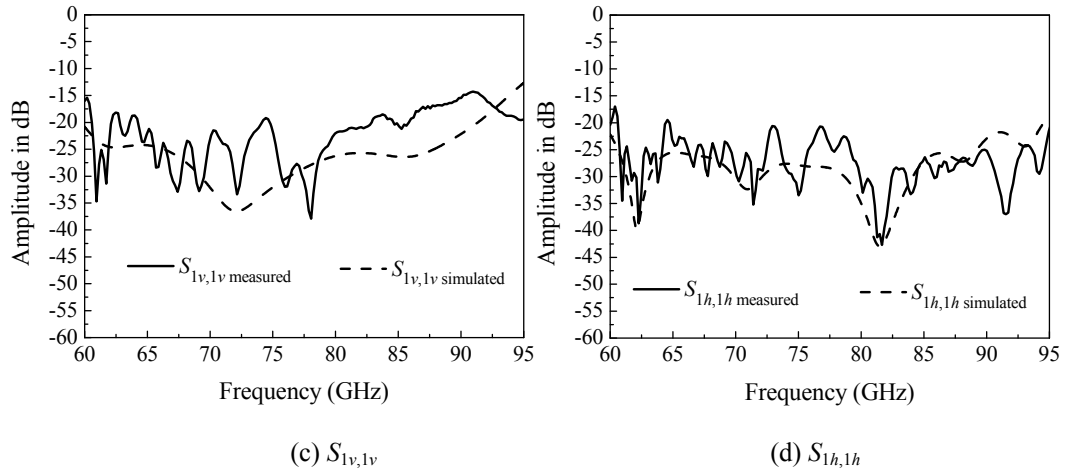


Fig. 4.9 Measured reflection coefficients of the fabricated Bøifot OMT with double ridges.

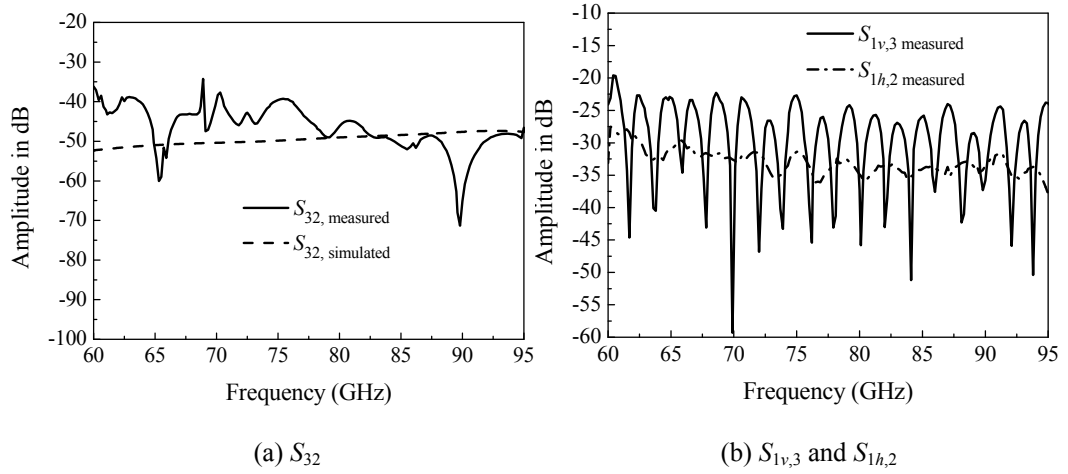


Fig. 4.10 Measured isolation and polarization discrimination of the fabricated Bøifot OMT with double ridges.

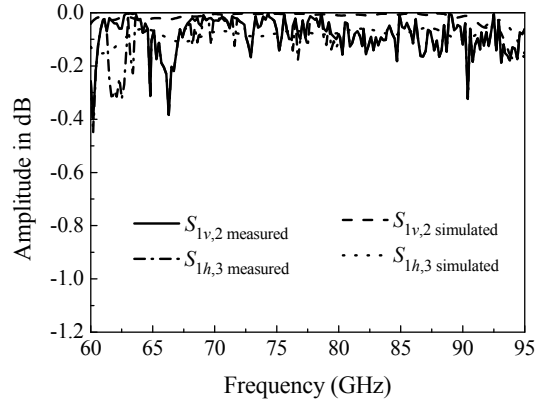


Fig. 4.11 Measured transmission coefficients of the fabricated Bøifot OMT with double ridges.

Table 4.4 shows the comparison between design goals and performances of the fabricated Bøifot OMT. The simulated performance of the Bøifot OMT satisfies design goals. The measured port isolation and transmission coefficient satisfy design goals. Reflection coefficients and polarization discrimination of the fabricated Bøifot OMT do not satisfy design goals.

Table 4.4 Comparison between design goals and performances of the fabricated Bøifot OMT.

Performance	Design goal	Simulated performance	Fabricated performance	Remarks
Reflection ( $R$ )	$\leq -20\text{dB}$	$\leq -20\text{dB}$	$\leq -16\text{dB}$	Not satisfied
Transmission ( $T$ )	$\geq -0.5\text{dB}$	$\geq -0.15\text{dB}$	$\geq -0.48\text{dB}$	Satisfied
Isolation ( $I$ )	$\geq 30\text{dB}$	$\geq 45\text{dB}$	$\geq 35\text{dB}$	Satisfied
Discrimination ( $D$ )	$\geq 30\text{dB}$	$\geq 58\text{dB}$	$\geq 20\text{dB}$	Not satisfied
Bandwidth ( $B$ )	60-90GHz	60-90GHz	60-90GHz	

Table 4.5 shows the comparison between specified and fabricated dimensions of the Bøifot OMT with double ridges. In Table 4.5,  $h_c$  has a maximum tolerance of 6.3%. From Fig 2.25, it has a significant effect on the level of the reflection coefficients. Also, there

are other reasons for differences between simulated and measured performances, which are misalignments in flange contact and assembly of split blocks.

Table 4.5 Specified and fabricated dimensions of the Boifot OMT in mm.

(a) Width

	$a$	$a_8$	$a_9$	$b$	$b_1$	$b_2$	$b_3$	$t$
Specified	3.1	0.77	0.39	1.55	1.18	2.36	1.8	0.73
Fabricated piece I	3.05 (-0.05)	0.76 (-0.01)	2.41 (-0.02)	1.48 (-0.07)	1.15 (-0.03)	2.32 (-0.04)	1.75 (-0.05)	0.73 (0)
Fabricated piece II	3.03 (-0.07)	0.76 (-0.01)	2.41 (-0.02)	1.5 (-0.05)	1.14 (-0.04)	2.3 (-0.06)	1.75 (-0.05)	0.7 (-0.03)

	$l$	$l_1$	$l_2$	$l_3$	$l_4$	$l_5$	$l_6$	$l_7$
Specified	1.5	1.18	1.12	1	1.77	0.65	1.08	1.12
Fabricated piece I	1.49 (-0.01)	1.18 (0)	1.12 (0)	1 (0)	1.76 (-0.01)	0.66 (+0.01)	1.07 (-0.01)	1.12 (0)
Fabricated piece II	1.48 (-0.02)	1.17 (-0.01)	1.12 (0)	0.99 (-0.01)	1.77 (0)	0.66 (+0.01)	1.08 (0)	1.13 (+0.01)

	$l_8$	$l_9$	$l_{10}$	$l_{11}$	$l_{12}$	$l_{13}$	$h_c$
Specified	1.12	3.93	2.38	1.32	1.31	9.53	<b>1.11</b>
Fabricated piece I	1.05 (-0.06)	4 (+0.07)	2.22 (-0.16)	1.33 (+0.01)	1.31 (0)	9.55 (+0.02)	<b>1.12 (+0.01)</b>
Fabricated piece II	1.05 (-0.07)	3.97 (+0.04)	2.22 (-0.16)	1.33 (+0.01)	1.31 (0)	9.56 (+0.03)	<b>1.18 (+0.07)</b>

(b) Depth

	$a_1$	$a_2$	$a_3$	$a_4$	$a_5$	$a_6$	$a_7$
Simulated	2.55	1.83	1.32	1.1	0.87	0.97	1.29
Fabricated	2.55 (0)	1.84 (+0.01)	1.33 (+0.01)	1.12 (+0.01)	0.88 (+0.01)	1.03 (+0.06)	1.28 (-0.01)

### 4.3 Measurement of the Branch-Line OMT

Finally, the fabricated branch-line OMT is measured. The comparison between the measured and simulated performances is shown in Figs. 4.12 to 4.14. Also, there are differences between simulated and measured performances.

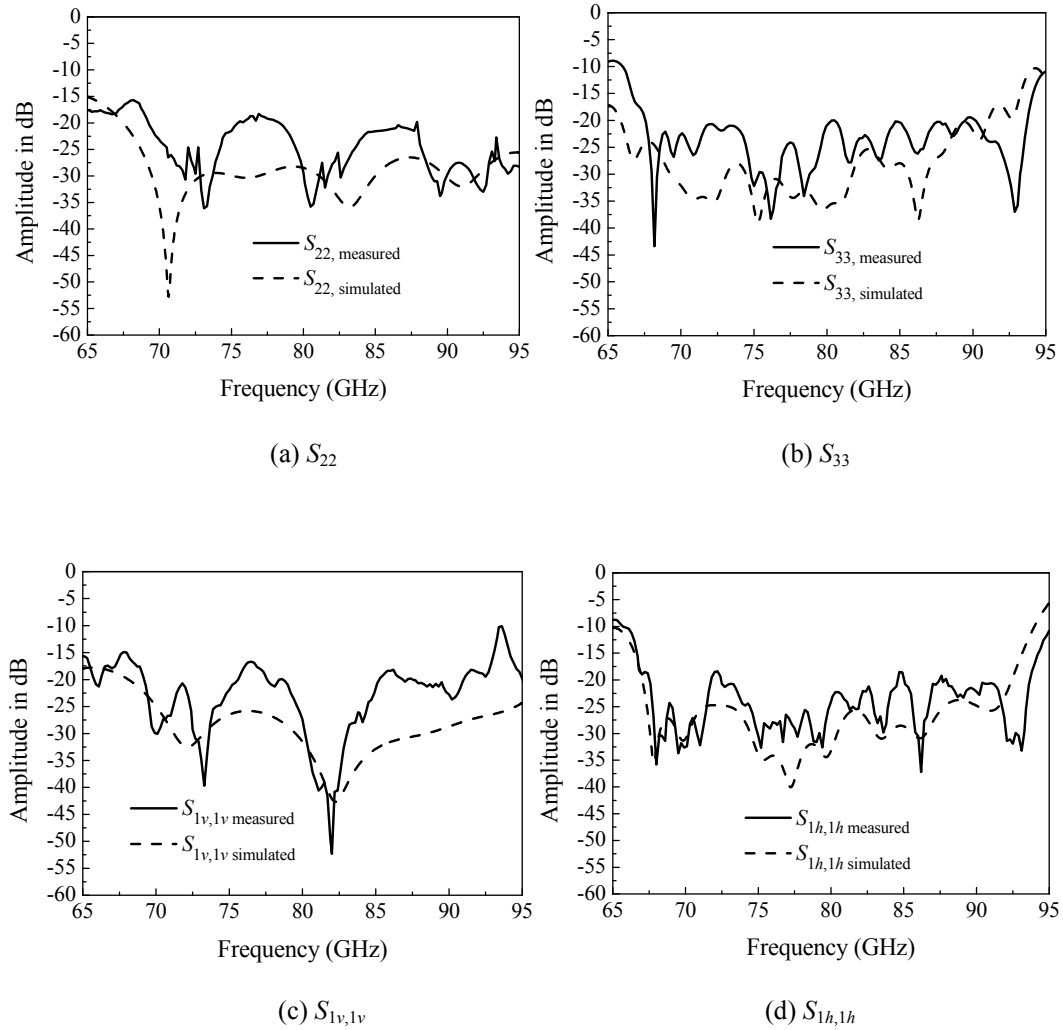


Fig. 4.12 Measured reflection coefficients of the fabricated branch-line OMT.

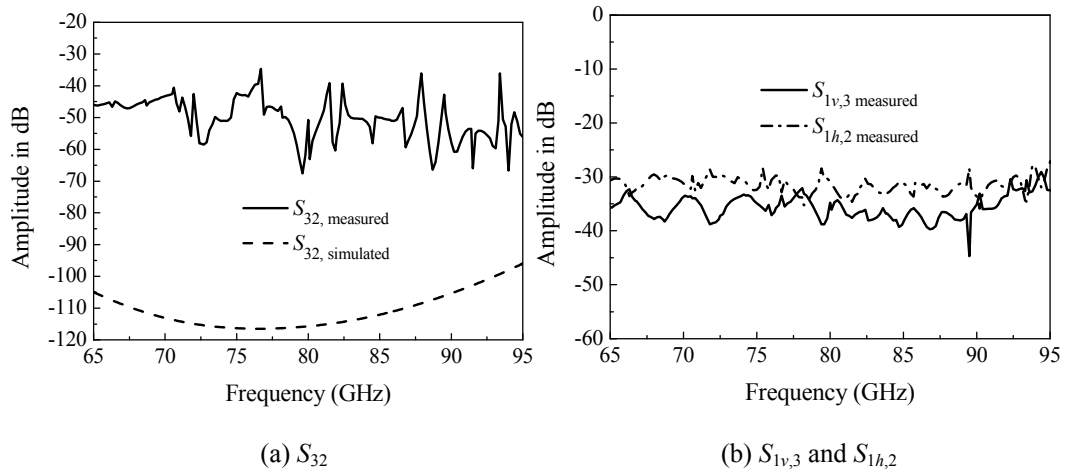


Fig. 4.13 Measured isolation and polarization discrimination of the fabricated branch-line OMT.

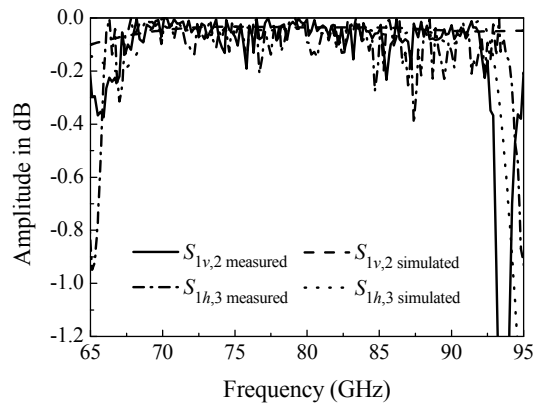


Fig. 4.14 Measured transmission coefficients of the fabricated branch-line OMT.

Table 4.6 shows the comparison between design goals and performances of the fabricated branch-line OMT. The simulated performance satisfies design goals of the branch-line OMT. The measured performance satisfies design goals except the reflection coefficient. The level of the reflection coefficient is close to design goals.

Table 4.6 Comparison between design goals and performances of the fabricated branch-line OMT.

Performance	Design goal	Simulated performance	Fabricated performance	Remarks
Reflection ( $R$ )	$\leq -20\text{dB}$	$\leq -23\text{dB}$	$\leq -17\text{dB}$	Not satisfied
Transmission ( $T$ )	$\geq -0.5\text{dB}$	$\geq -0.08\text{dB}$	$\geq -0.38\text{dB}$	Satisfied
Isolation ( $I$ )	$\geq 30\text{dB}$	$\geq 90\text{dB}$	$\geq 35\text{dB}$	Satisfied
Discrimination ( $D$ )	$\geq 30\text{dB}$	$\geq 85\text{dB}$	$\geq 30\text{dB}$	Satisfied
Bandwidth ( $B$ )	70-87GHz	70-87GHz	70-87GHz	

Dimensions of the fabricated branch-line OMT are measured and shown in Table 4.7. The  $a_3$  has a maximum error of 4.2%. It has a significant effect on the transmission coefficient of the straight port. Differences between simulated and measured performances are due to fabrication errors, which include flange misalignment and misaligned split blocks.

Table 4.7 Specified and fabricated dimensions of the branch-line OMT in mm.

(a) Width

	$a$	$a_1$	$a_2$	$a_3$	$a_8$	$a_9$	$b_2$	$b_3$
Specified	3.1	0.41	0.68	<b>0.71</b>	0.77	0.39	2.36	1.8
Fabricated piece I	3.08 (-0.03)	0.39 (-0.02)	0.67 (-0.01)	<b>0.69</b> <b>(-0.02)</b>	0.78 (+0.01)	0.37 (-0.02)	2.31 (-0.05)	1.79 (-0.01)
Fabricated piece II	3.08 (-0.03)	0.39 (-0.02)	0.66 (-0.02)	<b>0.68</b> <b>(-0.03)</b>	0.75 (-0.02)	0.37 (-0.02)	2.33 (-0.03)	1.75 (-0.05)

	$l_1$	$l_2$	$l_3$	$l_7$	$l_8$	$l_9$	$l_{11}$	$l_{12}$
Specified	1.09	0.99	2.6	1.07	1.06	1.45	1.32	1.31
Fabricated piece I	1.08 (-0.01)	0.99 (0)	2.57 (-0.03)	1.06 (-0.01)	1.11 (+0.05)	1.48 (+0.03)	1.33 (+0.01)	1.31 (0)
Fabricated piece II	1.1 (+0.01)	0.99 (0)	2.63 (+0.03)	1.06 (-0.01)	1.05 (-0.01)	1.42 (-0.03)	1.3 (-0.02)	1.3 (-0.01)

(b) Depth

	$a_5$	$a_6$	$a_7$
Simulated	2.64	1.89	1.55
Fabricated	2.64 (0)	1.84 (-0.05)	1.5 (-0.05)

## Chapter V

### Conclusion

In this dissertation, design and fabrication of the wideband OMT (Orthomode Transducer) are investigated, which include the Dunning type, the Bøifot junction and branch-line OMT. Existing structures of each OMT are improved for easier fabrication and better performance.

The design goals of wideband OMTs are as follows: reflection coefficient less than -20dB, transmission coefficient greater -0.5dB, polarization discrimination greater than 30dB and port isolation greater than 30dB over the desired operating bandwidth.

The structures and operating principles of each OMT is described using 3D and 2D field distribution inside the OMT structure. The design procedures of each OMT are presented. Sub-blocks of an OMT such as the polarization-separating junction, waveguide transitions, impedance matching sections, waveguide bends and Y-junction power combiner are designed separately and then assembled together. The assembled structure is further optimized for the best performance.

The designed Dunning OMT has an inner dimension ( $L \times W \times H$ ) of 13.21mm x 3.1mm x 7.69mm and a bandwidth of 25.5%. The designed Bøifot OMT and branch-line OMT have an inner dimension of 24.48mm x 14.07mm x 6.98mm and 30.29mm x 18mm x 6.32mm, and bandwidths of 42.0%, and 28.9%, respectively. The simulated performance satisfies design goals.

The designed OMTs are fabricated by split-block technique. The dimensions of the fabricated OMTs are measured and compared with specified dimensions. The fabricated Dunning, Bøifot and branch-line OMTs have maximum dimensional errors of 12.3%, 6.3% and 4.3%, respectively. Performances of the fabricated OMTs are measured for design verification. Due to fabrication errors, flange misalignment and misaligned split blocks, there are differences between simulated and measured performances. The measured performances of the fabricated OMTs do not fully satisfy design goals. With better precision in fabrication and assembly, one can obtain a good agreement between the measurement and the simulation.

The wideband fabricated OMTs presented in this dissertation can be used in satellite communication in millimeter-wave bands and radio astronomy. Their use in communication systems allows one to greatly increase the capacity of the system. In the future work, some improvements in fabrication and measurement are required:

- More accurate fabrication is necessary to bring the measured performance close to the simulation.
- Better flange mating is required to reduce the measurement error.
- New polarization-separating junctions need to be investigated such that it is robust to fabrication errors.

## REFERENCES

- [1] A. Dunning, S. Srikanth and A. R. Kerr, "A simple orthomode transducer for centimeter to submillimeter wavelengths," *Proc. 20<sup>th</sup> Int. Symp. Space Terahertz Tech.*, Apr. 2009, pp. 191-194.
- [2] A. Navarrini and M. Carter, "Design of a dual polarization SIS sideband separating receiver based on waveguide OMT for the 275-370GHz frequency band," *Proc. 14th Int. Space Terahertz Technol. Symp.*, Tucson, AZ, Apr. 2003, pp. 159–168.
- [3] G. Narayanan, and N. Erickson, "Full-waveguide band orthomode transducer for the 3mm and 1mm bands," *Proc. 14th Int. Symp. Space Terahertz Tech.*, Cambridge, 26-28 Mar. 2002, pp. 504-514.
- [4] R. Banham, G. Valsecchi, L. Lucci, G. Pelosi, S. Selleri, V. Natale, R. Nesti, and G. Tofani, "Electroformed front-end at 100 GHz for radio-astronomical applications," *Microw. J.*, Vol. 48, No. 8, pp. 112-122, Aug. 2005.
- [5] A. M. Bøifot, E. Lier, T. Schaug-Pettersen, "Simple and broadband orthomode transducer," *European Trans. Telecom. Related Tech.*, Vol. 2, No. 5, pp. 503-510, 1991.
- [6] J. A. Ruiz-Cruz, J. R. Montejo-Garai, J. M. Rebollar, C. E. Montesano, M. J. Martin and M. Naranjo-Masi, "Computer aided design of wideband orthomode transducers based on the Bøifot junction," *IEEE MTT-S Int. Microwave Symp. Dig.*, 2006, pp. 1173-1176.
- [7] A. J. Ruiz-Cruz, R. Montejo-Garai, J. M. Rebollar and J. M. Montero, "C-band orthomode transducer for compact and broadband antenna feeders," *Electron. Lett.*, Vol. 45, No 16, pp. 813-814, July 2009.

- [8] A. J. Ruiz-Cruz, R. Montejo-Garai and J. M. Rebollar, "Full-wave modeling and optimization of Bøifot ortho-mode transducers," *Int. J. RF Microw. Comp.-Aided Eng.*, Vol. 18, No. 4, pp. 303-313, 2008.
- [9] E. J. Wollack, W. Grammer and J. Kingsley, "The Bøifot orthomode junction," ALMA Memo 425, National Radio Astronomy Observatory, May 2002.
- [10] E. Wollack, "A full waveguide band orthomode junction," NRAO, EDIR Memo Series #303, May 1996.
- [11] A. Dunning, "Double ridged orthogonal mode transducer for the 16-26GHz microwave band," *Proc. Workshop Appl. Radio Sci.*, Feb. 2002.
- [12] G. G. Moorey, R. Bolton, A. Dunning, R. Gough, R. H. Kanoniuk and L. Reilly, "A 77-117 GHz cryogenically cooled receiver for radio astronomy," *Proc. Workshop Appl. Radio Sci.*, Leura, NSW, 15-17 February, 2006.
- [13] S. Asayama, S. Kawashima, H. Iwashita, M. Inata, Y. Obuchi, T. Suzuki, and T. Wada, "Design and development of ALMA band 4 cartridge receiver," *Proc. 19<sup>th</sup> Int. Symp. Space Terahertz Tech.*, Apr. 2008, pp. 244-249.
- [14] M. Kamikura, M. Naruse, S. Asayama, N. Satou, W. Shan and Y. Sekimoto, "Development of a 385-500GHz orthomode transducer," *Proc. 19<sup>th</sup> Int. Symp. Space Terahertz Tech.*, Apr. 2008, pp. 557-562.
- [15] N. Reyes, P. Zorzi, F. P. Mena, C. Granet, E. Michael, L. Bronfma and J. May, "Design of a heterodyne receiver for band 1 of ALMA," *Proc. 20<sup>th</sup> Int. Symp. Space Terahertz Tech.*, Apr. 2009, pp. 311-314.
- [16] T.-L. Zhang, Z.-H. Yan, L. Chen and F.-F. Fan, "Design of broadband orthomode transducer based on double ridged waveguide," *Proc. Int. Conf. Microw. Millim. Wave Tech.*, May 2010, pp. 765-768.
- [17] O. A. Peverini, R. Tascone, A. Olivieri and R. Orta, "Orthomode transducer for millimeter-wave correlation receivers," *IEEE Trans. Microwave Theory Tech.*, Vol. 54, No. 5, pp. 2042-2049, May. 2006.

- [18] A. Navarrini and R. Nesti, "Symmetric reverse-coupling waveguide orthomode transducer for the 3-mm band," *IEEE Trans. Microwave Theory Tech.*, Vol. 57, No. 1, pp. 80-88, Jan. 2009.
- [19] A. Navarrini and R. Nesti, "Backward couplers waveguide orthomode transducer for 84-116GHz," *Proc. 19<sup>th</sup> Int. Symp. Space Terahertz Tech.*, Apr. 2008, pp. 358-367.
- [20] A. A. San Blas, F. Mira, J. Gil, V. E. Boria and B. Gimeno, "Efficient analysis and design of compensated turnstile junctions using advanced modal techniques," *Progress in Electromag. Res. Lett.*, Vol. 12, pp. 21-30, 2009.
- [21] M. A. Meyer, and H. B. Goldberg, "Applications of the turnstile junction," *IRE Trans. Microwave Theory Tech.*, Vol. 3, No. 6, pp. 40-45. 1955.
- [22] G. Engargiola and A. Navarrini, "K-band orthomode transducer with waveguide ports and balanced coaxial probes," *IEEE Trans. Microwave Theory Tech.*, Vol. 53, No. 5, pp. 1792-1801, May 2005.
- [23] G. Engargiola and A. Navarrini, "Orthomode transducer with waveguide ports and balanced coaxial probes," *Proc. 16<sup>th</sup> Int. Symp. Space Terahertz Tech.*, 2005, pp. 334-337.
- [24] A. Navarrini, A. Bolatto and R. L. Plambeck, "Test of 1mm band turnstile junction waveguide orthomode transducer," *Proc. 17<sup>th</sup> Int. Symp. Space Terahertz Tech.*, 2006, pp. 99-102.
- [25] A. Navarrini and R. L. Plambeck, "A turnstile junction waveguide orthomode transducer," *IEEE Trans. Microwave Theory Tech.*, Vol. 54, No. 1, pp. 272-277, Jan. 2006.
- [26] A. Navarrini, R. L. Plambeck and D. Chow, "A turnstile junction waveguide orthomode transducer for the 1mm band," *Proc. 16<sup>th</sup> Int. Symp. Space Terahertz Tech.*, 2005, pp. 519-523.

- [27] Y. Aramaki, N. Yoneda, M. Miyazaki and T. Horie, "Ultra-thin broadband OMT with turnstile junction," *IEEE MTT-S Int. Microwave Symp. Dig.*, 2003, pp. 47-50.
- [28] S.-G. Park, H. Lee and Y.-H. Kim, "A turnstile junction waveguide orthomode transducer for the simultaneous dual polarization radar," *Proc. Asia Pacific Microw. Conf.*, Dec. 2009, pp. 135-138.
- [29] G. Pisano, L. Pietranera, K. Isaak, L. Piccirilo, B. Johnson, B. Maffei, and S. Melhuish, "A broadband WR10 turnstile junction orthomode transducer," *IEEE Microw. Wireless Component Lett.*, Vol. 17, No 4, pp. 286-288, April 2007.
- [30] A. Tribak, J. L. Cano, A. Mediavilla and M. Boussouis, "Octave bandwidth compact turnstile-based orthomode transducer," *IEEE Microw. Wireless Component Lett.*, vol. 20, no. 10, pp. 539-541, Oct. 2010.
- [31] J. L. Cano, A. Tribak, R. Hoyland, A. Mediavilla and E. Artal, "Full band waveguide turnstile junction orthomode transducer with phase matched outputs," *Int. J. RF and Microwave*, Vol. 20, No. 3, pp. 333-341, May 2010.
- [32] G. Chattopadhyay and J. E. Carlstrom, "Finline ortho-mode transducer for millimeter waves," *IEEE Microwave and Guided Wave Lett.*, Vol. 9, No 9, pp. 339-341, Sep. 1999.
- [33] C. E. Groppi, C. Y. D. Aubigny, A. W. Lichtenberger, C. M. Lyons, C. K. Walker, "Broadband finline ortho-mode transducer for the 750-1150GHz band," *Proc. 16<sup>th</sup> Int. Symp. Space Terahertz Tech.*, 2005, pp. 513-518.
- [34] S. J. Skinner and G. L. James, "Wide-band orthomode transducers," *IEEE Trans. Microwave Theory Tech.*, Vol. 39, No. 2, pp. 294-300, Feb. 1991.
- [35] L. J. Foged, L. Duchesne, P. Iversen and G. Barone, "High precision probes for wide-band near-field measurements in dual polarization," *Proc. Int. Symp. Ant. Propa. EM Theo. (ISAPE)*, Aug. 2003.

- [36] M. Ludovico, B. Piovano, G. Bertin, G. Zarba, L. Accatino and M. Mongiardo, "CAD and optimization of compact ortho-mode transducers," ,” *IEEE Trans. Microwave Theory Tech.*, Vol. 47, No. 12, pp. 2479-2486, Dec. 1999.
- [37] J. Uher, J. Bornemann and U. Rosenberg, *Waveguide Components for Antenna Feed systems: Theory and CAD*, Artech House, 1993.
- [38] D. M. Pozar, *Microwave Engineering*, 3<sup>rd</sup> Ed., New York: John Wiley & Sons, 2005.
- [39] A. Balanis, *Advanced Engineering Electromagnetics*, John Wiley & Sons, 1989.
- [40] G. Matthaei, L. Young and E. M. Jones, *Microwave Filters, Impedance-Matching Networks, and Coupling Structures*, Artech House, 1980.
- [41] N. Marcuvitz, *Waveguide Handbook*, IEEE Electromagnetic Wave Series 21, Peter Peregrinus Ltd., 1986.
- [42] P. Praßmayer, W. Blair and K. Kaczmarek, US Patent 7,750,763 B2, "Waveguide bend having a square shape cross-section," 6 Jul. 2010.
- [43] A. Casanueva, J. Pereda and A. Mediavilla, "Optimim compact *H*- and *E*-plane corners in rectangular waveguide," *Microw. Opt. Tech. Lett.*, Vol. 42, No. 6, pp. 494-497, 20 Sep. 2004.
- [44] B. Enkhbayar, J. –H. Bang, J. –S. Park, B. –K. Joo, J. Chun, B. –C. Ahn, "Design of a stepped *H*-plane bend in a rectangular waveguide," *Proc. ICCIT 2009*, Ulaanbaatar, Aug. 2009, pp. 90-92.
- [45] A. R. Kerr, "Elements for *E*-plane split-block waveguide circuits," ALMA Memo 381, National Radio Astronomy Observatory, 5 Jul. 2001.
- [46] B. Gimeno and M. Gudlielmi, "Multimode equivalent network representation for the Y-junction of rectangular waveguides," *IEE Proc. Microw. Antennas Propag.*, Vol. 144, No. 3, pp. 161-166, June 1997.

- [47] S. G. Tantawi, "A novel circular TE<sub>01</sub>-mode bend for ultra-high-power applications," *J. Electro. Waves Appl.*, Vol. 18, No. 12, pp. 1679-1687, 2004.
- [48] C. D. Nantista and S. G. Tantawi, "Over-moded rectangular waveguide components for a multi-moded RF power distribution system," *Proc. EPAC*, Vienna, 2000, pp. 318-320.
- [49] O. Vanbésien and D. Lippens, "Dual-branch electron waveguide coupler," *Material Sci. Eng. B*, Vol. 35, pp. 90-96, 1995.
- [50] G. Narayanan and N. R. Erickson, "Integrated terahertz heterodyne focal plane array receivers," *Proc. Far-IR, Sub-MM & MM Detector Tech. Workshop*, Apr. 2002.
- [51] J.- P. Boujet and J. Dietz, US Patent 4,210,880, "Multiple branch-line waveguide coupler," 1 Jul. 1980.
- [52] B. Enkhbayar, J.- H. Bang, E.- J. Cha and B.- C. Ahn, "Design of a W-band monopulse comparator based on *E*- and *H*- plane waveguide couplers" *Proc. 11th IEEE Annual Wire. Microw. Tech. Conf.*, 2010, pp. 1-5.
- [53] S. Srikanth and A. R. Kerr, "Waveguide quadrature hybrids for ALMA receivers," ALMA Memo 343, National Radio Astronomy Observatory, 11 Jan. 2001.
- [54] S. M. X. Claude, T. Cunningham, A. K. Kerr and S. -K. Pan, "Design of a sideband-separating balanced SIS mixer based on waveguide hybrids," ALMA Memo 316, 20 Sep. 2000.
- [55] H. Andoh, S. Asayama, H. Ogawa, N. Mizuno, T. Tsukamoto, T. Sugiura and Y. Fukui, "Numerical matrix analysis for performances of wideband 100GHz branch-line couplers," *Int. Jour. Infrared Millim. Waves*, Vol. 24, No. 5, pp. 773-788, May 2003.
- [56] H. Andoh, T. Minamidani, S. Asayama, Y. Yonekura, H. Ogawa, N. Mizuno, A. Mizuno and Y. Fukui, "Design of wideband 3dB branch-line couplers for ALMA bands 3 to 10," ALMA Memo 468, 7 July 2003.

- [57] F. P. Mena, J. Kooi, A. M. Baryshev, C. F. J. Lodewijk, T. M. Klapwijk, W. Wild, V. Desmaris, D. Meledin, A. Pavolotsky and V. Belitsky, "RF performance of a 600-720GHz sideband-separating mixer with all-copper micromachined waveguide mixer block," *Proc. 19<sup>th</sup> Int. Symp. Space Terahertz Tech.*, Apr. 2008, pp. 90-92.
- [58] G. Narayanan, N. R. Erickson, and R. M. Grosslein, "Low cost direct machining of terahertz waveguide structures," *Proc. 10<sup>th</sup> Int. Symp. Space Terahertz Tech.*, Mar. 1999, pp. 518-528.

## ACKNOWLEDGEMENTS

I would like to thank my supervisor, Professor Bierng-Chearl Ahn, who guided me through my Ph. D. study. Without his help and support, I could not get the degree of doctor of philosophy. During the last four years, I had learnt a great deal from him, especially the understanding of the most fundamental theories in the antenna and electromagnetics. I also would like to thank members of committee, Professor Jae-Hoon Ahn, Professor Kyung-Seok Kim, Dr. Jae-Hoon Bang, Professor Byoung-Kwon Ahn for their guidance and support.

I gratefully acknowledge the BK21 Research-Oriented Consortium of Chungbuk National University for financial support.

Thanks also go to my teacher Dr. Jae-Hoon Bang for suggesting lots of interesting ideas and his sincere contributions. I also thank to Dong-Hyun Min. He helped me with measurements.

I would like to say many thanks to all of the members in my laboratory. They help me so much from the first time I came to Korea. They helped me with good friendship, good cooperation, and great working environment.

I would like to Professor Tsogbadrakh Galsan and Professor Baljinnyam Tsevegmid for their many guides in research and life. Very special thanks to Professor Sukhbaatar Bilgee and Mrs. Khongorzul Dashdondov who gave me the big chance for studying in Korea.

Finally I wish to thank my family for their great support during the doctoral study.